INTERFACIAL CHARACTERISTICS OF PROPYLENE CARBONATE AND VALIDATION OF SIMULATION MODELS FOR ELECTROCHEMICAL APPLICATIONS

An Abstract

Submitted On The Third day of December 2014

To The Department Of Chemical And Biomolecular Engineering

In Partial Fulfillment Of The Requirements

Of The School Of Science And Engineering

Of Tulane University

For The Degree

Of

Doctor Of Philosophy

By

Xinli You

Approved: Lawrence R. Pratt

Lawrence R. Pratt, Ph.D.
Director

Steven Rick, Ph.D.

Vijay John, Ph.D.

Noshir S. Pesika, Ph.D.

Abstract

Supercapacitors have occupy an indispensable role in today's energy storage systems due to their high power density and long life. The introduction of carbon nanotube (CNT) forests as electrode offers the possibility of nano-scale design and high capacitance. We have performed molecular dynamics simulations on a CNT forest-based electrochemical double-layer capacitor (EDLC) and a widely used electrolyte solution (tetra-ethylammonium tetra-fluoroborate in propylene carbonate, $TEABF_4$/PC)

We compare corresponding primitive model and atomically detailed model of $TEABF_4$/PC, emphasizing the significance of ion clustering in electrolytes. The molecular dynamic simulation results suggests that the arrangement of closest neighbors leads to the formation of cation-anion chains or rings. Fuoss's discussion of ion-pairing model provides the approximation for a primitive model of 1-1 electrolyte is not broadly satisfactory for both primitive and atomically detailed cases. A more general Poisson statistical assumption is shown to be satisfactory when coordination numbers are low, as is likely to be the case when ion-pairing initiates. We examined the Poisson-based model over a range of concentrations for both models of $TEABF_4$/PC, and the atomically detailed model results identified solvent-separated nearest-neighbor ion-pairs.

Large surface areas plays an essential role in nanomaterial properties, which calls for an accurate description of interfaces through modeling. We studied propylene carbonate, a widely used solvent in EDLC systems. PC wets graphite with a contact

angle of 31°. The MD simulation model reproduced this contact angle after reduction 40% of the strength of graphite-C atom Lennard-Jones interactions with the solvent. The critical temperature of PC was accurately evaluated by extrapolating the PC liquid-vapor surface tensions. PC molecules tend to lie flat on the PC liquid-vapor surface, and project the propyl carbon toward the vapor phase. Liquid PC simulations also provide basic data for construction of accurate information to assist in device-level modeling of EDLCs.

The most serious uncertainty with previous simulations of CNT based EDLCs was definition of the actual composition of the pores. Therefore, direct simulations of filling of CNT forest based electrochemical double-layer capacitors with $TEABF_4$/PC solution was performed. Those calculation characterize the charging and discharging process, including rates of charging responses, the possibility of bubble formation, and kinetic properties with confinement. The mobilities of ions and solvent was investigated through mean square displacement (MSD) and velocity autocorrelation functions (VACF). The memory kernel was extracted from VACF by discretized linear-equation solving and a specialized Fourier transform method, results implies the existence of dielectric friction.

With the interest in chemical features of EDLCs, a multi-scale theory was developed to embed high resolution *ab initio* molecular dynamics (AIMD) methods into studies of EDLCs. This theory was based on McMillan-Mayer theory, potential distribution approach, and quasi-chemical theory. The quasi-chemical theory allow us to break-up the free energies into *packing*, *outer-shell* and *chemical* contributions, where the last part can be done by AIMD directly. For the primitive model of $TEABF_4$/PC, Gaussian statistical models are effective for these *outer-shell* contributions. And the Gaussian approximation is more efficient than the Bennett method in achieving an accurate mean activity coefficient.

INTERFACIAL CHARACTERISTICS OF PROPYLENE CARBONATE AND VALIDATION OF SIMULATION MODELS FOR ELECTROCHEMICAL APPLICATIONS

A Dissertation

Submitted On The Third day of December 2014

In Partial Fulfillment Of The Requirements

Of The School Of Science And Engineering

Of Tulane University

For The Degree

Of

Doctor Of Philosophy

By

Xinli You

Xinli You

Approved: Lawrence R. Pratt

Lawrence R. Pratt, Ph.D.
Chairman

Steven Rick, Ph.D.

Vijay John, Ph.D.

Noshir S. Pesika, Ph.D.

Acknowledgement

I would like to express my most sincere gratitude to my advisor Prof. Lawrence R. Pratt, for his support, guidance, invaluable comments, and suggestions that benefited me during the research. I thank him for introducing me the careful-and-neat research spirit. His immense knowledge becomes the "thermo-encyclopedia" of our lab, while his patient instructions and historical story-like theory-teaching charged my *research energy capacitor*, kept me interested, motivated and focused.

I also take this opportunity to record our thanks to the thesis committee: Dr. Steven Rick, Dr. Vijay John, and Dr. Noshir Pesika, not only for their time and extreme patience, but for their encouragement, inspiration and constructive advises.

I would also like to thank our Statistical Mechanics Lab *star* members: Mangesh Chaudhari, Peixi Zhu, Wei Zhang, Liang Tan. They are the ones who solved my technical problems, shared their truthful and illuminating views related to the project, and brought me a joyful working environment.

I also express my warm thanks to all faculties and friends in the CBE department. It was your helping hands and glowing hearts supported me overcome the difficulties and interruptions.

Last but not the least, my family: my parents Jianzhong You, Lin Li, and my husband Tijiang Liu, for always being my spiritual pillars.

Table of Contents

List of Tables

List of Figures

Chapter 1

Background

An important future electrical storage system, electrochemical capacitors (ECs) have attracted much attention in recent years.[1–3] Although storing less energy per unit mass than Li-ion batteries, ECs can be rapidly charged and discharged, making them promising for applications which need faster and higher-power energy transfer.[4] Generally, ECs comprise electrodes (e.g. carbon, metal-oxides), electrolytes (e.g. H_2SO_4(aq) or organic electrolyte/propylene carbonate) and separator. Electrochemical double layer capacitors (EDLCs) are a common type of ECs. EDLCs (also called supercapacitors) often utilize carbon-based active materials as electrodes because of their large surface area available for charge storage. Among them, carbon nanotube (CNT) based EDLCs have achieved high energy and power density not only due to their high surface area but also their excellent conductivity. Indeed, CNT materials are potential candidates as electrodes for a new type of supercapacitors.[5–9] Recently proposed EDLCs with electrodes of dense, vertically aligned CNT forests (Fig. 1.1) moved these studies further.[10] A group led by Joel E. Schindall at MIT has developed commercialized supercapacitors based on ordered arrays of CNTs.

The ability of an EDLC to store charge also depends on the choice of electrolyte because the good accessibility of the electrolyte ions to the porous surface-area depends on the size match between pores and electrolyte ion.[11] Therefore, it is im-

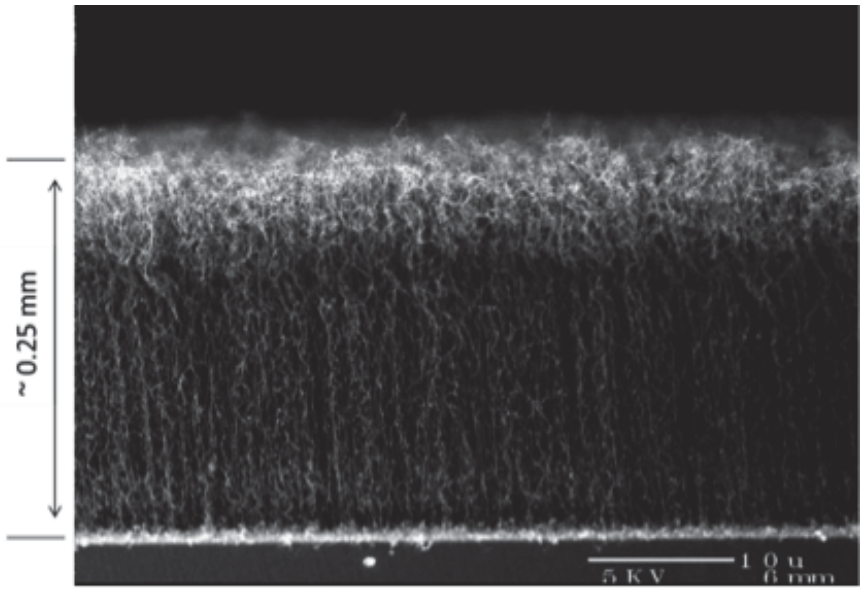

Figure 1.1: Cross section of carbon nanotube (CNT) forests, adapted from http://mitei.mit.edu/news/novel-ultracapacitor.

portant to choose an electrolyte that is compatible with CNT forests. As a popular electrolyte choice, the solution of tetraethylammonium tetrafluoroborate in propylene carbonate has shown promising preliminary results in the proposed EDLCs with electrodes of vertically aligned CNT forests.[10]

Despite the large effort and rapid progress on developing CNT forests-based EDLCs, our fundamental understanding of the underlying molecular mechanism remains incomplete.[12–15] For example, although molecule-specific choices for the electrolyte and solvent are important, molecular-scale theories to guide and interpret those choices are limited.[16,17] Examples include the effect of pore size on solution access and on the capacitance, the role of the electrolyte, and molecular time-scale dynamical processes that govern the fastest responses.[13]

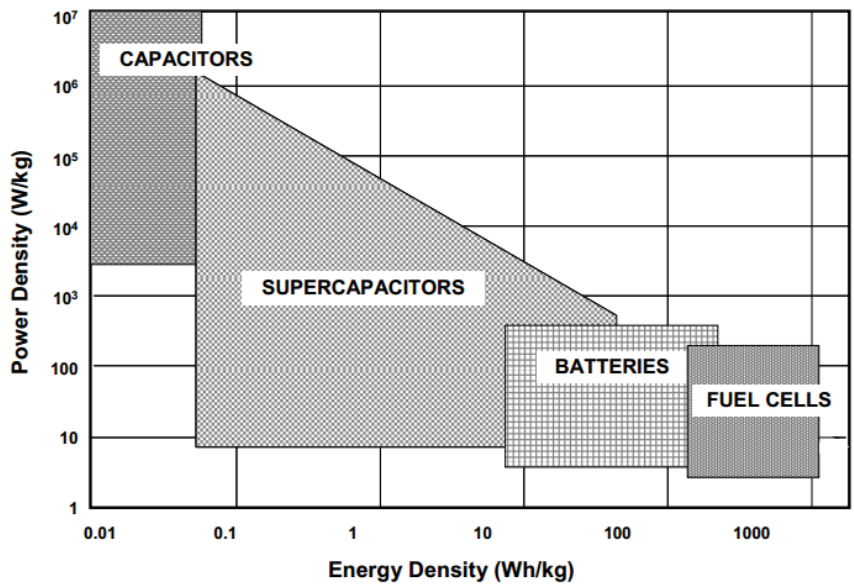

Figure 1.2: power density against energy density for important energy storage systems.[18]

1.1 Electrochemical double-layer capacitors

In response to changing global landscape, the industrial and scientific communities have become more interested in the sustainable and renewable energy resources, as well as the development of electric vehicles or hybrid electric vehicles with low CO_2 emissions. As a consequence, high efficient electrical energy storage devices and harvesting applications are required. Important energy storage systems are batteries, fuel cells, capacitors. They are usually shown in a "Ragone Plot" (Fig. 1.2). Fuel cells and batteries are classified as high energy density but low power density. Capacitors, on the other hand, are classified as high power density and low energy density. In recent years, electrochemical capacitors have attracted much attention mainly because they fill the gap between conventional dielectric capacitors and battery/fuel cells. Especially, they can complement batteries when high power delivery or uptake is needed.

The capacitors can be further classified as electrostatic capacitors, electrolytic

capacitors and electrochemical capacitors. The first two are conventional capacitors which typically include two parallel metallic electrodes separated by a dielectrics or conductive electrolyte salt. Electrochemical double-layer capacitors, part of electrochemical capacitors, are also called ultra-capacitors, or super-capacitors. Generally, EDLCs consists of two electrodes, an electrolyte, and a separator that electrically isolates the two electrodes.

The mechanism of double-layer capacitance can be described as

$$C = \frac{\epsilon_r \epsilon_0 A}{d} \quad \text{or} \quad C/A = \frac{\epsilon_r \epsilon_0}{d} \ , \tag{1.1}$$

with the stored electric energy, $E = \frac{1}{2}CV^2$. The ϵ_r is the solvent dielectric constant, ϵ_0 is the dielectric constant of the vacuum, d is the effective thickness of the double layer (charge separation distance) and A is the electrode surface area.

The maximum power $P_{\max}$ for a capacitor is given by[19,20]

$$P_{\max} = \frac{V^2}{4 \times \text{ESR}} \ , \tag{1.2}$$

with V the voltage, ESR is known as the equivalent series resistance which is contributed by current collectors, electrodes, and electrolyte.

Since the double-layer charge storage is a surface process, the ideal electrodes should have large specific surface area (SSA). Another key factor is high electronic conductivity (Low ESR). The practical candidates are carbon materials, metal-oxides, conducting polymer, hybrid and conducting polymers. Among them, activated carbons are the most widely used materials today, because of their high SSA, high conductivity, availability, relatively low cost. But activated carbons suffer from irregular pore size, uneven path, impurities and dangling bonds, contact resistance etc. Nano-structured materials, such as carbon nanotube, possess high SSA and high

conductivity, and can provide short transport/diffusion path lengths for ions and electrons, leading to faster kinetics, more efficient contact of electrolyte ions, and results in high charge/discharge capacities even at high current densities due to the ordered arrays of carbon nanotube.

The electrolytes in EDLCs have equal importance to electrode materials. Energy density is largely dependent on the breakdown voltage of the electrolyte. ESR is strongly dependent on electrolyte conductivity. Practically, an ideal electrolyte in EDLC should process high breakdown voltage, high conductivity, low volatility, low toxicity, low cost as well as availability at high purity. Currently, there are three types of electrolytes in use in EDLCs: organic, aqueous and ionic liquids (ILs). Aqueous electrolyte (such as H_2SO_4, Na_2SO_4, KOH and NH_4Cl) have high conductivity and high ionic concentration which means high power density, but suffer low breakdown voltage ($\lesssim 1V$) which limit both the energy density and power density. The breakdown voltage of an organic electrolyte can be as high as $\gtrsim 3.0V$ which largely increases the power and energy storage. This is why organic electrolytes are chosen in most commercial devices. Among organic electrolytes, acetonitrile and propylene carbonate (PC) are the most commonly used solvents. Acetonitrile can dissolve larger amounts of salt than other solvents, but suffers from high volatility, environmental and toxicity problems. PC-based electrolytes are friendly to the environment and can offer a wide electrochemical window, a wide range of operating temperature, as well as good conductivity. Besides, organic salts such as tetra-ethylammonium tetra-fluoroborate, tetra-ethylphosphonium tetra-fluoroborate, and tri-ethylmethylammonium tetra-fluoroborate ($TEMABF_4$) have also been used in EDLC electrolytes. However, the energy storage of EDLCs can be significantly weakened by just a tiny amount (> 10 ppm) of water.[21] So high-purity of organic electrolyte is a key.

Ionic liquids are promising electrolyte in the future because of its higher breakdown voltage $\sim 4.5V$.[22] But the drawback of current ionic liquids as the electrolyte are obvious such as low electrolyte conductivity in the range between $-30°$ and $+60°$, where batteries and supercapacitors are mainly used.[23]

In fact, electrodes and electrolytes in EDLCs are closely associated with each other. The mobility of ions in pores and the ability of charge storage in electrodes are greatly dependent on the accessibility of the ions of electrolyte to the porous surface-area of electrodes. If the sizes of pores are too small, electrolyte ions will not pass through the pores. As a result, the actual capacitance will be much lower. Thus, the optimal distribution of pore size depends on the size of ions.[2,11,24]

The importance of the solvent was also the subject of a particularly interesting study[25] of the aging behavior of EDLCs based on activated carbon electrodes bound with poly(tetrafluoroethylene) in electrolyte solutions based on acetonitrile (AN) and propylene carbonate (PC) at a constant elevated cell voltage of 3.5V. Significant modifications of the electrode surface were observed and provided clear evidence for the deposition of electrolyte degradation products on the electrodes. It was found that the enhanced aging rate of symmetric EDLCs in either solvent at elevated voltages is dominated by the aging of a single electrode, and that the polarity of this limiting electrode depends directly on the solvent. Clearly, several basic physical chemistry issues associated with their function and the role of the solution have not been characterized at a molecular level that would be relevant to the design of these systems.

1.1.1 Focuses for Theory & Modeling and Some Previous Work

Theory and modeling of EDLCs got a big impetus by the announcement of "an anomalous increase in carbon capacitance at pore sizes less than 1 nanometer" with carbide-derived amorphous carbon as electrode material.[26] Yang, *et al.,*[13] proved

the feasibility of molecular-scale computational simulation of EDLCs based on CNT forests, and obtained capacitance magnitudes in remarkably close agreement the experiment.[27] Beyond consensus on reasonable magnitudes, the "anomalous increase" has not been universally observed; specifically[28] "The study of 28 porous carbons shows that the specific capacitance in the electrolyte $(C_2H_5)_4NBF_4$/acetonitrile is relatively constant between 0.7 and 15 nm (0.094 ± 0.011 F m^{-2}). The increase in pores below 1 nm and the lower values between 1 and 2 nm reported earlier are not observed in the present work." Though 28 different porous carbons were studied, the group originating the "anomalous increase" announcement suggests[29] that those null observations are due to "...comparison of data obtained with various carbons with broad pore size distributions and in different electrolytes." The original null claim has been re-asserted.[30]

There has been an avalanche of responding modeling work.[31–54] Of course, modeling calculations are not expected to prove or disprove a specific contentious experimental feature. Indeed, the available modeling calculations all adopt simplifications that themselves deserve scrutiny and proof. But accumulating improvements of the simulation and theory serve to develop a better grounded physical understanding that can lead to a correct assessment and integration of the various results. The "anomalous increase" issue may be a candidate for resolution in that incremental fashion.

Thus, theory and modeling needs to be developed and improved for these applications. As we have discussed elsewhere here, an important feature of EDLCs is their prompt response. This suggests that their dynamical performance is a good topic for further study, including the general transport characteristics of these solutions but also the dynamic filling of pore-spaces in EDLCs. Indeed, preceding theory and modeling work has manifestly avoided study of the dynamics relevant to the function

of EDLCs. For example, wide-spread enthusiasm for ionic liquid filling solutions typically overlooks the important feature that ionic liquids will almost surely reduce the conductivity of the solution.

1.2 Molecular theory of associated electrolyte solutions

1.2.1 McMillan-Mayer theory

The moderm starting point for understanding electrolyte solutions is McMillan-Mayer (MM) theory, developed by W. G. McMillan and J. E. Mayer in 1945.[55,56] MM theory is set in the context of the classical thermodynamics. An electrolyte solution is characterized by the state (T, V, N, μ_0), where T is the temperature , N is the mole-number of solutes and V is the volume, μ_0 is the solvent chemical potential. MM theory supports the common mode that the solvent is treated as dielectric medium in which the solutes are distributed. Then, an electrolyte solution is treated as "an imperfect gas where the vacuum has been replaced by a solvent".[57] In a molecular simulation language, the solvent coordinates of the solution are excluded from the molecular dynamics (MD) or *ab initio* molecular dynamics (AIMD) simulation. Since the solvent chemical potential during the charging process is considered to be constant, MM theory is very convenient in electrolyte thermodynamics.

MM theory is a pinnacle of coarse-graining for the statistical mechanics of solutions and achieves a vast conceptual simplification for the theory of electrolyte solutions. "Primitive model" is then synonymous[56,58] with "McMillan-Mayer model." For primitive models, furthermore, an enormous literature of sophisticated theory is available.[59,60] For example, Debye-Hückel theory[61] gave accurate predictions of mean activity coefficients for ions in dilute solution. It might be argued that no sac-

rifice of molecular realism is implied by the McMillan-Mayer theory. However, that theory has not been used specifically to construct a primitive model for a system of experimental interest.[62] Indeed, a catalog of the multi-body potentials implied by a literal McMillan-Mayer approach would be prohibitive by itself.[63]

Beyond primitive models, the realism of molecular models that are studied varies over a vast range. In judging molecular realism, a notable characteristic is whether the model permits prediction of the results of structural experiments that reasonably might be expected. Atomic resolution models are typically required to treat X-ray and neutron scattering experiments on solutions. RISM theories[64] and molecular simulation[65,66] have been exploited for those purposes. If approximate theories or methods have sufficient physical clarity, then they offer the advantage of testing physical ideas by comparison with experimental results.

1.2.2 Quasi-Chemical Theory

Recent developments of quasi-chemical theory offer an alternative way to the theory of solutions from a molecular scale.[67–71] The major targets of quasi-chemical theory are solvation free energies from a wide variety of simulation records obtained with techniques such as molecular dynamics with an empirical force field or *ab initio* MD simulations. A main feature of the theory is the separation of the neighborhood of the solute into an inner shell and outer shell. This separation allows the solvation free energy to be dissected into separate contributions with clear physical meanings: short range chemical and packing contribution, but also further long range. Depending on the available simulation data some of these contributions can be calculated specifically in detail, while others can be handled with physically motivated approximations.

1.3 Molecular Modeling

Molecular modeling focuses on atomistic level description of molecular systems through a large variety of theoretical methods and computational techniques. This description provides an applicable way to compute the macroscopic behavior from microscopic interactions. For example, macroscopic observables (e.g. solvation energy) can be obtained from the average of observables over selected microscopic states. With reasonable modeling on a microscopic level, one can understand and interpret the experimental results. Furthermore, one may be able to quantitatively estimate experimental results and interpolate or extrapolate experimental data into experimentally inaccessible regions.

Molecular modeling methods are usually divided into molecular dynamics (MD), Monte Carlo (MC) methods. Modern methods blend these two approaches together in appropriate ways.[65,66]

There are two main families of MD methods, which can be distinguished according to the model (and the resulting mathematical formalism) chosen to represent a physical system. In the 'classical' mechanics approach to MD simulations molecules are treated as classical objects. The microscopic behaviors of an N-particle system are obtained by numerically solving the Newton's equations of motion for a system of interacting particles, where forces between the particles and potential energy are determined by empirical force fields. In the 'quantum' or 'first-principles' MD simulations, which started in the 1980s with the work of Car and Parinello, the quantum nature of the chemical bond is accounted for. The electron density function for the valence electrons that determine bonding in the system is computed using quantum equations, whereas the dynamics of ions (nuclei with their inner electrons) is followed classically. Quantum MD simulations represent an important advance over the classical approach since then do not rely on preset force fields as classical MD does.

However, they require more computational resources. At present only the classical MD is practical for simulations of molecular systems comprising many thousands of atoms over time scales of nanoseconds.

In both molecular dynamics methods, the successive configurations of the system are connected in time by solving Newtonian equations of motion and/or Schrödinger's equation, *i.e.*, the state of the system at future times is predicted from its current state. However, in MC method, the successive configurations of the system is a randomly generated configuration determined by a special set of criteria (Generally, the configuration with lower potential energy is preferred). In another words, the current state of system depends only upon its immediate predecessor. MC method fundamentally requires a description of the potential energy of a given molecular configuration as classical MD method does, but calculations achieve that in a vast variety of ways.

1.4 Outline

This research is aimed to study the electrochemical double-layer capacitors based on carbon nanotube forests in the molecular level. This requires a detailed understanding of electrolyte solution theories, interfacial behavior of solvent, and charging and discharging processes. Developed with experimental results, we attempt to offer better understanding on the molecular mechanism of CNT-based EDLCs and therefore offer a feasible strategy for EDLC design.

There are four major steps in this thesis: first, we will develop a Poisson statistical theory to treat an ion-pairing model and test it for $TEABF_4$/PC solutions (Fig: 1.3); Secondly, simulations of solvent PC to understand its interfacial properties; in the third part, we will explore the molecular mechanism of EDLCs based on CNT forests, including a full charge and discharge cycle; last, a multi-scale theory will

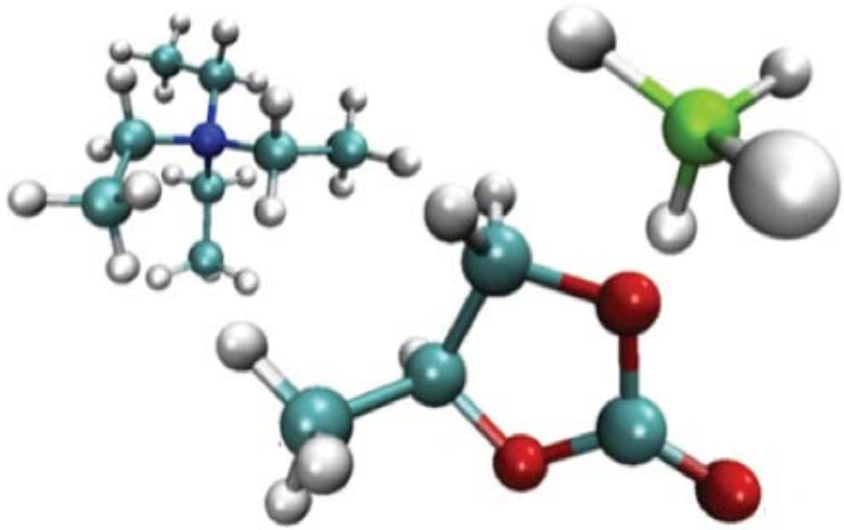

Figure 1.3: propylene carbonate (PC) enantiomer with atom labeling used in this study. PC is a non-reactive, low-toxicity, aprotic, highly polar dielectric solvent widely used in nonaqueous electrochemical systems. The $TEABF_4$ salt consists of cation (TEA^+) and anion (BF_4^-) as electrolyte for ultracapacitor.

be proposed to involve the time-and-scale-limited AIMD methods into our EDLCs studies.

Ion association is one important subject for physical understanding of electrolytes. In Chapter 2, a Poisson statistical approximation is obtained, generalizing the well known Fuoss ion-pairing model. The model is tested using two distinct simulation data sets. These simulations treated solutions of $TEABF_4$/PC, one at atomic resolution and the other on the basis of a primitive electrolyte solution model over a range of concentrations. This study is useful to characterize the interionic neighborship.

In Chapter 3, we exhaustively studied the interfacial behaviors of solvent PC. PC-graphite contact angle was evaluated by both MD simulation and experiments. Agreement was achieved by adjusting the Lennard-Jones interaction between PC and

graphite carbon atoms. Simulations of PC liquid-vapor interface provides the surface tensions, molecular structures on the interface layer. Together with the bulk liquid PC simulation, this study serves as a preparation for constructing a feasible simulation model of CNT-based EDLCs.

The direct simulations of filling of EDLCs based on CNT will be reported in Chapter 4. We looked into the charging and discharging cycle, considered the possibility of bubble formation and analyzing the rates of charging response. Transport behaviors for ions and solvent were accessed from high resolution simulations. The memory function of PC identifies the role of long-ranged interaction effects, which have been called 'dielectric friction' in other setting. Considering PC molecules are not ions and the interests for the basic theory of liquids, we broaden our memory kernel studies to three other popular solvents, ethylene carbonate, acetonitrile, and water.

With the interest in chemical properties of EDLCs, the final chapter discusses a multi-scale theory to apply AIMD methods to electrolyte solutions. Several theoretical specifics, McMillan-Mayer theory, the potential distribution approach, and quasi-chemical theory, are developed here. The Appendix A gives an accessible derivation of the MM theory results used here; Appendices B and C present technical features of the potential distribution theory and quasi-chemical theory, respectively, required in the main text. Sec. 5.3 gives a demonstration of the results obtained for the primitive electrolyte solution model ($TEABF_4$/PC).

Chapter 2

Generalizations of the Fuoss Approximation for Ion Pairing

2.1 Introduction

Association of ionic species in electrolytes is common in non-aqueous solutions.[72] As an example, the concentration of saturated tetra-ethylammonium tetra-fluoroborate in propylene carbonate under standard conditions is about [73] 0.86 mol/dm^3, and direct numerical simulation at the supersaturate state of 1 mol/dm^3 (FIG. 2.1) shows interesting clustering effects (FIG. 2.2). Note (upper panel) that the average B-occupancy of a naturally defined N-inner shell is about 2, and that is clearly true also of the average N-occupancy of a naturally defined B-inner shell is about 2. This suggests a natural microstructural organization on the basis of formation of (cation-anion) chains.

Ion clustering has long been an essential ingredient of our physical understanding of electrolyte solutions at elevated concentrations,[72,77–86] To describe pairing of a counter-ion of type γ with a co-ion of type α, we focus on the radial distribution of the *closest* γ-ion to a distinguished α-ion. We denote that normalized radial distribution

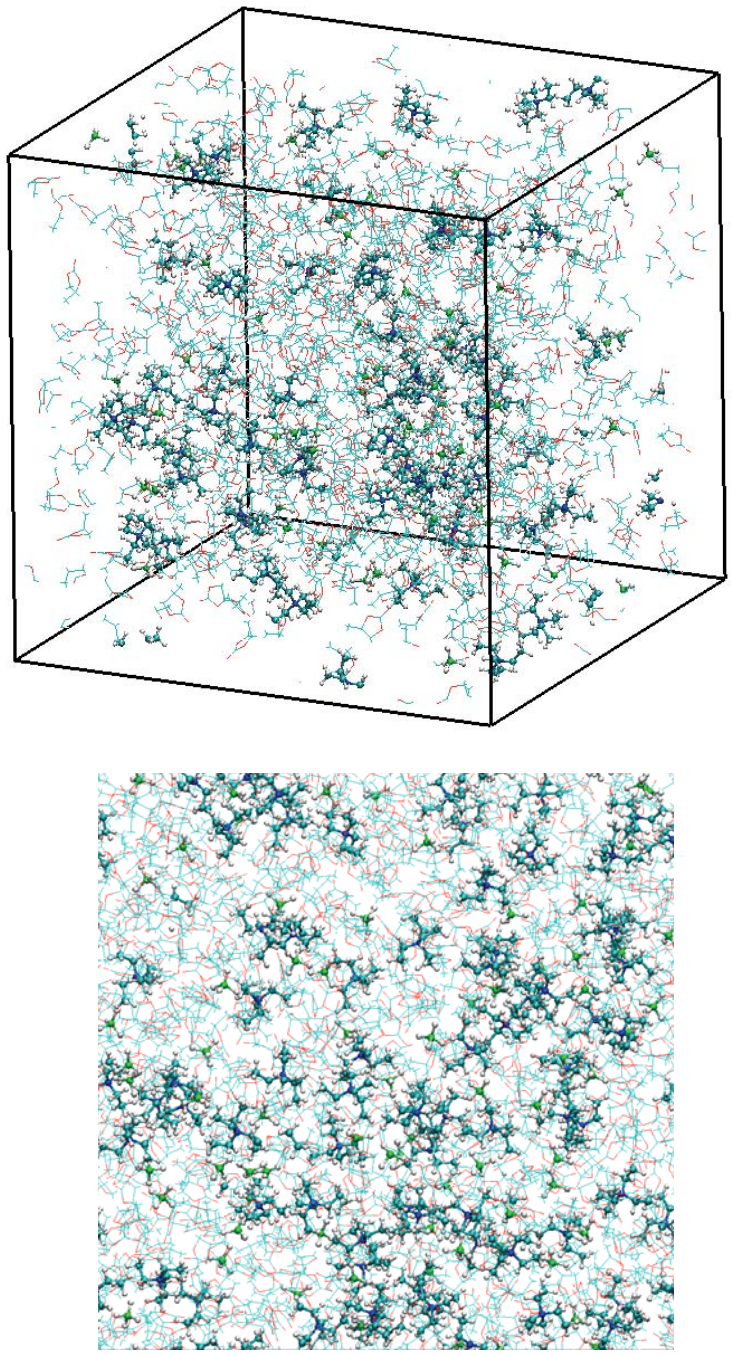

Figure 2.1: Snapshots for simulation model of bulk tetra-ethylammonium tetra-fluoroborate in propylene carbonate. Simulation details are specified in Sec: 2.5.1.

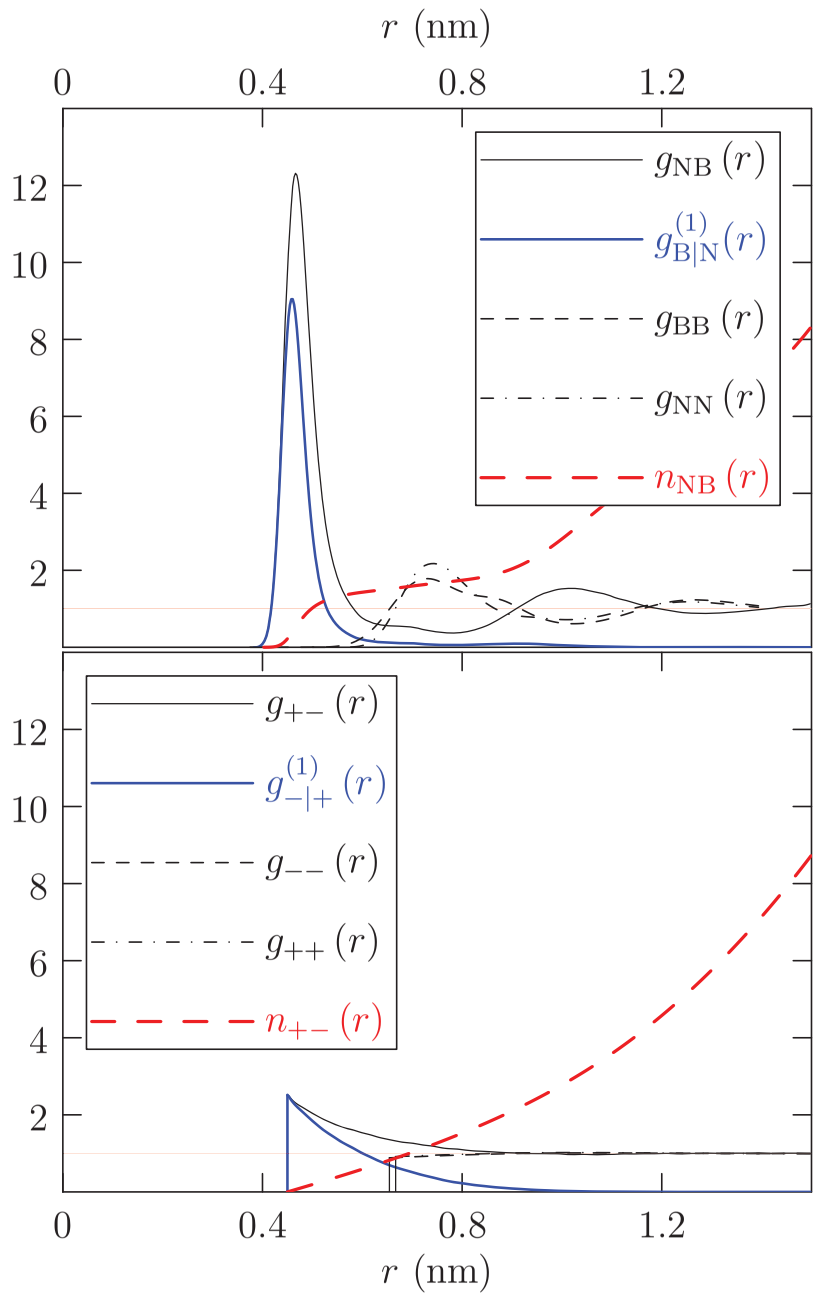

Figure 2.2: Upper-panel: Ion-ion radial distribution functions for atomically-detailed simulation[74,75] of tetra-ethylammonium tetra-fluoroborate in propylene carbonate ($TEABF_4$/PC) at $T = 300$ K, $p = 1$ atm, and the slightly supersaturated concentration of 1 mol/dm^3. $g^{(1)}_{\mathrm{B|N}}(r)$ is the radial distribution of the nearest B-neighbor of an N-atom. Lower panel: Results for a corresponding primitive model with dielectric constant and with ion charges and sizes matched to the $TEABF_4$/PC case above. Specifically the model dielectric constant is $\epsilon = 60$, and $d_{++} = 0.6668$ nm, $d_{--} = 0.6543$ nm, $d_{-+} = 0.45$ nm are distances of closest approach for the hard spherical ions. The lower panel was produced by Monte Carlo simulation of a neutral system of 2×500 hard spherical ions in conventional cubical periodic boundary conditions at the same temperature and concentration as the results above, utilizing the Towhee[76] package adapted to the present system.

as $g^{(1)}_{\gamma|\alpha}(r)$. A famous discussion of Fuoss[87] arrived at the approximation

$$\ln g^{(1)}_{\gamma|\alpha}(r) \approx \frac{\beta q^2}{\epsilon r} - 4\pi\rho \int_{d_{\gamma\alpha}}^{r} \mathrm{e}^{\frac{\beta q^2}{\epsilon x}} x^2 \mathrm{d}x \ , r \geq d_{\gamma\alpha} \tag{2.1}$$

for a primitive model of 1-1 electrolyte as in Fig. 2.2. Here q is the magnitude of the formal ionic charges, $d_{\gamma\alpha}$ is the distance of closest approach, ϵ is the solution dielectric constant, 2ρ is number density of ions, and $(k\beta)^{-1} = T$ is the temperature. We propose and test generalizations of Eq. (2.1) in the following.

Several complications of the distributions of near-neighbor ion-pair distances motivate the generalizations that we develop. First, ion-clustering can be particularly sensitive to non-ionic interactions. Comparison (Fig. 2.2) of atomically-detailed simulation results[74,75] with those of a corresponding primitive model package[76] straightforwardly exemplifies that point. Eq. (2.1) only treats classic ionic interactions. Second, even for primitive models the Fuoss approximation can be unsatisfactory (Fig. 2.3). Third, nearest-neighbor distributions generally depend on which ion of an ion-pair is regarded as the central ion (Fig. 2.4). The distribution of anions nearest to a cation is different from the distribution of the cations nearest to an anion, $g^{(1)}_{\alpha|\gamma}(r) \neq g^{(1)}_{\gamma|\alpha}(r)$. The approximation Eq. (2.1) is symmetric $g^{(1)}_{\alpha|\gamma}(r) = g^{(1)}_{\gamma|\alpha}(r)$.

We are lead then to generalizations by recalling that the probability that a ball of radius r centered on an α-ion is *empty* of γ-ions can be obtained from

$$p_{\gamma|\alpha}(n=0) = 4\pi\rho_\gamma \int_r^\infty g^{(1)}_{\gamma|\alpha}(x) x^2 \mathrm{d}x \ , \tag{2.2}$$

the assessment of the probability that the *nearest* γ-ion is further away than r. The simple estimate

$$p_{\gamma|\alpha}(n=0) \approx \exp\left[-\left\langle n\left(r\right)\right\rangle\right] \ , \tag{2.3}$$

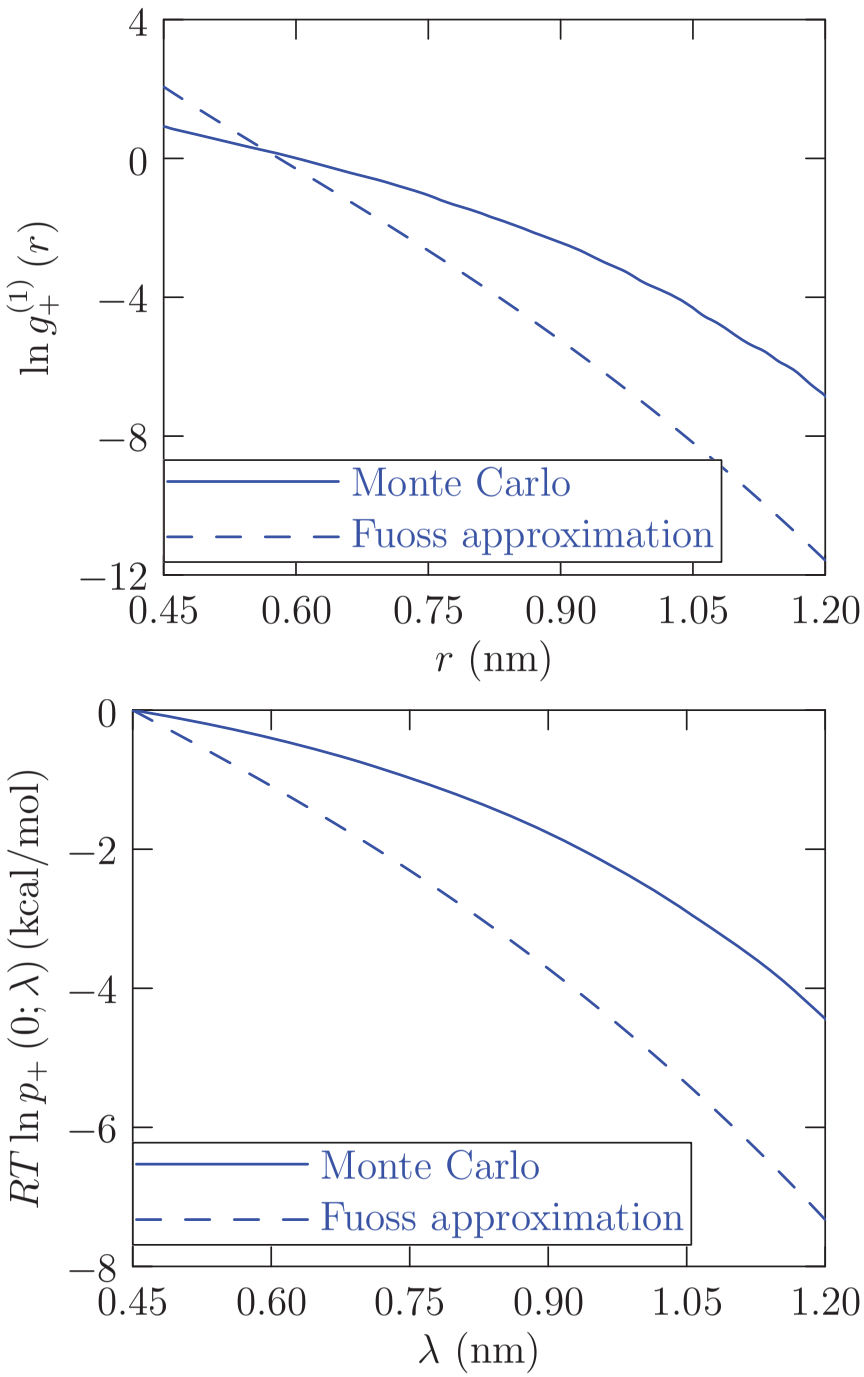

Figure 2.3: Comparison of the Fuoss[78] approximation $\ln g_{\mathrm{B}}^{(1)}(r) = q^2/(\epsilon r k T) - 4\pi\rho \int_{d_{+-}}^{r} \mathrm{e}^{q^2/(\epsilon x k T)} x^2 \mathrm{d}x$ for a 1-1 electrolyte with the primitive model results of FIG. 2.2.

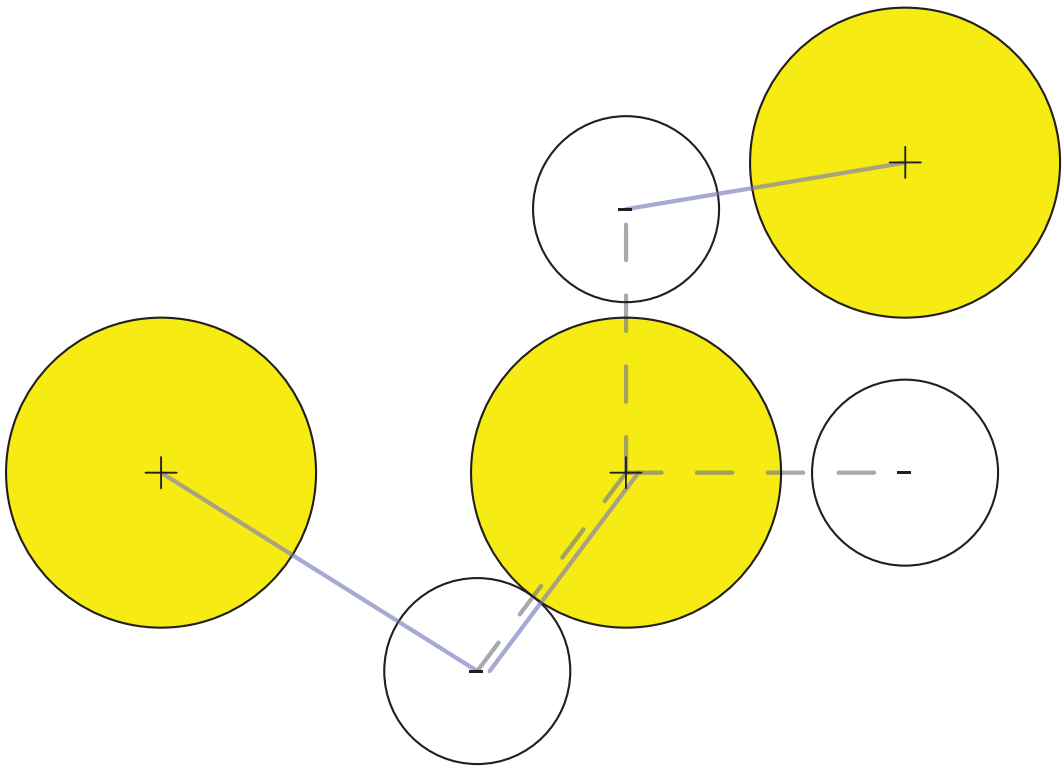

Figure 2.4: An example showing that the distribution of anions nearest to a cation is generally different from the distribution of the cations nearest to an anion. The dashed lines indicate the nearest distances of a cation to each of the three anions. The solid lines mark the nearest distances of a anion to each of the three cations.

with $\langle n(r)\rangle = 4\pi\rho_\gamma \int_0^r g_{\gamma\alpha}(x)x^2\mathrm{d}x$, ρ_γ being the density of γ ions, and $g_{\gamma\alpha}(x)$ the conventional radial distribution function, follows from the assumption of the Poisson distribution for that probability. Evaluating the derivative of Eq. 2.2 using Eq. 2.3 gives

$$\boxed{g^{(1)}_{\gamma|\alpha}(r) \approx g_{\alpha\gamma}(r)\exp\left[-4\pi\rho_\gamma \int_0^r g_{\gamma\alpha}(x)x^2\mathrm{d}x\right] .} \tag{2.4}$$

For $g_{\alpha\gamma}(r) = 1$ (no correlations), this is the Hertz distribution that is correct for that case.[88,89] We recover the Fuoss approximation with $\ln g_{\alpha\gamma}(r) \approx -\beta q_\alpha q_\gamma/\epsilon r = \beta q^2/\epsilon r$ for $r > d_{\alpha\gamma}$, and zero (0) otherwise. This derivation of the Fuoss approximation Eq. (2.1) has been given before. Nevertheless, the suggested approximation Eq. (2.4) is a standard idea in the context of scaled-particle theories of the hard-sphere fluid[89].

As discussed below, the Poisson result Eq. 2.3 follows from a maximum entropy development when the information supplied is the expected occupancy of the inner-shell[90–92] That information is sufficient if the occupancy $n(r)$ is rarely larger than one. Thus, in contrast to the Fuoss approximation, Eq. 2.4 is correct for small r because the expected coordination number tends to zero then. For the same reason, the Poisson approximation Eq. 2.3 is correct at low electrolyte concentration, and even when the solvent is treated at an atomic resolution. Furthermore, it is natural to guess cation-anion chain or ring structures when ionic interactions drive well developed clustering. Fig. 2.2 shows a mean coordination number of less than two for counterion neighbors closer than about 0.5 nm, and supports the chain/ring picture of chain/ring ion clusters formed. It is plausible, therefore, that a choice of inner-shell radii leading to small coordination numbers should validly describe important features of well-developed ion-clustering.

For computational analysis of reactive bimolecular encounters in solution, identification of geometries of closest molecular pairs is critical.[93,94] Because it is correct

for low r in any case, Eq. 2.4 should be regarded as the general resolution of those questions.

When coordination numbers exceed one with a reasonable probability, information on the expected number of pairs of counterions in the inner-shell should improve a maximum entropy model of these probabilities.[90–92] A maximum entropy model involving pair information would predict the $g^{(1)}_{\alpha|\gamma}(r) \neq g^{(1)}_{\gamma|\alpha}(r)$ asymmetry. For a 1-1 electrolyte, the generalization Eq. 2.4 is symmetrical in accord with the Fuoss approximation. The extent to which the observed asymmetry is significant gives an indication whether the Poisson approximation is adequate.

2.2 Results and Discussion

For $TEABF_4$/PC, comparison (Fig. 2.5) of the numerical data with the approximation Eq. 2.4 shows agreement over a distance range wider than the sizes of the molecules as judged by the radial distributions (Fig. 2.2). These near-neighbor distributions show bimodal probability densities with maxima at $r \approx 0.5$ nm and 0.9 nm. These correspond, respectively, to a contact ion pair and to a solvent-separated near-neighbor ion-pair. Thus the Poisson approximation Eq. 2.4 in this case includes a solvation structure in characterizing inter-ionic neighborship.

A plateau between $r \approx 0.5$ nm and 0.9 nm in occupancy probabilities (Fig. 2.6) indicates the saturation of counterion probability, and marks the intershell region. The two sets of probabilities (Fig. 2.6) are qualitatively similar, reinforcing the symmetry of Fig. 2.5. At the distance r indicated by the vertical line, the coordination numbers $n = 1$, 2 predominate, supporting the idea of the formation of cation-anion chain and ring structures. Size distribution of observed ion clusters are shown in FIG. 2.8.

Results (Fig. 2.7) for the primitive model of Fig. 2.2 examine the sufficiency of

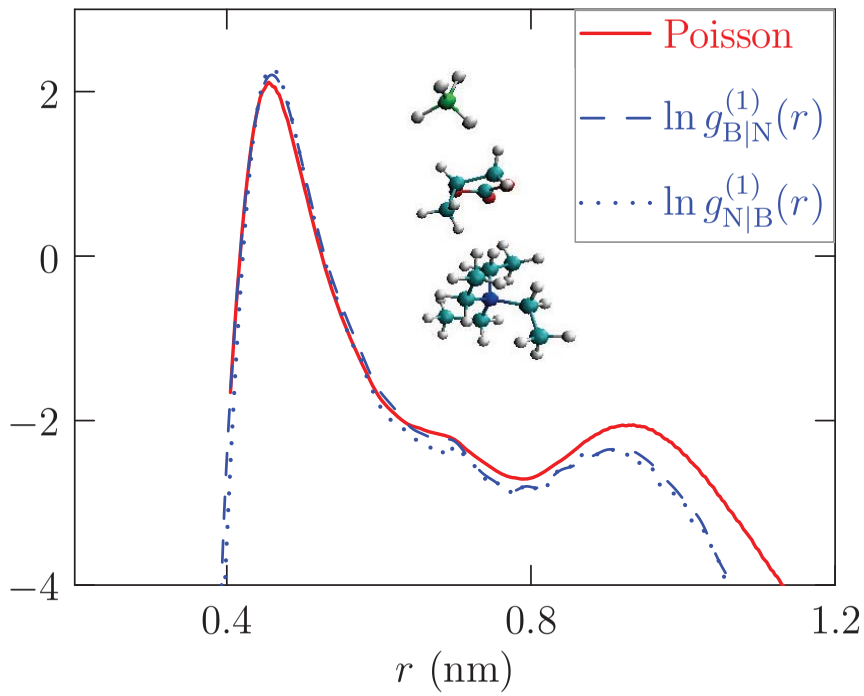

Figure 2.5: For the $TEABF_4$/PC case of Fig. 2.2, comparison of the numerical data with the approximation Eq. (2.4). The local maximum at $r \approx 0.9$ nm identifies solvent-separated nearest-neighbor ion-pairs. In this case, asymmetry of the two observed near-neighbor distributions is slight. That suggests that more elaborate maximum entropy models are unnecessary, and indeed the Poisson approximation is accurate. The embedded molecular graphic shows one of the solvent-separated nearest-neighbor BF_4^-...PC ...TEA^+ structures observed.

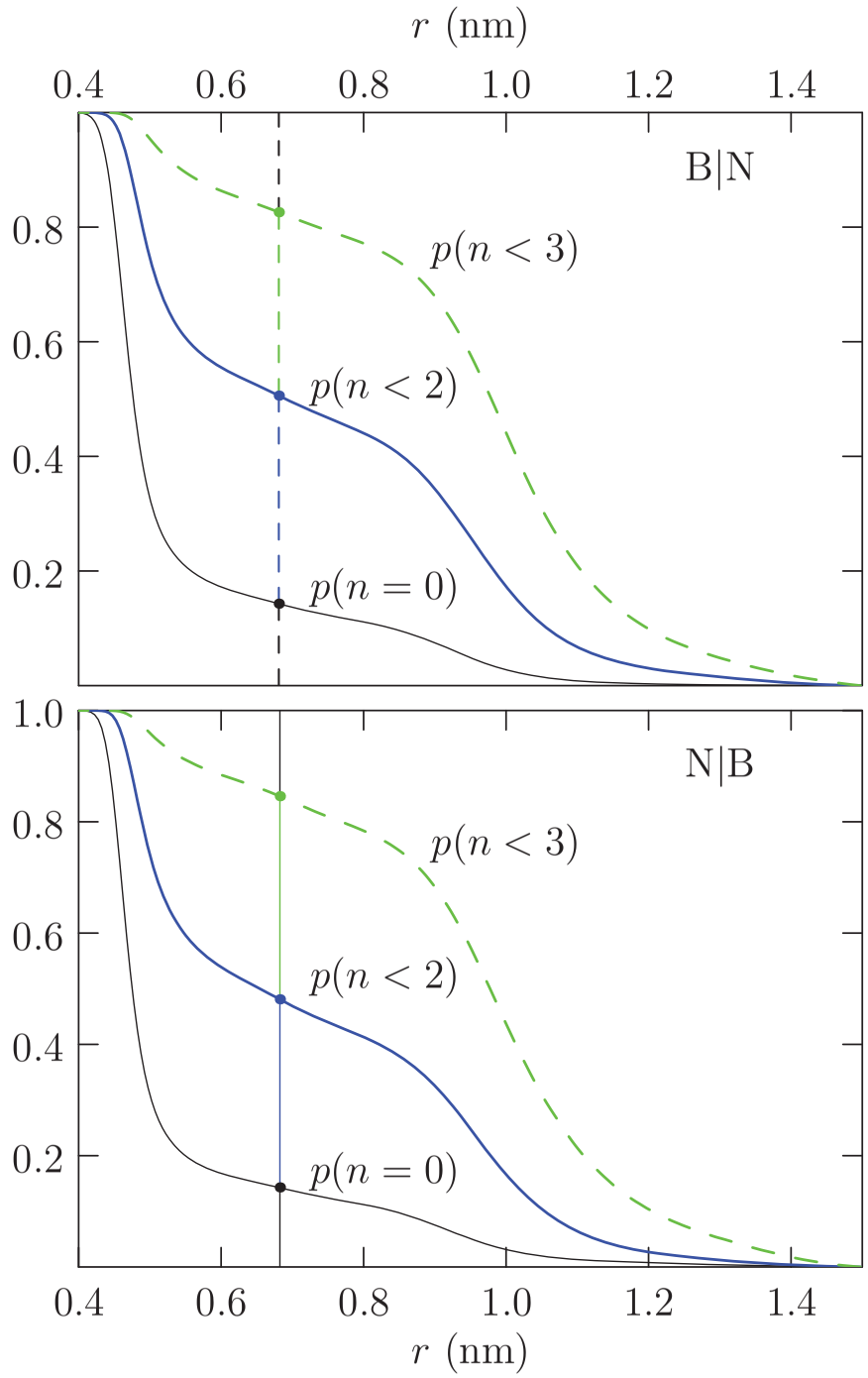

Figure 2.6: Occupancy probabilities as functions of the observation sphere radii r for the $TEABF_4$/PC case of Fig. 2.2. Upper panel: probabilities for occupancy by the B-atom of the $BF_4{}^-$ anion of the inner-sphere of the N-atom of tetra-ethylammonium cation (TEA^+). Lower panel: probabilities for occupancy by the N-atom of the cation of the inner-sphere of the B-atom of the anion. The curves lowest in each panel are similar, showing symmetry displayed also in Fig. 2.5.

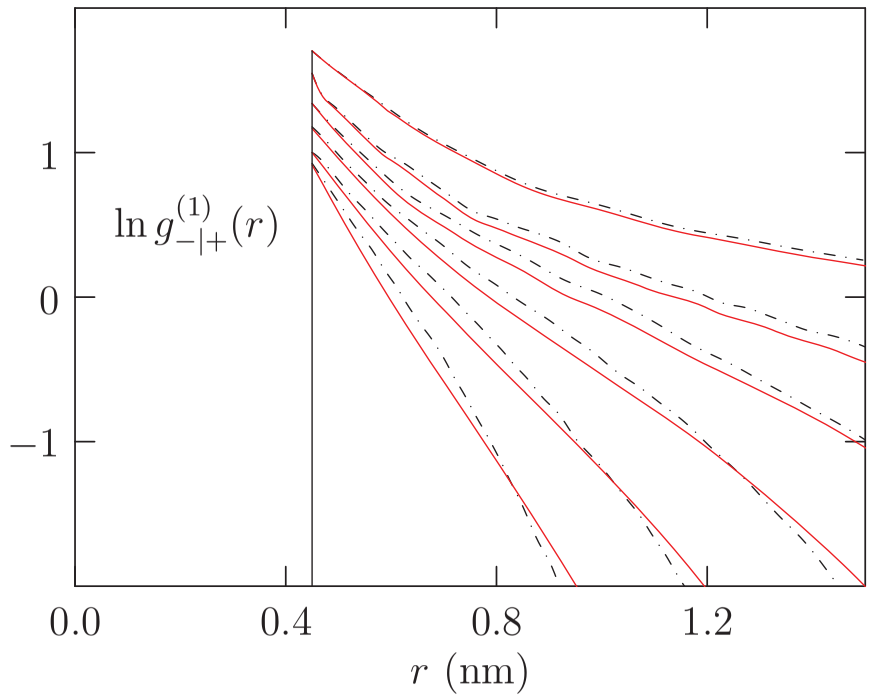

Figure 2.7: Dashed curves are Monte Carlo results for the primitive model of Fig. 2.2 and the solid lines are the Poisson approximation, Eq. (2.4). From top to bottom, the distinct cases correspond to concentrations 0.01, 0.05, 0.10, 0.20, 0.40, and 0.80 mol/dm^3, T = 300K for each case. For the highest concentration, the system size is 2×400 ions. For all other cases, the system size is 2×200 ions. At the lowest concentration here the distribution of the nearest neighbor $g^{(1)}_{-|+}(r)$ is close to the full radial distribution function $g_{+-}(r)$.

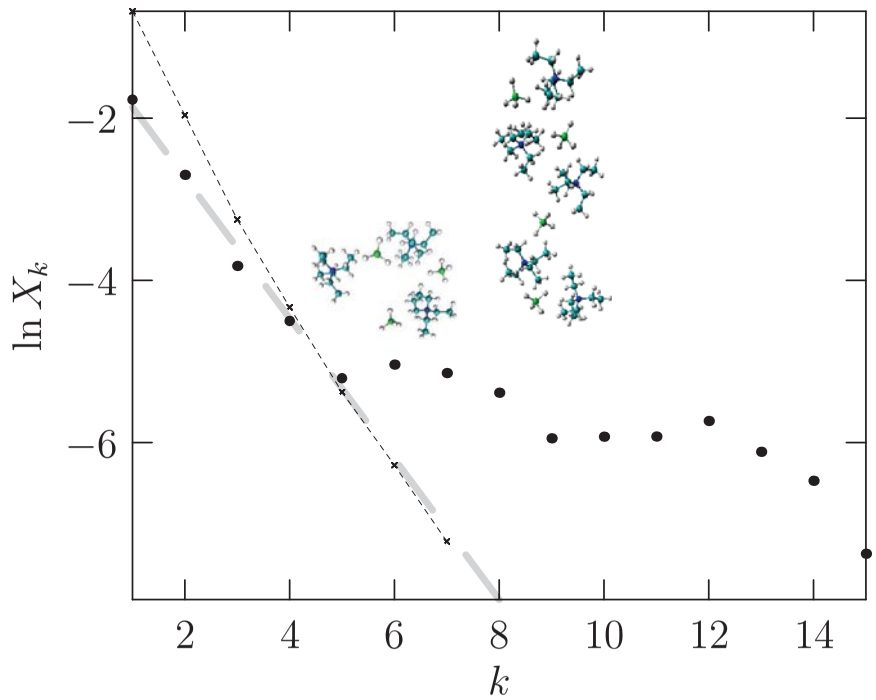

Figure 2.8: Observed size distribution for global clusters, with $\lambda = 0.6$ nm adopted as the clustering radius. $X_k = \rho_k/2\rho$ with ρ_k the number density of k-mers and ρ the salt number density (concentration), so that $\sum_k kX_k = 1$. The dotes are for the atomically detailed simulation; the largest cluster observed was $k = 64$. Note the fraction of free ions obtained here is the same as that inferred from FIG. 2.6. The crosses are for the primitive model calculation (FIG. 2.2, lower panel). There the largest cluster observed was $k = 15$. Note that the fraction of unassociated ions ($k = 1$) is significantly different between the two models.

the Poisson approximation over a broader concentration range for such models. The nearest-neighbor distributions are unimodal in this case. Correct at small r, where the probability densities are highest and properly normalized, the Poisson approximation Eq. 2.4 is accurate over the whole range shown.

Another example is the ionic liquid [Bmim][BF_4], performed by Peixi Zhu. The numerical data showed the expected asymmetry, which can be treated by a maximum entropy model based on the expected number of pairs of counter ions occupying the inner-shell of the central ion.

2.3 Maximum Entropy Modeling

The Poisson distribution $\hat{p}(n) = \langle n \rangle^n \exp^{-\langle n \rangle} / n!$ describes random occupancy consistent with the information $\langle n \rangle = \langle n(r) \rangle$. Considering the relative entropy

$$\eta(\{p(n)\}) = -\sum_{n \geq 0} p(n) \ln\left(\frac{p(n)}{\hat{p}(n)}\right) , \tag{2.5}$$

the Poisson distribution is the maximum entropy distribution satisfying the specific expected occupancy. If we have more information, e.g., the binomial moments[90–92]

$$\left\langle \binom{n}{j} \right\rangle = \sum_{n \geq 0} p(n) \left(\frac{n!}{(n-j)!j!} \right) , \tag{2.6}$$

we can seek the distribution which maximizes $\eta(\{p(n)\})$ and satisfies the broader set of information.

With the binomial moments (Eq. 2.6), the Poisson distribution is seen to be correct if realized values of n are rarely bigger than one. If n is never 2 or larger, binomial moments $j \geq 2$ vanish. When binomial moments are small for j as large as 2 that is consistent with the Poisson prediction that they are zero. This underlies our observation above the the Poisson model, $p(0) \approx \exp^{-\langle n \rangle}$ of Eq. 2.3 is correct for

small $\langle n \rangle$.

Beyond the mean occupancy, the next level of information is the pair-correlation information $\langle n(r)\,(n(r)-1)\,/2 \rangle$, the expected number of pairs of counterions in the indicated inner-shell. Maximizing for the case that pair information is available induces the model $p(n) \propto \exp\left[-\lambda_1 n - \lambda_2 n(n-1)/2\right]/n!$, where λ_1, and λ_2 are Lagrange multipliers adjusted to reproduce the information $\langle n \rangle$ and $\langle n\,(n-1)\,/2 \rangle$. Explicitly addressing the normalization of these probabilities leads to

$$p\,(n) = \frac{\frac{1}{n!}\mathrm{e}^{(-\lambda_1 n - \lambda_2 n(n-1)/2)}}{1 + \sum_{m \geq 1} \frac{1}{n!}\mathrm{e}^{(-\lambda_1 m - \lambda_2 m(m-1)/2)}}\ , \tag{2.7}$$

$$\ln p\,(0) = -\ln\left[1 + \sum_{n=1}^{\infty}\left(\frac{1}{n!}\right)\mathrm{e}^{-\lambda_1 n - \lambda_2 n(n-1)/2}\right]\ . \tag{2.8}$$

$p\,(0)$ involves only the denominator of Eq. 2.7, which can be considered as a partition function sum over occupancy states with n-dependent interactions and interaction strengths adjusted to satisfy the available information.

2.4 Conclusions

Results for $TEABF_4$/PC (Fig. 2.2) identify a natural clustering radius where mean coordination numbers are near two. This suggests arrangements of the closest neighbors leading to a structural motif of cation-anion chains and rings. In contrast to the atomically detailed $TEABF_4$/PC results, a corresponding primitive model (Fig. 2.2) does not display those clustering signatures (Fig. 2.7). A generalization (Eq. (2.4)) of the Fuoss ion-paring model was obtained by recognizing that the Poisson distribution is correct when the mean coordination numbers are low. On the

basis of measurable molecular distribution functions, this generalization also establishes the distribution of molecular nearest-neighbors for the computational analysis of bimolecular reactive processes in solution. This Poisson-based model is accurate for the $TEABF_4$/PC results, both for the primitive model and the atomically detailed case. For $TEABF_4$/PC, the atomically detailed numerical results and the statistical model identify *solvent-separated* nearest-neighbor ion-pairs. Distributions of nearest-neighbor distances typically depend on which ion of a pair is taken as the central ion, *i.e.,* the distribution of anions nearest to a cation is different from the distribution of the cations nearest to an anion. The Poisson-based model is *not* asymmetric in that way.

2.5 Methods

2.5.1 Molecular dynamics simulation

The simulations were performed with AMBER9.[95] Partial charges are assigned to atomic sites of tetra-ethylammonium (TEA^+) and tetra-fluoroborate ($BF_4{}^-$) ions from Luzhkov, *et al.*[96] and Andrade, *et al.*[97], respectively. All the other parameters are taken from general AMBER force field (GAFF).[98] Trajectories were constructed with a time step of 2 fs, using the isothermal-isobaric (NPT) ensemble with the Langevin thermostat. Temperature and pressure were 300K and 1 atm. Electrostatic interactions were calculated using particle mesh Ewald with a grid spacing of 1 Å. Separate calculations on homogeneous liquid propylene carbonate verified that this model gives an accurate value for the linear-response dielectric constant and its temperature dependence.[99]

2.5.2 Non-additive primitive model

The primitive model was produced by Monte Carlo simulation of a neutral system of hard spherical ions in conventional cubical periodic boundary conditions at $T = 300$ K, $p = 1$ atm, the concentration was ranged from 0.01 to 1 mol/dm^3. Ion charges and sizes are matched to the $TEABF_4$/PC MD simulation. Specifically the model dielectric constant is $\epsilon = 60$, and $d_{++} = 0.6668$ nm, $d_{--} = 0.6543$ nm, $d_{-+} = 0.45$ nm are distances of closest approach for the hard spherical ions. Simulation utilized the Towhee[76] package adapted to the present system.

Chapter 3

Interfacial Properties of PC

3.1 Introduction

Unique properties of nanomaterials, and specifically of electrochemical double-layer capacitors (EDLC) based on carbon nanotube (CNT) forests,[1] arise from their large surface areas. Accurate descriptions of interfaces is an important challenge for modeling. Here we considered propylene carbonate (PC: FIG. 3.1) as a solvent for electrochemical double-layer capacitors, reporting experimental and molecular simulation results on PC interfaces. This validation is preparatory to direct simulation of dynamical filling and performance of CNT-based EDLCs.

Differential filling of a charged nanotube forest from a bulk electrolyte solution is expected to be sensitive to the balance of attractive intermolecular interactions. A possible concern for the first simulations of CNT-based EDLCs was that models of the PC solvent had not been parameterized to describe contact with carbon electrodes.[75,100] An initial molecular dynamics calculation showed complete spreading of the modelled liquid PC on graphite,[101] in disagreement with experimental observation of a PC droplet on graphite reported below. That experience[102] suggested the advantage of studying PC interfaces in validation of simulation models for electrochemical applications. The present work adjusts the Lennard-Jones interactions

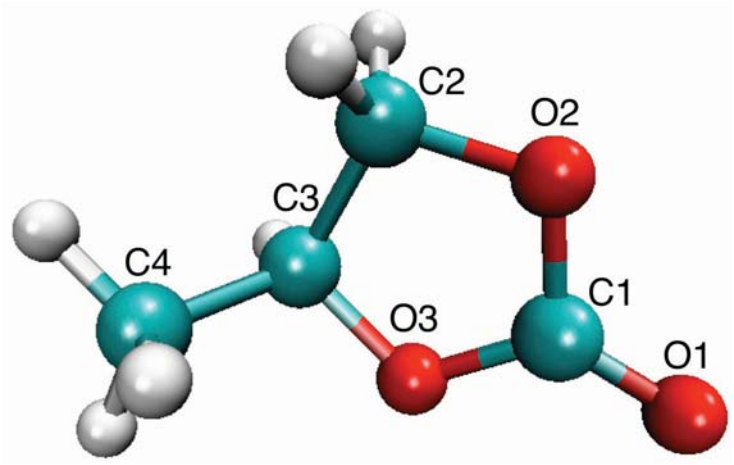

Figure 3.1: Propylene carbonate (PC) enantiomer with atom labelling used in this chapter.

with the graphitic carbon to agree with the observed contact angle.

Propylene carbonate is a non-reactive, low-toxicity, aprotic, highly polar dielectric solvent widely used in nonaqueous electrochemical systems. Simulation of interfaces of non-aqueous solvents for electrolytes, acetonitrile[103,104] and propionitrile,[105] have been previously carried-out. Helpful molecular simulations[75,106,107] of the uniform liquid propylene carbonate solvent are also available. A variety of molecular dynamics results are discussed below.

3.2 Results and Discussion

3.2.1 Droplet-on-graphite contact angle

The observed contact angle (FIG. 3.2) is acute. This indicates good wetting and favorable PC:graphite interactions, though not the complete spreading that was obtained[101] from simulation with initial models.[75,100] Trial-and-error (Sec. 3.4.1) found a simulation contact angle of about 31° with a 40% lowering of the strength of Lennard-Jones interactions associated with the C atoms of the graphite substrate (FIG. 3.3).

Figure 3.2: PC droplet on graphite. Contact angle measurements of 5 μl propylene carbonate drops on a bulk pyrolytic graphite disc (Grade: PG-SN, Graphitestore.com) were performed under ambient conditions using a Rame-Hart contact angle goniometer. The graphite disc was sheared against a paper wipe (Kimwipe) to reveal a fresh surface. The surface was then rinsed with water and allowed to air dry. A static contact angle of 31.4±1.6° was obtained from 3 trials

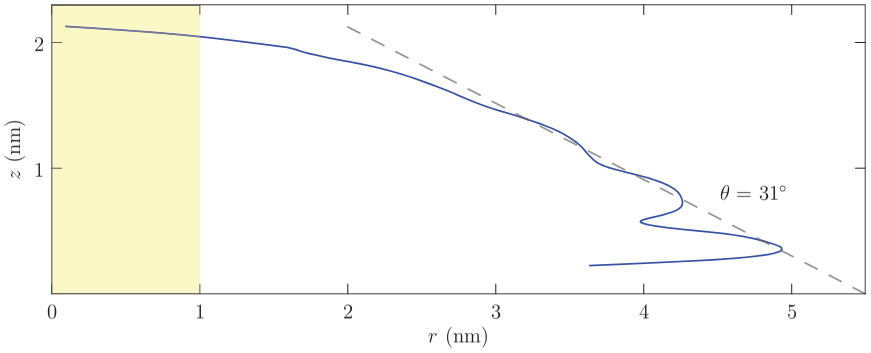

Figure 3.3: Silhouette of the droplet, suggesting an Aztex pyramid.[108,109] $T = 300$K (check). The procedure for obtaining this silhouette[110] is detailed in the Methods. The suggested contact angle is found by fitting a straight line to the region 3.0 nm $< r <$ 4.2 nm. The shaded region identifies the cylinder used to investigate the layering of the mean density in Fig. 3.4.

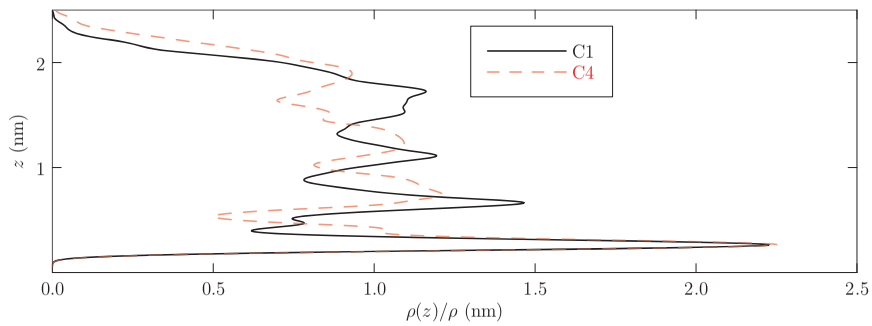

Figure 3.4: The density, relative to the bulk density, in the central plug of material indicated by the shaded region of Fig. 3.3. Atom layers nearest to the graphite are concordant. The density oscillations of C1 and C4 atoms conflict at larger distances from the graphite, and C4 slightly prevails furthest from the graphite.

Simulations of water on graphite surfaces show that changing the number of water molecules from 1000 to over 17,000 has only a small effect on the contact angle.[110] A droplet size dependences of such results are often ascribed to a line-tension effect. The fine structure observed here in the three-phase contact region here would make definition and further investigation of a triple line complicated. Together with the distinctly non-spherical molecular shape and packing pattern (studied below), interesting structural transitions of PC molecules near *charged* electrodes are expected; those issues should be the subject of future studies.

The millimeter length scales of the experimental observation differ by 10^6 from nanometer length scales treated by the calculation. Pore radii for ECDL capacitors are in the nanometer range. Therefore, the nano-scale fine-structure of the molecular dynamics result (FIG. 3.4) should be relevant to the anticipated studies of EDCLs.

3.2.2 Liquid-vapor interfacial tensions

Surface tensions were evaluated from simulations in slab geometry (FIG. 3.5) at several temperatures. The PC liquid-vapor interfacial tensions (FIG. 3.6) agree accurately with experimental values (TABLE 3.1) at moderate temperatures. The simple formula $\gamma(T) \sim \gamma_0 \left(\frac{T-T_c}{T_c}\right)^{5/4}$, utilizing an approximate estimate of the critical

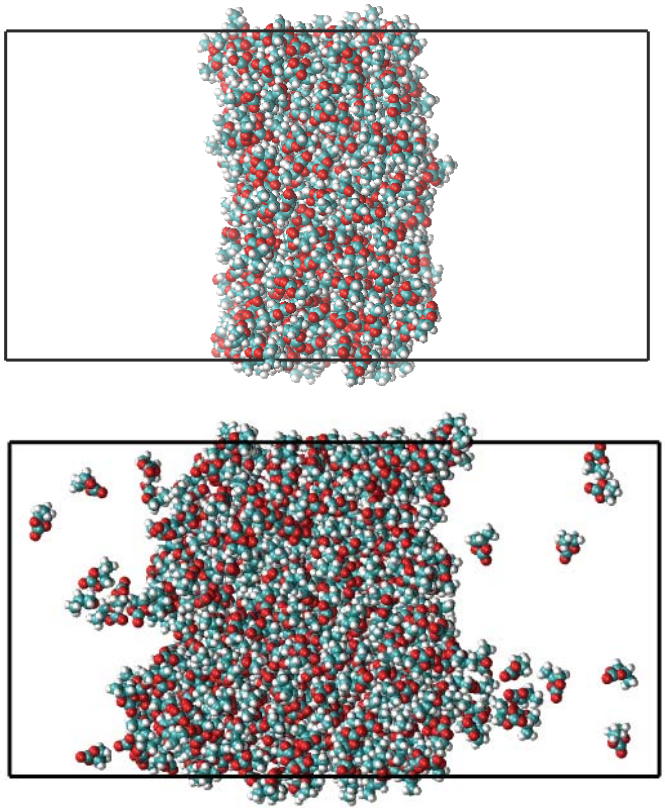

Figure 3.5: Slab geometry, upper configuration from T=300K simulation, lower configuration from T=600K simulation.

exponent, extrapolates to $\gamma \to 0$ at $T_c \approx 740$K (FIG. 3.6).

3.2.3 Liquid-vapor interfacial structure

For the lowest temperatures considered here, the interfacial profiles of the atomic densities are distinctive (FIG. 3.7): non-monotonic except for the density of the propyl carbon (C4). The coincidence of the positive lip in atom densities other than C4 with the deficit in the C4 density suggests that the PC molecule lies approximately flat on this interface while projecting C4 further toward the vapor. Direct interrogation of the orientations of molecules with z_{C1} >1.5 nm (FIG. 3.7) confirms this view (FIG. 3.8).

Table 3.1: Experimental surface tension at 20C is 41.1 dyne/cm.[111] Except at the highest temperature, vapor densities ρ_{vap} were obtained from the WHAM calculations specified in Sec. 3.4.3, and Fig. 3.13.

T(K)	ρ_{liq} (nm^{-3})	ρ_{vap} (nm^{-3})	$-kT \ln\left(\frac{\rho_{\text{liq}}}{\rho_{\text{vap}}}\right)$ (kcal/mol)	$\rho_{\text{vap}} kT$ (bar)	p (bar) [exp][112]	γ (dyne/cm)
300	7.11	1.6e-6	-9.2	6.2e-5	7.6e-5	40.8
400	6.46	4.8e-4	-7.6	2.6e-2	2.8e-2	29.9
600	4.93	7.0e-2	-5.1	5.8	4.9	9.7

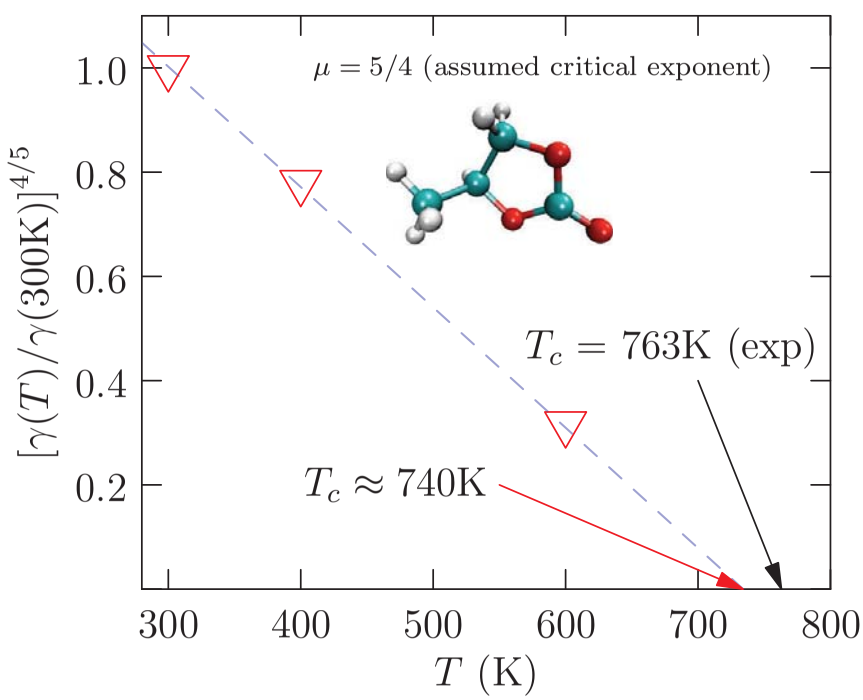

Figure 3.6: Surface tensions $\gamma = \frac{1}{2}\int \left\{p_{zz}(z) - \frac{1}{2}\left[p_{xx}(z) + p_{yy}(z)\right]\right\} \mathrm{d}z$. The experimental critical temperature[112] is $T_c = 763$ K, whereas the triple temperature is about $T_{\text{triple}} \approx 220$ K.

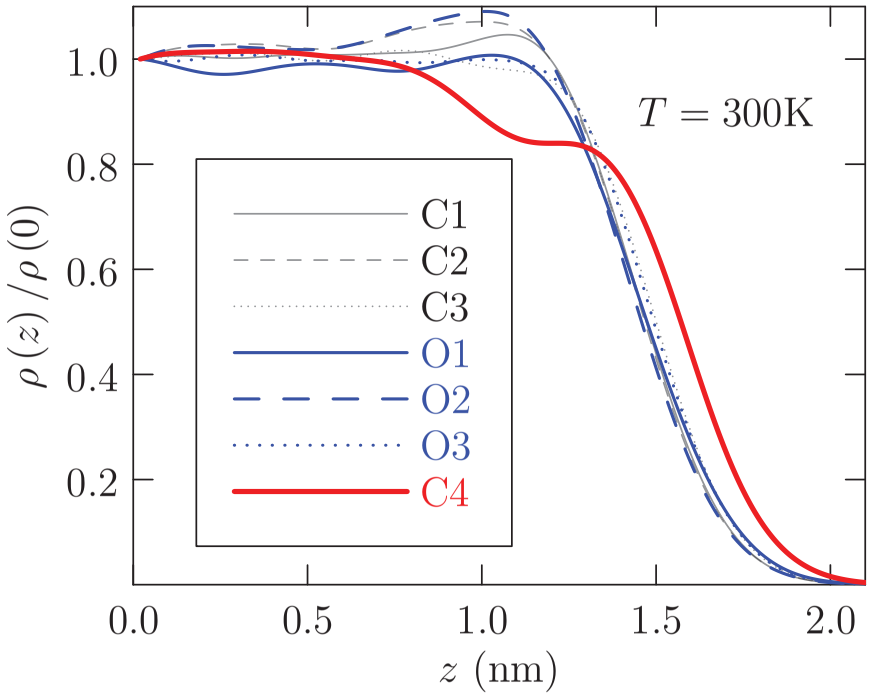

Figure 3.7: Evidently the carbonate plane lies down on the surface, projecting C4 out of the liquid.

3.2.4 Structure of the coexisting liquid

The atom-atom intermolecular radial distribution functions (FIGS. 3.9 and 3.10) supplement the view that an important packing motif stacks carbonate planes of close PC neighbors with the outer (O1) oxygen of one molecule snuggled into the positively charged propyl end of another molecule so that neighboring molecule dipole moments are approximately antiparallel. Such an arrangement is similar to the known crystal structure of ethylene carbonate,[114] and to the PC dimer structures established by electronic structure calculations.[107]

On the basis of the C1C1 joint distribution (FIG. 3.10), the nearest two neighbors of a C1 are physically distinct, imperfectly stacked on top and bottom of the carbonate plane. The *closest* C1 neighbor of a C1 atom is most probably at a radial displacement of 0.38 nm (FIG. 3.10). The observed distribution of the *closest* C1

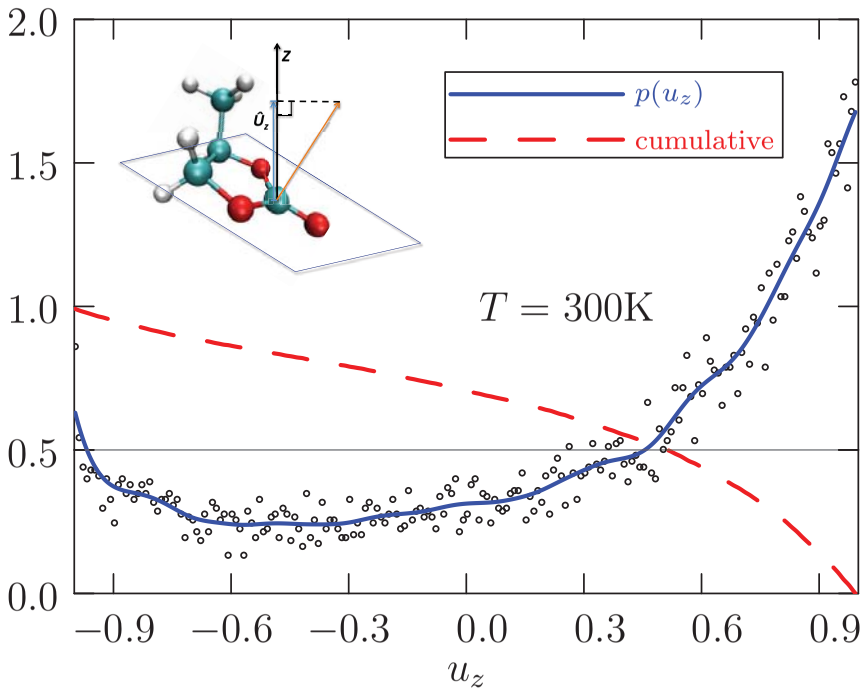

Figure 3.8: In the liquid-vapor outer interfacial layer, the probability density and cumulative probability for projection of unit vector normal to the carbonate (-CO_2-) plane onto the z-axis, perpendicular to the interface. In this interfacial layer, the most probable orientation aligns the carbonate plane parallel with the plane of the interface, with the C4 methyl group extended toward the vapor phase. About 50% of the observations of a PC molecule have $u_z > 0.5$ ($\theta < 60°$).

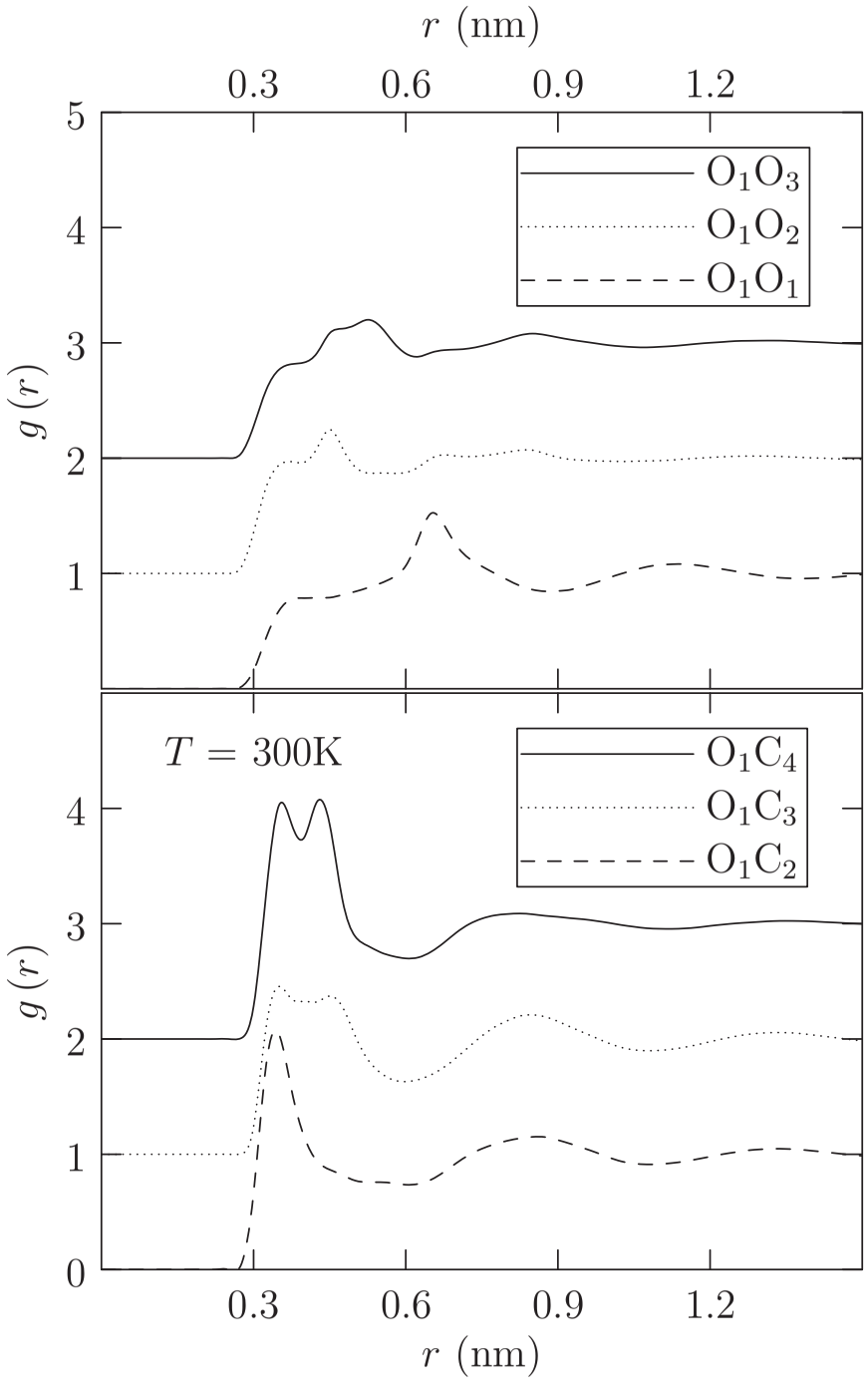

Figure 3.9: Structured close-contacts involve negatively charged O1 with the opposite end of the PC molecule. Intermolecular radial distribution functions between heavy atoms in PC at $T = 300$K, 400K and 600K are showed in Appendix D.

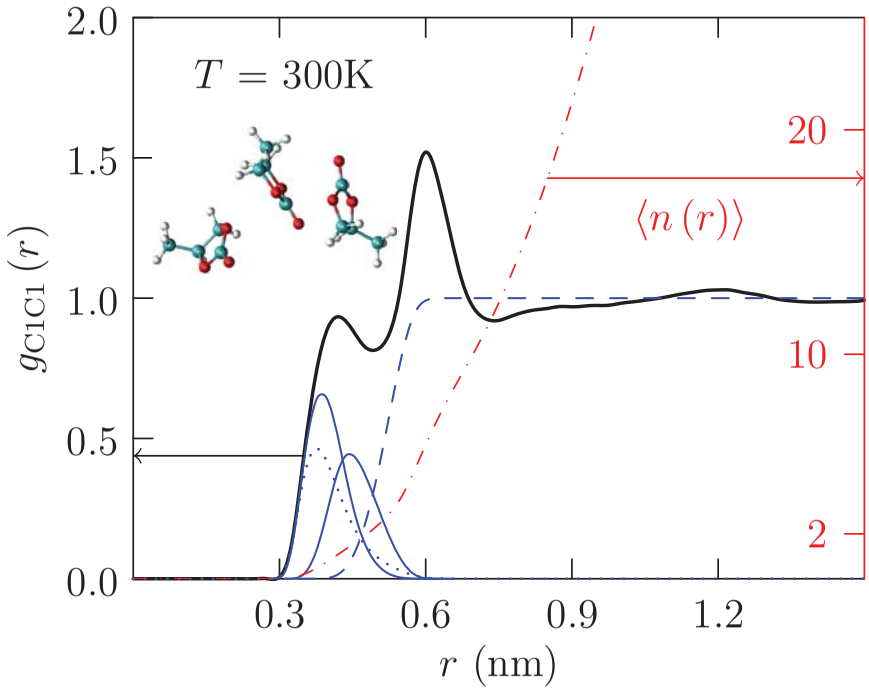

Figure 3.10: Taking C1 as the center of the PC molecule, this characterizes the packing of centers, with molecular coordination numbers of 10 - 12. The solid blue curves are the radial distribution functions for the *closest*, and *2nd-closest* C1 neighbors of a C1 atom, peaked at 0.38 nm and 0.44 nm, respectively. The dotted curve is the estimate of the radial distribution of the *closest* C1 neighbor of a C1 atom based on the Poisson approximation.[113] The dashed blue curve is the probability, with median point of about 0.52 nm, that a central C1 atom has more than two (2) C1 neighbors within that radius. The closest C1-C1 contacts are associated with stacking, with substantial disorder, of carbonate planes as suggested by the embedded molecular graphic.

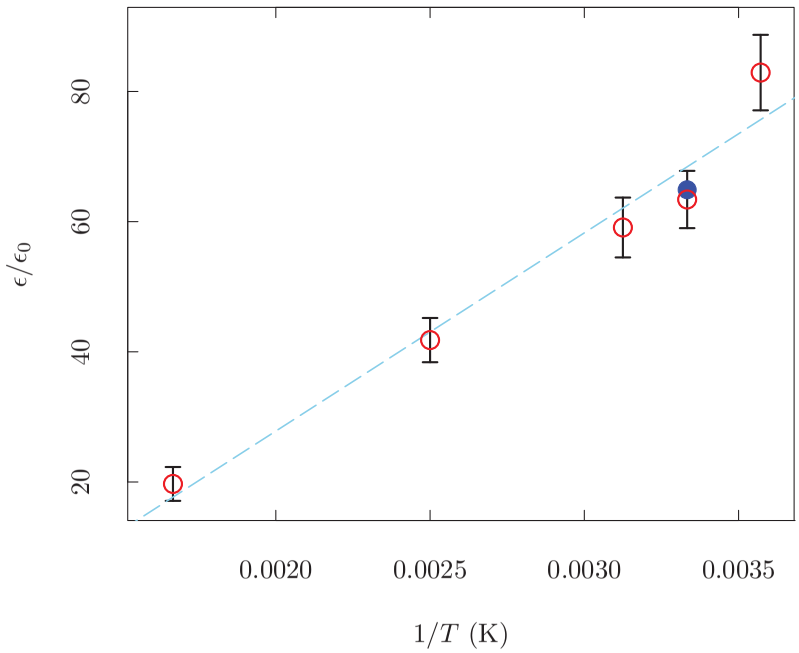

Figure 3.11: Dielectric constant of model propylene carbonate, evaluated following standard simulation methods.[75,115] The calculation treated 600 PC molecules under periodic boundary conditions using AMBER GAFF force field. Resulting values were averaged from the 40 ns production trajectories at constant pressure of 1 atm. The solid dot is the experimental result at 25C, $\epsilon/\epsilon_0 = 64.9$.[116] Numerical values are given in TABLE 3.2.

neighbor of a C1 atom (FIG. 3.10) is more strongly peaked than the simple Poisson-based estimate.[113]

The dielectric constant of uniform PC liquid implied by these simulations (FIG. 3.11) agrees satisfactorily with experiment.

3.2.5 Balance of excluded volume and attractive interactions

Thermodynamic energies for liquid PC may be analyzed on the basis of quasi-chemical theory[117? –120] in which the paramount goal is molecular-scale physical clarity from thermodynamic characteristics. The quasi-chemical approach focuses

on binding energies, $\varepsilon = U(N) - U(N-1) - U(1)$, of individual molecules and introduces a conditioning based on definition of an indicator function,[?] χ, so that $\chi = 1$ defines a logical condition or constraint that physically simplifies that statistical thermodynamic problem.[120]

For example, if close neighbors set particularly important or complicated or *chemical* interactions, then the logical $\chi = 1$ can indicate the absence of neighbors in a specified local region. Indeed, for numerous applications to liquid water,[118–124] $\chi = 1$ indicates that there are no O-atoms of bath molecules within a specified radius from the O-atom of a distinguished water molecule. Then $\chi = 0$ if any solvent molecule *is* present in that inner-shell. For the application to CF_4(aq)[?], $\chi = 0$ if any water molecule is in defined van der Waals contact with the polyatomic CF_4 solute.

With such a indicator function χ specified, the partial molar Gibbs free energy in *excess* over the ideal contribution, $\mu^{(\mathrm{ex})} = \mu - \mu^{\mathrm{ideal}}$, can be expressed as

$$\beta\mu^{(\mathrm{ex})} = -\ln\langle\langle\chi\rangle\rangle_0 + \ln\int \mathrm{e}^{\beta\varepsilon} P(\varepsilon|\chi = 1)\mathrm{d}\varepsilon + \ln\langle\chi\rangle \ , \tag{3.1}$$

with $\beta^{-1} = k_{\mathrm{B}}T$. A principal virtue of this formulation[120] is that is subsumes a van der Waals picture of the solvation without requiring that intermolecular interactions of different types be expressed is some specific format. We will use this formulation here to distinguish packing contributions from longer-ranged interactions that are attractive on balance. The notation $\langle\ldots\rangle$ indicates the usual average over the thermal motion of the system. The notation $\langle\langle\ldots\rangle\rangle_0$ indicates the average over the thermal motion of the system *together* with an additional molecule with no interaction between them, thus the subscript 0. $\langle\langle\chi\rangle\rangle_0$ is then the probability that the defined inner-shell is empty in the case that interactions between the distinguished molecule and the solution are absent. That contribution thus gauges the free energy cost of finding space for positioning the additional PC molecule in the liquid.

More broadly, these formalities follow from the identity[118,122]

$$\frac{\left\langle e^{\beta\varepsilon}\chi\right\rangle}{\langle\chi\rangle} = e^{\beta\mu^{(\mathrm{ex})}}\frac{\langle\langle\chi\rangle\rangle_0}{\langle\chi\rangle} \ , \tag{3.2}$$

which is a disguised expression of the *rule of averages.*[125?] This broader observation Eq. (3.2), might permit design of weight functions χ for improved numerical performance.[118]

$P(\varepsilon|\chi = 1)$ that appears in Eq. (3.1) is the probability distribution of the binding energies, and is conditional on an empty inner-shell. That conditioning can make $P(\varepsilon|\chi = 1)$ simple enough that a Gaussian (or normal) approximation suffices.[121?] The observed behavior of $P(\varepsilon)$ (FIG. 3.12) already suggests that possibility. Accepting that Gaussian approximation

$$\beta\mu^{(\mathrm{ex})} \approx -\ln\langle\langle\chi\rangle\rangle_0 + \beta\langle\varepsilon|\chi = 1\rangle + \beta^2\left\langle\delta\varepsilon^2|\chi = 1\right\rangle/2 + \ln\langle\chi\rangle \ . \tag{3.3}$$

For conceptual clarity, let us discuss how definition of χ might be approached. χ=1 corresponds to the absence of van der Waals contact of the distinguished PC molecule with the solution. We might chose to define χ by assigning van der Waals radii for all atom types. The results of FIGS. 9 and 10, characterizing close atom-atom pair distances, and particularly distance ordered contributions of FIG. 10 would be directly relevant for that. We would adjust those radii assignments to realistically large values, while targeting values of $\langle\chi\rangle$ not too different from one.

With this conceptual background, Eq. (3.3) becomes

$$\beta\mu^{(\mathrm{ex})} \approx -\ln\langle\langle\chi\rangle\rangle_0 + \beta\langle\varepsilon\rangle + \beta^2\left\langle\delta\varepsilon^2\right\rangle/2 \ . \tag{3.4}$$

This result is interesting for several reasons. Though it is suggestive of a van der

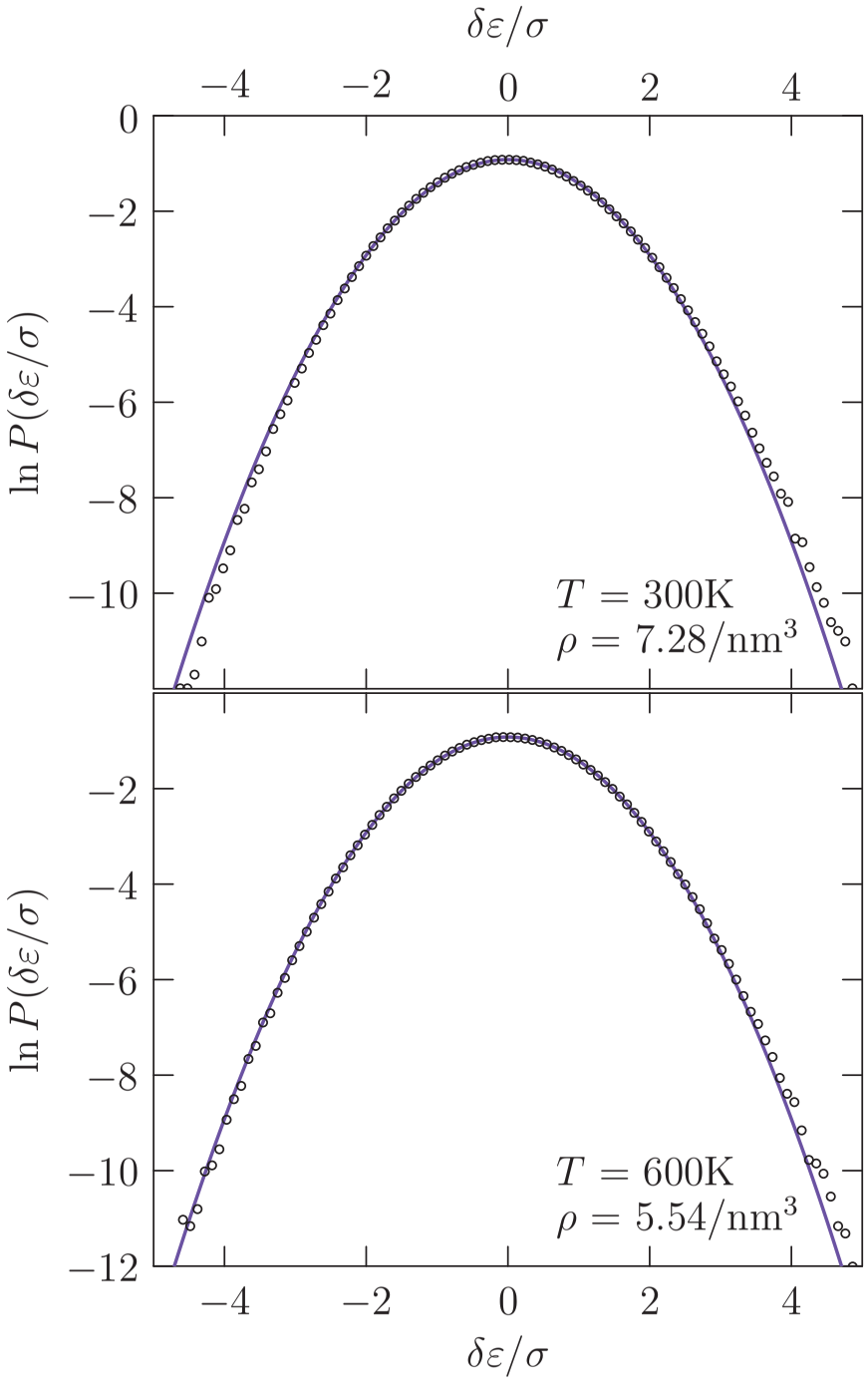

Figure 3.12: Binding energies, centered and scaled $\delta\varepsilon = \varepsilon - \langle\varepsilon\rangle$ and $\sigma^2 = \langle\delta\varepsilon^2\rangle$, are approximately normally distributed. The slight super-gaussian behavior on the crucial right-side of these plots is the signature of repulsive intermolecular interactions.

Waals treatment, it is not limited to a first-order mean-field contribution, and additionally the assessment of attractive interaction is made on the basis of observations for the case that those interactions are actually operating. Nevertheless, the *packing* contribution $-\ln\langle\langle\chi\rangle\rangle_0$ is typically difficult to calculate directly.

To quantitatively characterize the effort to obtain that packing contribution, here we focus on getting an estimate on the basis of the present methods. With observation of the density of the vapor phase (FIG. 3.13), we can get the desired free energy on the saturation curve[125]

$$\beta\mu_{\rm liq}^{\rm (ex)} = \beta\mu_{\rm vap}^{\rm (ex)} - \ln\left(\frac{\rho_{\rm liq}}{\rho_{\rm vap}}\right) \ . \tag{3.5}$$

Our intention (tested below) is to assume that the vapor phase is approximately ideal, $\beta\mu_{\rm vap}^{\rm (ex)} \approx 0$. The result Eq. (3.5) applies to the coexisting liquid. For the thermodynamic states of TABLE 3.2, at the same temperature but slightly different pressures, we apply the correction

$$\beta\mu_{\rm liq}^{\rm (ex)} \approx -\ln\left(\frac{\rho_{\rm liq}}{\rho_{\rm vap}}\right) + \beta\left(\frac{\partial\mu}{\partial p}\right)_T \Delta p - \ln\left(\frac{\rho}{\rho_{\rm liq}}\right) \ . \tag{3.6}$$

Of course $\beta\left(\partial\mu/\partial p\right)_T \Delta p = \beta\Delta p/\rho_{\rm liq}$; at T=300K (TABLE 3.2) this term is about 0.003 and we neglect it. The rightmost term of Eq. (3.6) extracts the ideal contribution to the chemical potential change. Collecting all, we find that

$$-\ln\langle\langle\chi\rangle\rangle_0 \approx -\ln\left(\frac{\rho}{\rho_{\rm vap}}\right) - \beta\langle\varepsilon\rangle - \beta^2\left\langle\delta\varepsilon^2\right\rangle/2 \ , \tag{3.7}$$

characterizes the net effect of intermolecular excluded volumes when the vapor pressure is low.

Except for the highest temperature considered, the ideal estimate of the vapor

pressure is low and close to the experimental vapor pressure (TABLE 3.1), so the assumption of ideality of the vapor is accurate then. At T=600K, the vapor pressure is substantial but the ideal estimate of the vapor pressure is still within about 20% of the experimental vapor pressure.

We therefore estimate the packing contribution $-k_{\mathrm{B}}T \ln \langle\langle\chi\rangle\rangle_0 \approx 15$ kcal/mol at 300K, and 14 kcal/mol at 400K. Thus volume exclusion effects contribute to the solvation free energies at the level of about 2/3rds of the magnitude of the attractive interactions (TABLE 3.2), of course with opposite sign, when the vapor pressure is low. At 300K, $\langle\langle\chi\rangle\rangle_0 \approx 1 \times 10^{-11}$.

Attractive interactions stabilize the liquid of course. van der Waals attractions make a larger contribution to the mean binding energies (TABLE 3.2) than do electrostatic interactions. Contrariwise, electrostatic contributions dominate van der Waals attractions in the variances of binding energies.

If electrostatic interactions are considered solely, then at the lowest temperature the mean and variance electrostatic contributions are roughly in the 2:1 proportion that is a symptom of satisfactory Gaussian models of solvation. If the distributions of binding energies are precisely Gaussian, then

$$\langle\langle\varepsilon\rangle\rangle_0 = \langle\varepsilon\rangle + \beta \left\langle \delta\varepsilon^2 \right\rangle \ . \tag{3.8}$$

This follows from the general requirement that [125]

$$P(\varepsilon) = \mathrm{e}^{-(\varepsilon-\mu^{\mathrm{ex}})} P^{(0)}(\varepsilon) \tag{3.9}$$

where $P^{(0)}(\varepsilon)$ is the distribution of binding energies for the uncoupled case associated with the $\langle\langle\ldots\rangle\rangle_0$ averaging. Setting $\langle\langle\varepsilon\rangle\rangle_0 = 0$ for electrostatic interactions, then the 2:1 proportion of mean and variance contributions is clear in view of the 1/2

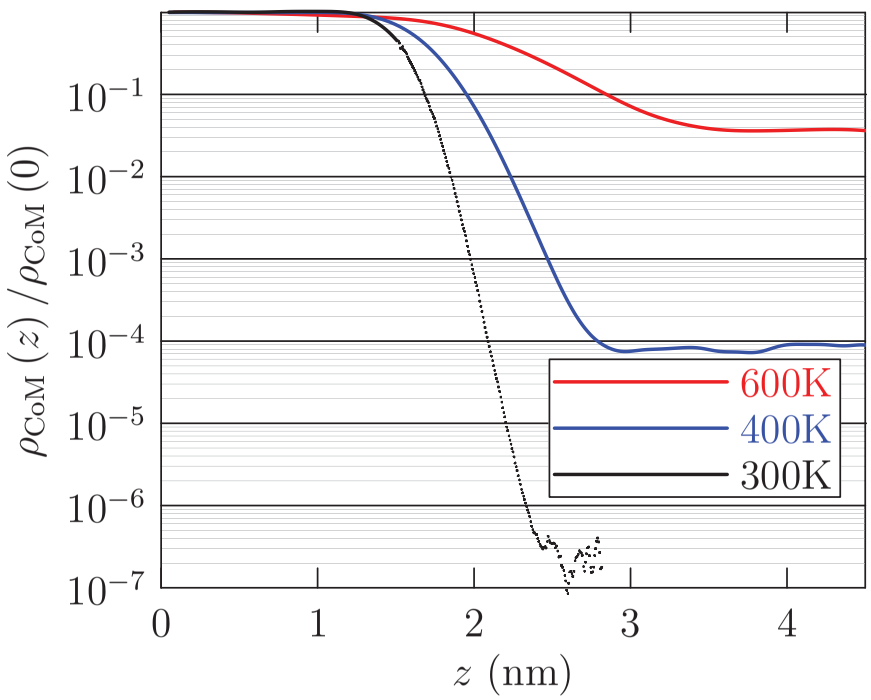

Figure 3.13: The dotted results were obtained by the WHAM method in order to estimate of the vapor density for the T=300K case where that value is not satisfactorily obtained from observation of the physical simulation.

in Eq. (3.4). At the highest temperature considered, the mean and variance contributions are roughly equal, so Gaussian models of solvation are not supported then. The accuracy of the inference of the packing contribution at T=600K is therefore less convincing also.

3.3 Conclusions

Propylene carbonate (PC) does not spread completely on graphite, but at ambient conditions it wets with a contact angle of 31°. Molecular dynamics simulations agree with this contact angle after 40% reduction of the strength of graphite-C atom Lennard-Jones interactions with the solvent, relative to the models used initially.[75,100] The simulation of a nano-scale PC droplet on graphite displays a pronounced layering tendency and an *Aztex pyramid* structure for the droplet. Extrap-

Table 3.2: Bulk calculations at $p = 1$ atm, $N = 600$. Energies are in kcal/mol. $\kappa_T = \beta \left\langle \delta V^2 \right\rangle / \langle V \rangle$. Experimental values[126,127] for κ_T at $T = 25$C are in the range 0.5-0.6 GPa^{-1}. Where not indicated explicitly, estimated statistical uncertainties are less than one (1) in the least significant digit given. The thermal expansion coefficient implied by these results is 0.94×10^{-3}/K (experimental value:[128] 0.845×10^{-3}/K).

T(K)	ρ (nm^{-3})	$\langle\varepsilon\rangle$	$\langle\varepsilon\rangle + \frac{\beta}{2}\langle\delta\varepsilon^2\rangle$	κ_T (GPa^{-1})	ϵ/ϵ_0
270	7.5	-33.2	-24.4	0.3	82.9 ± 2.9
300	7.3	-32.0	-24.3	0.3	63.4 ± 2.2
320	7.2	-31.2	-23.6	0.4	59.1 ± 2.3
400	6.7	-28.4	-21.1	0.5	41.8 ± 1.7
600	5.5	-22.0	-15.3	1.9	19.7 ± 1.3

olation of the computed tensions of PC liquid-vapor interface estimates the critical temperature of PC accurately to about 3%. PC molecules lie flat on the PC liquid-vapor surface, and tend to project the propyl carbon toward the vapor phase. Close PC neighbors stack carbonate planes with the outer (O1) oxygen of one molecule snuggled into the positively charged propyl end of another molecule so that neighboring molecule dipole moments are approximately antiparallel. The calculated thermal expansion coefficient and the dielectric constants for liquid PC agree well with experiment. The distribution of PC molecule binding energies is closely Gaussian. Evaluation of the density of the coexisting vapor then permits estimation of the excluded volume contribution to the PC chemical potential, and that contribution is about 2/3rds of the magnitude of the contributions due to attractive interactions, with opposite sign.

3.4 Methods

The GROMACS package[129] was used in all simulations. All the simulations were performed under periodic boundary conditions, electrostatic interactions calculated by the particle mesh Ewald method with a grid spacing of 0.1 nm. Partial charges of PC are those of Ref. 3. cutoff at 0.9 nm, and the temperature was main-

tained by the Nose-Hoover thermostat.

For bulk PC systems, constant NPT conditions were adopted, treating 600 PC molecules initially positioned uniformly in a $(4.4\ \mathrm{nm})^3$ cubic cell utilizing Packmol.[130] The initial configuration was energy-minimized, then simulations were carried out at $T = 270$ K, ... 600 K with p=1 atm, with 1 fs integration time step, and were extended to 50 ns with first 10 ns discarded as aging.

Interfacial characteristics of liquid PC were investigated by molecular dynamics of two-phase (liquid-vapor) systems in slab geometry (FIG. 3.5). 600 PC molecules were positioned in a $5.3 \times 5.3 \times 10.3\ \mathrm{nm}^3$ cell, T=300, 400, and 600K. After minimization, these systems were aged for 10 ns before a 10 ns production equilibrium trajectory at 300 K. At 400 K and 600 K, 40 ns equilibrium trajectories were obtained. The interfacial tensions were assessed (FIG. 3.6) by differencing interfacial stresses in the standard way, averaging through the production trajectories.

Configurations were sampled from each trajectory at every 0.005 ns for further analysis. The electrostatic contributions to the binding energies (TABLE 3.2) were evaluated with the GROMACS reaction field method. Those electrostatic contributions were checked against standard Ewald evaluations of electrostatic energies, and the differences were typically about 0.1 kcal/mol. The differences of generalized reaction field alternatives from the other methods were substantially larger, *i.e.* 1-2 kcal/mol.

Experimental applications almost always involve a racemic mixture of PC. The calculations here were for the pure liquid of the enantiomer FIG. 3.1. This was because extensive initial calculations made that choice,[75,100] and no results here are expected to be sensitive to that distinction. Explicit checking of a few cases in TABLE 3.1 and TABLE 3.2 confirm that no results are changed significantly for the racemic mixture. Nevertheless, we expect subsequent results to treat the racemic

case.

3.4.1 PC/graphite simulations

The PC/graphite simulations used 600 PC molecules and three layers of graphite. Each layer has 9122 atoms, including 266 capping hydrogen atoms at the edges, to make a square surface of about 15.5 nm by 15.5 nm. A liquid phase configuration of the PC molecules was placed near the graphite surface and equilibrated for 5 ns. All simulations used constant TVN conditions, at T=300 K and a cubic (15.5 nm)^3 volume. To test how the PC/graphite interactions influence interfacial properties, a series of simulations with different Lennard-Jones $\varepsilon_{\mathrm{LJ}}$ values for the PC-graphite interactions were obtained, by scaling $\varepsilon_{\mathrm{LJ}}$ by factors (0.25, 0.4, 0.5, 0.55, 0.6, 0.75 and 1). Interactions between all PC atoms and the graphite carbon atoms were all scaled. Each system was simulated for 5 ns. For the optimal $\varepsilon_{\mathrm{LJ}}$ scaling, simulations were carried out for 10 ns. Simulations were carried out with and without constraints on the graphite surface utilizing a harmonic restraint with force constant of 1000 kJ/(mol nm^2). The simulations uses a cut-off value for equal to 0.9 nm. Additional simulations were carried-out with a cut-off value of 1.2 nm. The PC/graphite contact angle was found to insensitive to the cut-off value or the use of restraints on the surface. The indicated 40% reduction in the strength of graphite-C Lennard-Jones interactions may be the simplest adjustment that brings the simulation results into consistency with the contact angle observation.

3.4.2 Droplet silhouette

The droplet silhouette (FIG. 3.3) was obtained in the following way:[110] On the basis of the simulation data, the mass density was binned. A two dimensional grid was used in cylindrical coordinates with z perpendicular to the graphite plane and r the radial coordinate. The z axis contained the centroid of the droplet. The

function

$$\rho(r,z) = \frac{\rho_{\text{liq}}}{2}\left\{1 - \tanh\left[\frac{r - r_0(z)}{d(z)}\right]\right\} , \tag{3.10}$$

which acknowledges that the $\rho_{\text{vap}} \approx 0$, was fit to the binned mass density. Thus the width of the interfacial profile, $d(z)$, and the position of the interface, $r_0(z)$ were obtained for each z layer. Since the density exhibits distinct layering parallel to z (FIG. 3.4), this procedure is particularly effective where analysis of the density in constant-z slices is natural, for $0 < z < 1.9$ nm.

For $z > 1.9$ nm, where the $0 < r < 2$ nm portion of the fluid interface is roughly parallel to the z=constant (graphite) surface, constant-r slices of the density were similarly fit to the function

$$\rho(r,z) = \frac{\rho_{\text{liq}}}{2}\left\{1 - \tanh\left[\frac{z - z_0(r)}{d(r)}\right]\right\} . \tag{3.11}$$

In view of FIG. 3.4, this describes the outer (largest r) behavior, where the density is decreasing through $\rho_{\text{liq}}/2$. The two approaches give the same values near a crossing point $r \approx 2$ nm. Combing these two fits gives FIG. 3.3.

3.4.3 Windowed sampling for calculations of coexisting vapor densities

The coexisting vapor densities were evaluated by stratification on the basis of the Weighted Histogram Analysis Method (WHAM)[131,132] to concentrate sampling on the low densities of the vapor phase. Windowed calculations were performed with 600 PC molecules at temperatures 300K and 400K adopting the methods described above. Initial configuration for each window was obtained by pulling a PC molecule from the center of mass of the slab to deep into vapor phase at constant rate of 0.01 nm/ps. In the 300K case, 15 windows, spaced by 0.1 nm in bulk liquid phase

and 0.05 nm near interface and vapor phase, were treated. Trajectories of 5 ns/window (after 1 ns of minimization and 5 ns of aging) were used to reconstruct density profiles. For the 400K calculation, 41 windows of 0.1 nm uniform spacing were used.

The harmonic potential energy $U = k(z - z_0)^2$ windowing function was employed, with z is the instantaneous distance of the center of mass of the pulled PC molecule from center of mass of the slab and z_0, the designated minimum of U, identifying the window position. $k = 4000$ kJ/mol/nm^2 (for 300K) and k=6000 kJ/mol/nm^2 (for 400 K).

3.4.4 Liquid PC dielectric constant

The dielectric constant of uniform PC liquid is evaluated following standard simulation methods.[75,115] The calculation treated 600 PC molecules under periodic boundary conditions. Resulting values were averaged from the 40 ns production trajectories at constant pressure of 1 atm.

Chapter 4

Direct Dynamical Simulation of Filling of Carbon Nanotube Forest Electrochemical Double-layer Capacitors

4.1 Introduction

Compared to batteries, capacitors provide high charge/discharge rates, temperature insensitivity, and long life-times. Batteries have high energy densities, but capacitors have higher power densities. Research on capacitor materials emphasizes improving energy densities while retaining good power densities of capacitors. Forests can have high specific capacitance and offer the possibility of nano-scale design. The feasibility of fully molecular simulation of electrochemical double-layer capacitors based on CNT forests has recently been demonstrated. (Fig. 4.1)

In previous chapter, we studied propylene carbonate as a solvent for EDLCs, reported experimental and molecular simulation results on PC interfaces. PC wets graphite with a contact angle of 31° at ambient conditions. Molecular dynamics simu-

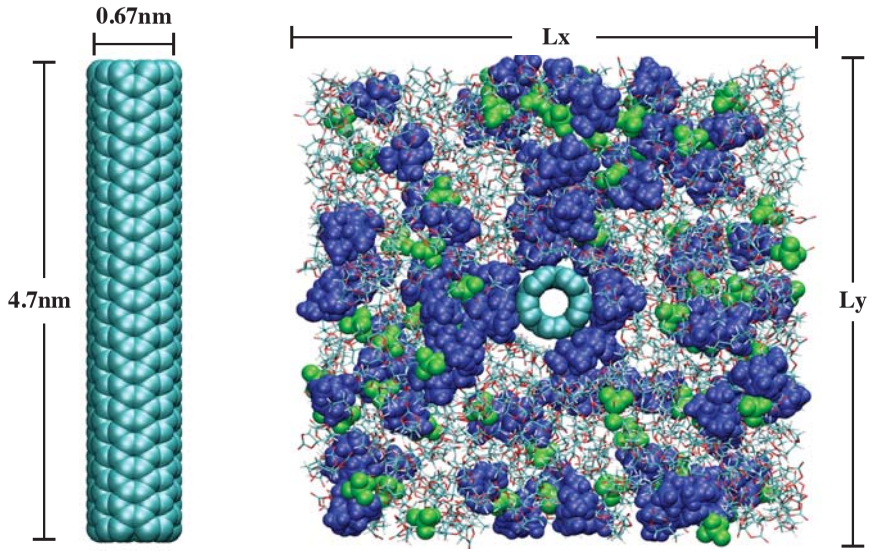

Figure 4.1: Illustration of the filled nanotube forest treated by simulation with periodic boundary conditions. (Left) The nanotube model. (Right) Cross-section perpendicular to the nanotubes.[100]

lations agree with this contact angle after 40% reduction of the strength of graphite-C atom Lennard-Jones interactions with the solvent. This validation paves the way to direct simulation of dynamical filling and performance of CNT-based EDLCs.

Here, we present all-atom molecular dynamics simulations of electrochemical double-layer capacitors based on CNT forests with PC: $TEABF_4$ solutions. We explicit characterizations of the charging and discharging processes, including electrolyte composition in the pores, the rates of charging responses, and the possibility of bubble formation. Also, we consider the kinetic properties associated to confinement.

4.2 Results and Discussion

4.2.1 Primitive simulation

Primitive simulation with 8 nanotubes, 43 pairs of $TEABF_4$ ions and 414 PC molecules was carried out to investigate the system-size dependence of simulation results. (Peixi Zhu) Bubble formation was observed in the separating solution (Fig. 4.2),

which is a common concern in the charging process of chemical capacitors and batteries. Also, at highest charge level, the difference in ionic charge above and below the mid-plane of simulation box was not matching with the charge difference between the upper and lower nanotubes. Both observations were related to the system size.

Based on this primitive simulation, we scaled-up the reservoir region of our system by including 1000 PC and 85 pairs of ions (Fig. 4.3). Under applied charges, the entrance of ions into the interstitial pores occurs. That is, negative ions (BF_4^-) will experience an attraction from the positively charged lower nanotubes and move into the lower layer, whereas positive ions (TEA^+) will go into the upper layer. The transport results in a de-mixed state of solution. For each charge level, the ionic charge difference matched the charge difference between nanotubes. The rate of charging responses relates to the power density of EDLC. In our simulation, sub-nanosecond equilibration was observed during both charging and discharging processes.

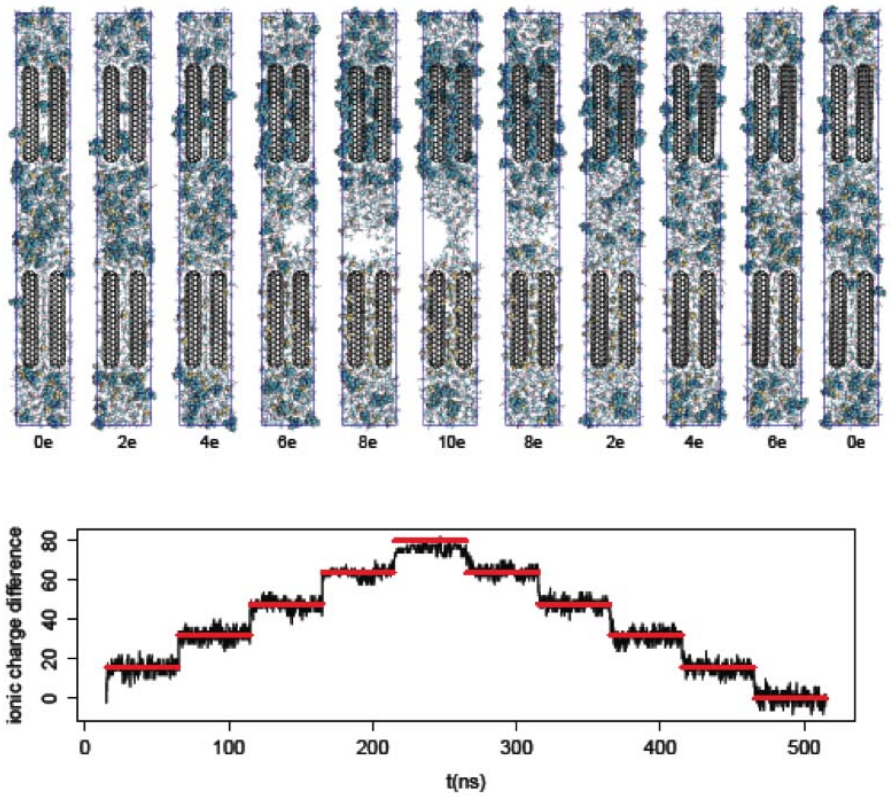

Figure 4.2: Upper panel: snapshots, separated by 50 ns, of the molecular dynamical filling of CNT forests as the electronic charge on the nanotubes is incremented. The label below each frame is the electronic charge/CNT. Upper layer has negatively charged CNTs, and the lower layer has positively charged CNTs. Here there are four CNTs above and below, for a total of eight (8) tubes altogether. The solvent is propylene carbonate, and the electrolyte is tetraethylammonium tetrafluorate. $T = 300$K (established by a Nose-Hoover thermostat). Notice the demixing and formation of a bubble in the separating solution, as the forest becomes strongly charged in this constant volume calculation. Notice also the low occupancy of the pores by the ions at the lowest levels of charging. Lower panel: Difference in ionic charge (black) above and below the mid-plane of the upper panel. Notice the sub-nanosecond equilibration of the charge balance, in both filling and emptying.

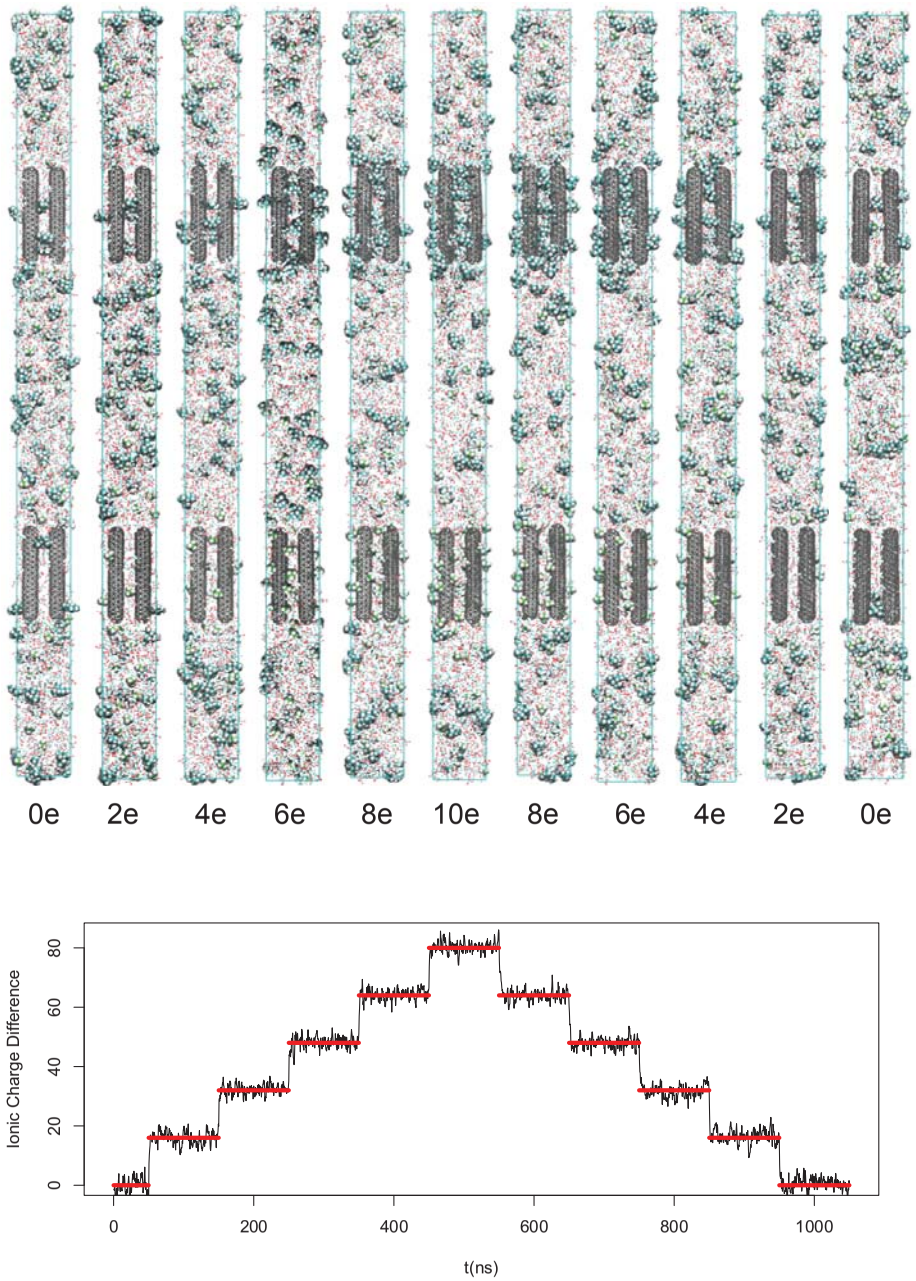

Figure 4.3: Upper panel: snapshots, separated by 100 ns, of the molecular dynamical filling of CNT forests as the electronic charge on the nanotubes is incremented. Pore radius = 0.5nm, T = 300K, p =1 atm. Lower panel: Difference in ionic charge (black) above and below the mid-plane of the upper panel. Notice the sub-nanosecond equilibration of the charge balance, in both filling and emptying.

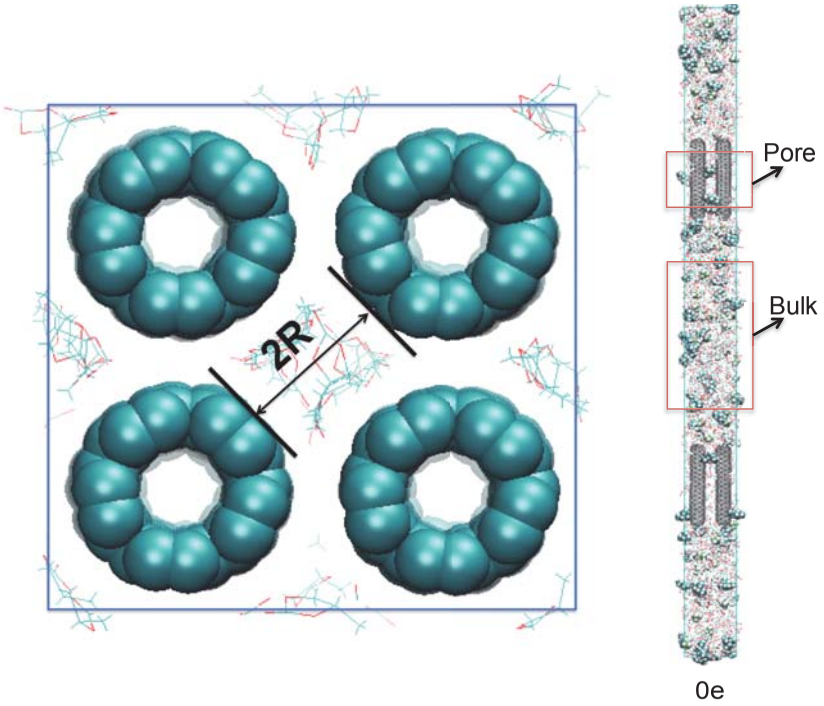

Figure 4.4: CNT pore geometry (left). Bulk solution reservoir and interstitial spaces of the CNT forest (right).

4.2.2 Calculations and data to be analyzed

Table 4.1: Calculations and data to be analyzed. The following simulations of filling CNT forest with $TEABF_4$/PC were carried out by GROMACS packages in an isothermal-isobaric ensemble (NPT) with periodical boundaries at $T = 300$K, $p = 1$ atm. The 300-atom carbon nanotubes are capped with half of a buckyball, C_{360} in total. The pore radius ranged from 0.4nm to 1.5nm. All the calculations simulated a complete charging and discharging cycle (charged up to 10e/CNT), except for the r_{pore}=0.4nm simulation (successfully charged up to 6e/CNT, only the charging process is performed). For each charge level, 50ns production run was performed after a 50ns-aging period.

r_{pore} (nm)	n_{PC}	$n_{\mathrm{TEABF_4}}$	n_{CNT}	L_{x},$L_{\mathrm{y}}(nm)$	L_{z} (nm)
0.4	1000	85	8	2.1	42.4
0.45	1000	85	8	2.2	37.9
0.5	1000	85	8	2.4	34.2
1.0	2000	170	8	3.8	26.3
1.5	1000	85	2	2.6	25.5

4.2.3 The role of attractive interactions in the motions of molecules in liquids

With the database constructed during above simulations, we focus on the kinetic characteristics. Our initial step, in this section, is to distinguish differing roles of repulsive and attractive interaction in the motions of molecules in equilibrium liquids. A basic goal of the molecular theory of liquids is the clear discrimination of effects of intermolecular interactions of distinct types, *e.g.* excluded volume interactions and longer ranged attractive interactions[133,134]. That discrimination leads to the van der Waals picture of liquids[133,135,136] in the equilibrium theory of classical fluids. Those ideas are clear enough to be captured in models with van der Waals *limits* that are susceptible to rigorous mathematical analysis[137]. Ultimately, the general theory of liquids is then founded on the composite van der Waals picture which also serves to characterize non-van der Waals cases, such as water, for particular scrutiny[121]. Here we obtain observations that distinguish differing roles of repulsive and attractive interaction in the dynamics of molecules in equilibrium liquids.

The analogue of the van der Waals picture of equilbrium liquids for transport properties is much less developed. That is partly because of the higher variety of transport phenomena to be addressed[138]. It is also because the mathematical van der Waals limit contributes essentially at *zeroth* order to the thermodynamics, whereas extensions of van der Waals concepts to transport parameters have shown that the leading contribution typically comes at higher order[139]. The leading contribution from attractive interactions to a self-diffusion coefficient vanishes in the van der Waals limit[140] though the equation of state changes qualitatively in the same limit.

Nevertheless, it is important accurately to characterize the contributions of realistic attractive interactions to kinetic characteristics of liquids. This has been the serious topic of previous investigations[141,142]. One distinction of the work here from

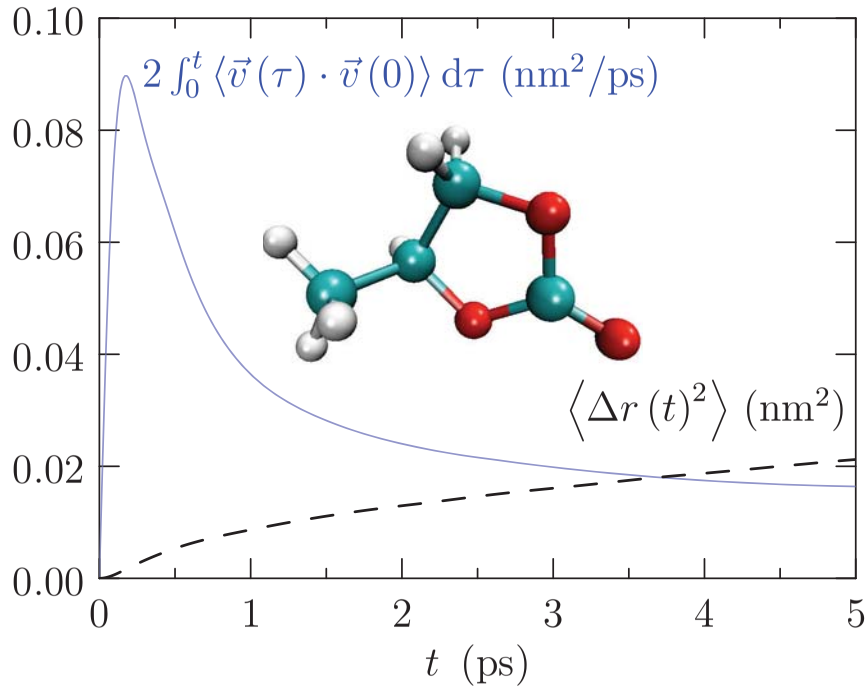

Figure 4.5: Dashed curve: the mean-square-displacement of the center-of-mass of a propylene carbonate molecule in liquid PC. $D_{\mathrm{PC}} = 4.0 \times 10^{-6}$ cm^2/s. Solid curve: time-derivative of the mean-square-displacement. The inset depicts the propylene carbonate (PC) molecule. The molecular dynamics simulation utilized the GROMACS package in the isothermal-isobaric ensemble (NPT) with periodic boundary conditions and p = 1 atm. The GROMACS OPLS all-atom force field was adopted for liquid PC, and temperature T = 300K maintained by Nose-Hoover thermostat. The system of n = 1000 PC molecules was aged for 10 ns, then a 1 ns trajectory was obtained, saving configurations every 10th 1 fs time step for analysis.

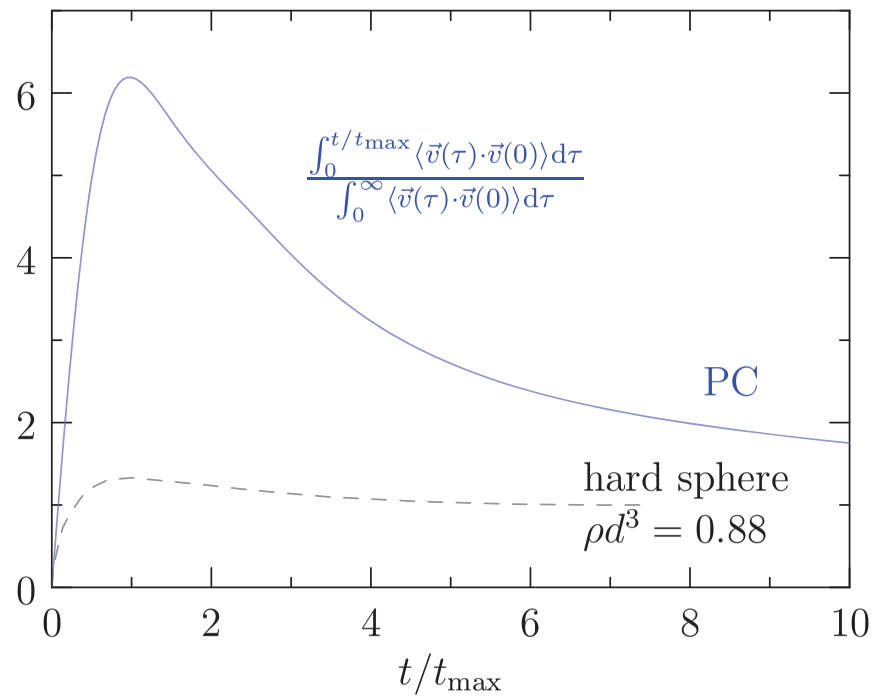

Figure 4.6: Normalized time-derivative of the mean-square displacement of a molecule center-of-mass. The blue curve is redrawn from FIG. 4.5, with the vertical scaling so that the graph equals one (1) at large time, and the horizontal scaling so that the graph has a maximum at the time $t_{\max}$. The dashed curve is the result for the hard sphere fluid, redrawn from Alder, *et al.*[143] The density, $\rho d^3 = 0.88$, is within about 5% of the hard-sphere freezing point. The maximum in these graphs occurs when $C(t)$ changes sign. The result for the realistic PC fluid is qualitatively different from the result for the hard sphere case.

previous efforts is that we focus on a specific autocorrelation function of the random forces on a molecule in the liquid, $\gamma(t)$ defined below. Another distinction is that we consider practical examples of solvent liquids that are strongly bound compared to the Lennard-Jones (LJ) models that have been the focus of historical work. We characterize this 'strongly bound' distinction by the ratio of the critical-point to the triple-point temperatures ($T_{\mathrm{c}}/T_{\mathrm{t}}$). For the LJ fluid this ratio is $T_{\mathrm{c}}/T_{\mathrm{t}} = 1.9$, but here we consider propylene carbonate (PC: 3.5), ethylene carbonate (EC: 2.3), acetonitrile (AN: 2.4), and water (W: 2.4). In these practical cases, attractive interactions leading to the greater binding strength are more prominent than in the historical LJ work.

Primitive results that motivate our observations are shown in FIGs. 4.5 and 4.6. The mean-square-displacement $\langle \Delta r(t)^2 \rangle$ of the center-of-mass of a PC molecule in liquid PC (FIG. 4.5) achieves growth that is linear-in-time only after tens of collision-times. The time-derivative of $\langle \Delta r(t)^2 \rangle$ displays a prominent maximum that can be taken as a rough marker for a collision time. After that, the derivative decreases by more than a factor of ten, reflecting the integrated strength of a negative tail of the velocity autocorrelation function,

$$C(t) = \langle \boldsymbol{v}(t) \cdot \boldsymbol{v}(0) \rangle / \left\langle v^2 \right\rangle \ . \tag{4.1}$$

That negative tail is qualitatively different from the case of the hard-sphere fluid at high densities (FIG. 4.6)[143]. More recent studies of atomic fluids with purely repulsive inter-atomic forces show that negative tails in the velocity autocorrelation functions are slight[144,145]. The result for the realistic PC fluid is qualitatively different from the atomic repulsive force case.

We focus on the friction kernel (memory function), $\gamma(t)$ defined by

$$M \frac{\mathrm{d}C(t)}{\mathrm{d}t} = -\int_0^t \gamma(t-\tau)\, C(\tau)\, \mathrm{d}\tau \ , \tag{4.2}$$

where M is the mass of the molecule. $\gamma(t)$ can be considered the autocorrelation function for the *random* forces on the molecule[146]. The textbook method for extracting $\gamma(t)$ utilizes standard Laplace transforms. But inverting the Laplace transform is non-trivial and we have found the well-known Stehfest algorithm[147] to be problematic. Berne and Harp[148] developed a finite-difference-in-time procedure for extracting $\gamma(t)$ from Eq. (4.2). That procedure is generally satisfactory but sensitive to time resolution in the numerical $C(t)$ that is used as input here. Another alternative follows the Laplace transform idea expressed as Fourier integrals, utilizing

specifically the transforms

$$\hat{C}'(\omega) = \int_0^\infty C(t)\cos(\omega t)\,\mathrm{d}t \ , \tag{4.3a}$$

$$\hat{C}''(\omega) = \int_0^\infty C(t)\sin(\omega t)\,\mathrm{d}t \ . \tag{4.3b}$$

Then

$$\hat{\gamma}'(\omega) = \frac{M\hat{C}'(\omega)}{\hat{C}'(\omega)^2 + \hat{C}''(\omega)^2} \ , \tag{4.4}$$

with

$$\hat{\gamma}'(\omega) \ = \int_0^\infty \gamma(t)\cos(\omega t)\,\mathrm{d}t \ . \tag{4.5}$$

Taking $\gamma(t)$ to be even time, the cosine transform is straightforwardly inverted. The Einstein frequency $\Omega^2 = \langle F^2 \rangle / 3Mk_\mathrm{B}T$, with $F = |\boldsymbol{F}|$ the force on the molecule, provides the natural normalization $\gamma(0) = M\Omega^2$.

More details for memory kernel and above two numerical methods are provided in Appendix E.

The two numerical methods for extracting $\gamma(r)$ from $C(t)$ agree well (FIG. 4.7). $\gamma(t)/M\Omega^2$ for four strongly bound liquids are qualitatively similar to each other and show two distinct relaxation behaviors. The historical LJ results[141,142] are consistent with this, though the two relaxation behaviors are distinct for the LJ fluid only at the lowest liquid temperatures[142]. We suggest that the slowest-time relaxation derives from molecularly long-ranged interactions, while the fastest-time relaxation is associated with collisional events and short-ranged interactions. Indeed exponential relaxation of $C(t)$ — reasonable for $t > 0$ for the atomic purely repulsive-force case — is associated with practical δ-function models of $\gamma(t)$. This discrimination of long-

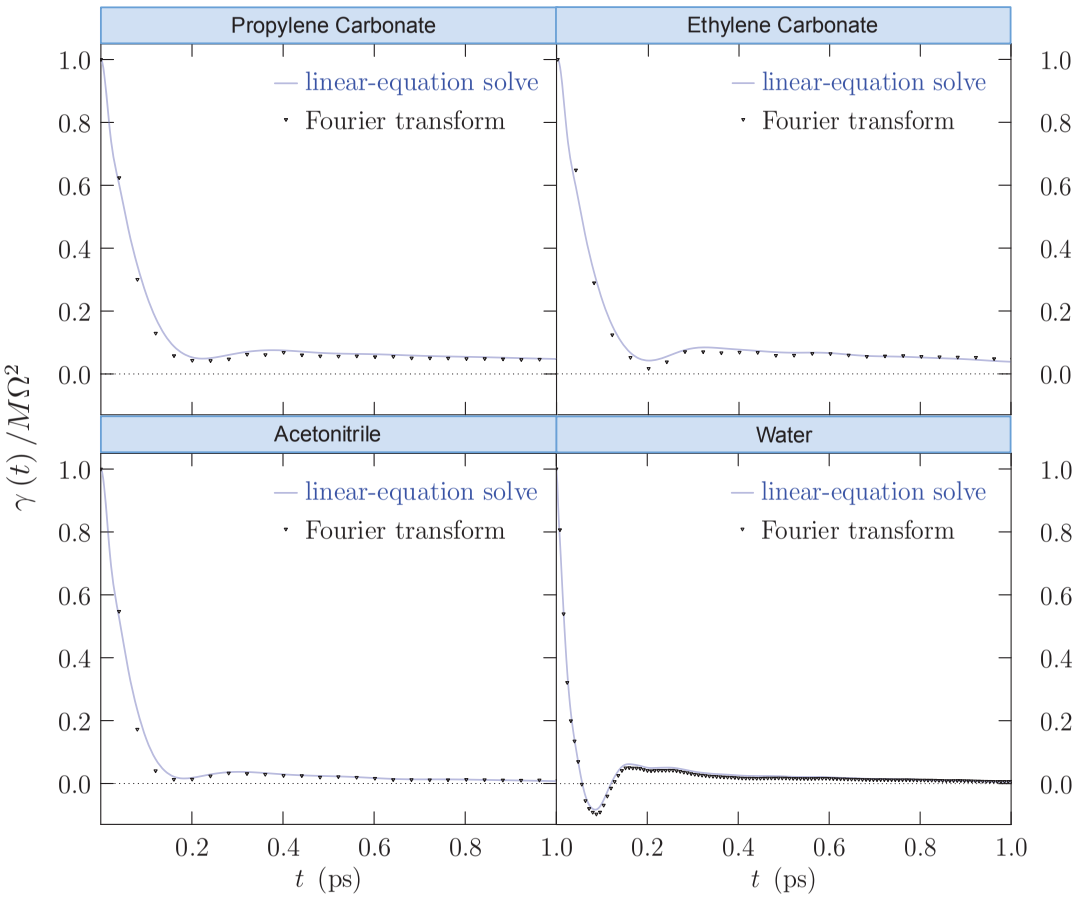

Figure 4.7: $\gamma(t)$ the friction kernel (memory function, or autocorrelation of random forces) All the simulations were carried out with the GROMACS package in the isothermal-isobaric ensemble (NPT) with periodic boundary conditions and $p = 1$ atm. PC calculations were specified in FIG. 4.5. For the acetonitrile simulation the force-field of Nikitin and Lyubartsev [149] was assumed. For ethylene carbonate we used the GAFF force field [98], a system size of 215 molecules at $T = 313$ K. For the water simulation, the TIP4P-EW model [150] was used, and the trajectory was saved every 1 fs.

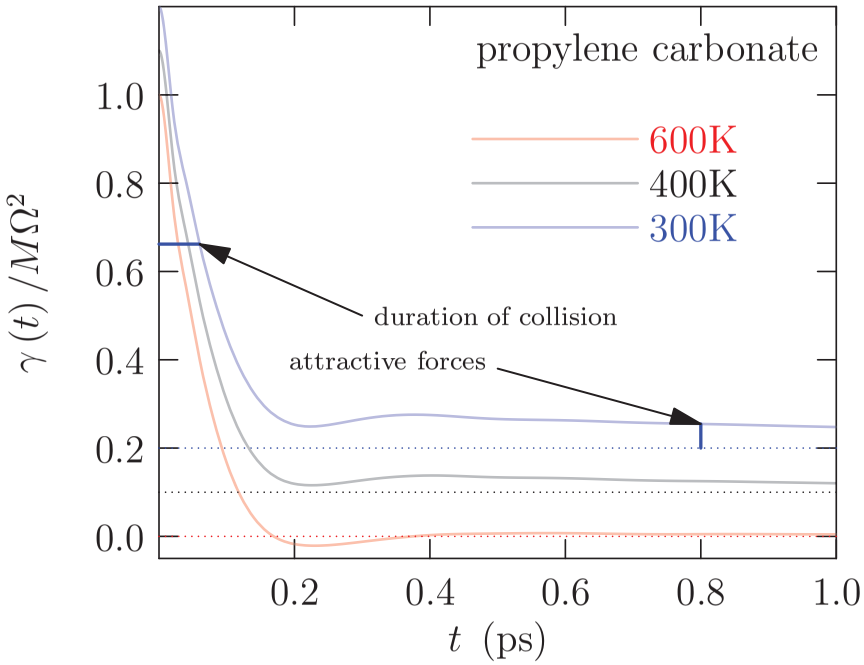

Figure 4.8: Autocorrelation function for the random forces on the center-of-mass of a propylene carbonate molecule as a function of temperature at constant pressure, $p = 1$ atm. The longer time-scale relaxation becomes less prominent at higher T.

ranged and short-ranged interaction effects was expressed by Wolynes[151] long-ago in the context of ion mobilities in solution. Here the mobilities of non-ionic species are considered, though similar behavior has been identified in just the same way for organic ions in solution[152].

The results for liquid PC at several higher temperatures (FIG. 4.8) show that the amplitude of this longer-time-scale decay decreases with increasing T, as expected.

By comparison, Dang and Annapureddy[153,154] evaluated $\gamma(t)$ for Dang-Chang-model water[155] in a different setting, and they obtained the distinct bi-relaxation behavior observed here. In that alternative setting, the separation between a water oxygen atom and a near-neighbor ion was constrained at a barrier value and $t > 0$ negative values of $\gamma(t)$ (FIG. 4.7) were not observed[153,154].

The longer-time scale decay of $\gamma(t)$ (FIG. 4.7) is less prominent for the liquid water case than for the other cases. We investigated this further by eliminat-

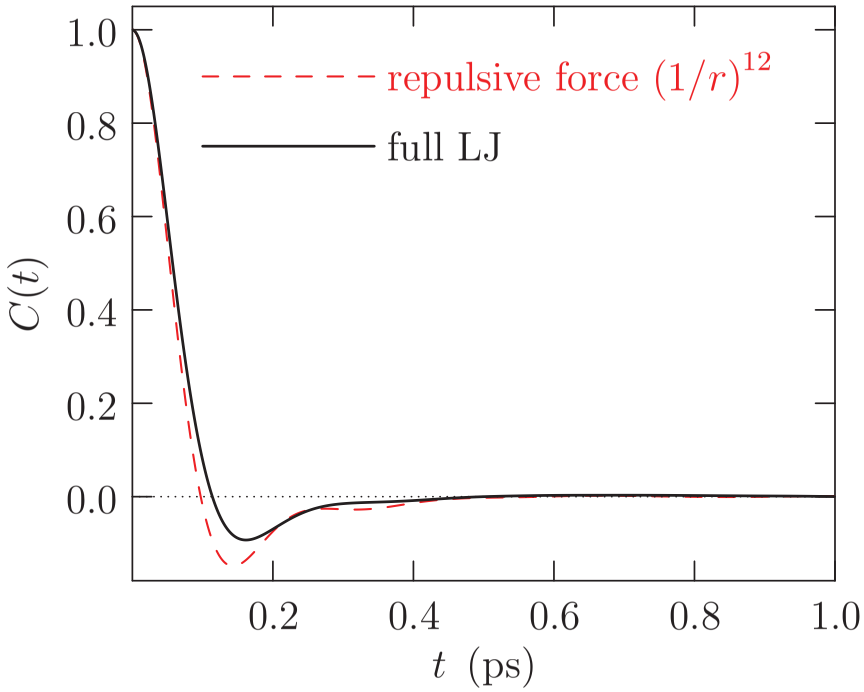

Figure 4.9: Velocity autocorrelation function for the LJ 6-12 fluid and the corresponding result when the $1/r^6$ contribution to the pair potential energy is dropped. The LJ thermodynamic state point is $\rho\sigma^3 = 1.06$, and the super-critical $k_\mathrm{B}T/\epsilon = 3.66 \approx 2.8T_\mathrm{c}$ [156]. For the $1/r^{12}$ case, this density is slightly higher than the high density cases studied by Heyes *et al.* [145], (effective packing fraction $\xi_\mathrm{HS} \approx 0.466$ compared to 0.45).

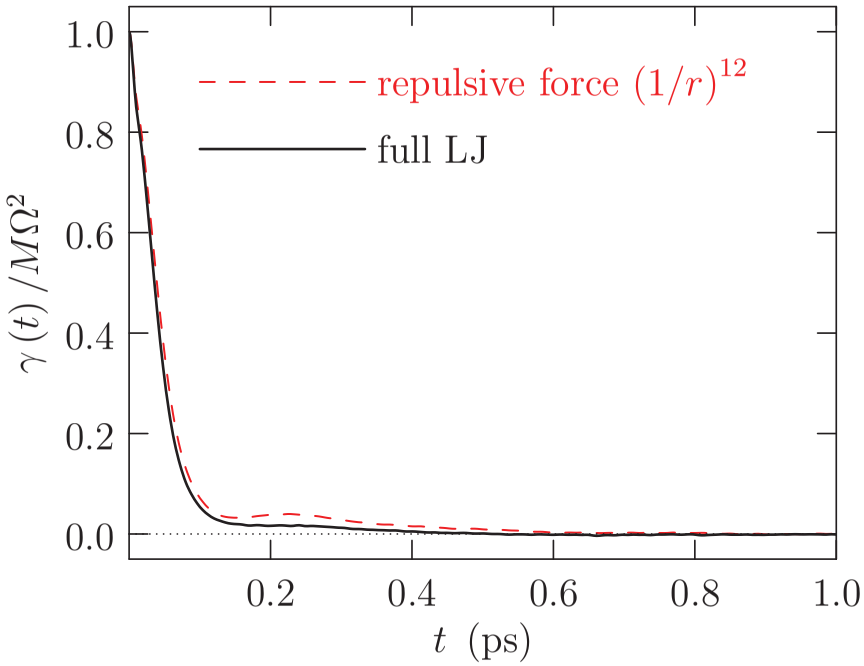

Figure 4.10: For the LJ system of FIG. 4.9. The second, longer-time-scale relaxation is not evident at this thermodynamic state which high density, super-critical for the LJ liquid. Thus, the longer-time-scale relaxation of Fig. 4.7 for water, is due to the electrostatic interactions that contribute largely to the cohesive binding of liquid water.

ing the partial charges associated with the pair-molecule interactions, leaving LJ 6-12 interactions (FIGs. 4.9 and 4.10). That underlying LJ case is strongly super-critical. Furthermore, with the implied high-density of the underlying LJ system, the continuous-repulsive-force ($1/r^{12}$) case in not similar to the result from the previous study of Heyes *et al.*[145]; we observe a distinct recoil feature at this density.

4.2.4 Transport properties associated with confinement

Based on the understanding the effects of attractive forces in the motion of molecules in liquids, we go back to our study of kinetic characteristics associated with the confinement and the anisotropic environment. Transport properties for PC molecule in above simulations are showed in Fig. 4.11, compared between bulk solution reservoir and the interstitial spaces of the CNT forest (Fig. 4.4). the mobilities of solvent were characterized on the basis of the observed mean-square-displacements (MSD):

$$\frac{\mathrm{d}\left\langle \Delta r(t)^2 \right\rangle}{\mathrm{d}t} = 2\int_0^t \left\langle \boldsymbol{v}\left(0\right) \cdot \boldsymbol{v}\left(t\right)\right\rangle \mathrm{d}\tau \ , \tag{4.6}$$

and velocity autocorrelation function (VACF), defined in Eq: 4.1.

The intermediate time differences — the negative peak in the velocity autocorrelation function — are probably consequences of long-range interactions with the two media, which are different over long distances scales. At much longer times, the VACF for the PC molecules in the pore displays a negative correlation tail. This may be due to the one-dimensional (single-file) character of the motions within the pore. The long-term diffusivity of a PC molecule in this channel is then substantially lower than in the bulk solution.

Compared to the bulk, PC molecule in the pore showed a larger mobility (Fig. 4.11, upper) and a slower time manner of velocity dropping during the collision (Fig. 4.11, lower). Both effects are due to the more organized orientation of PC molecules in the pore (Recall that the PC molecules are tend to lie flat on the interface layer, Fig. 3.7).

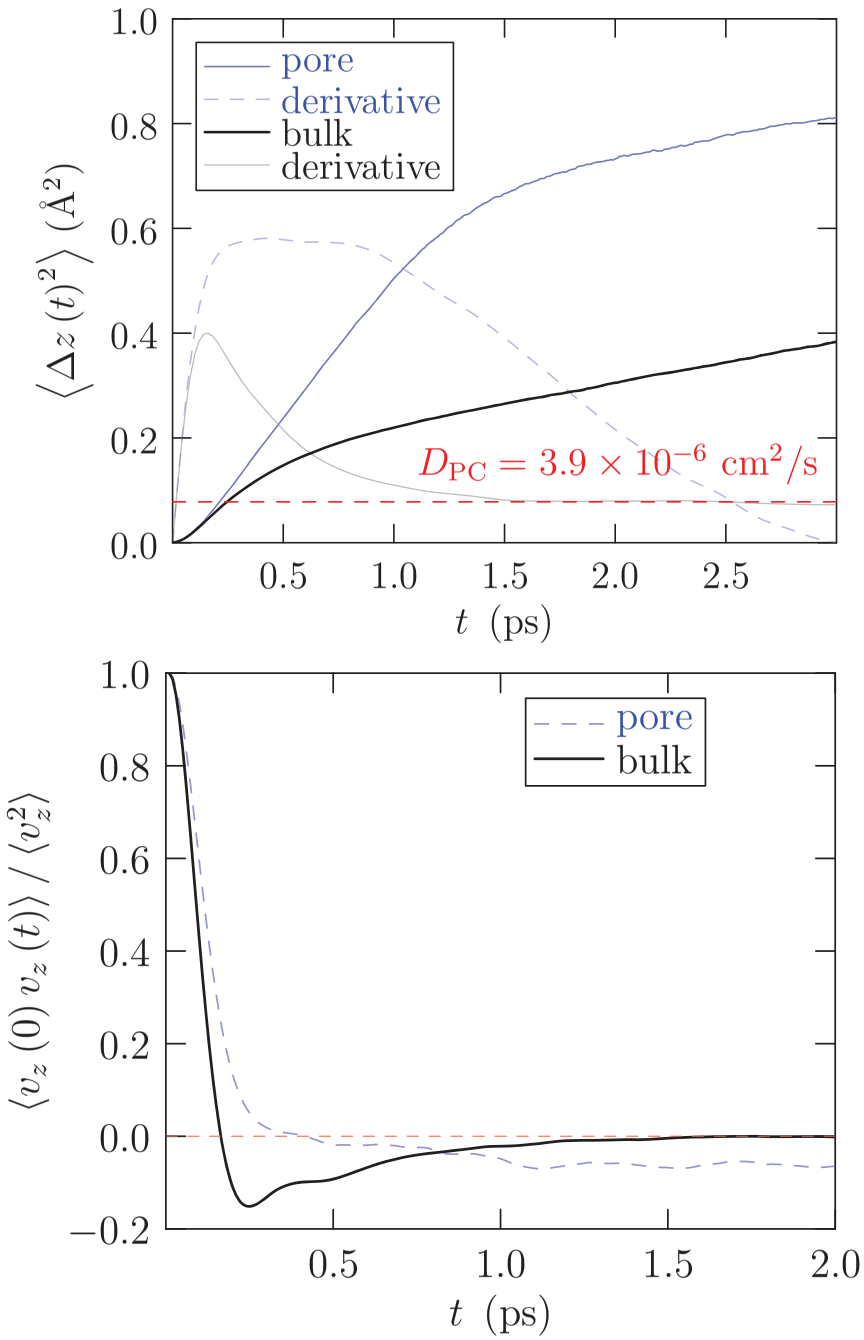

Figure 4.11: (upper) Mean-square z-displacement of a propylene carbonate (PC) molecule in the interstitial spaces of the CNT forest, compared to a PC molecule in the bulk solution reservoir. The fainter peaked curves in the background are derivative of MSD, which is nearly constant as $t \to \infty$. (lower) Comparison of the z-velocity autocorrelation function (VACF) for a PC molecule in the two cases, bulk vs pore (Geometry defined as Fig. 4.4). (T,p) = (300K,1atm) and the electrolyte concentration is about 1M. In this case, the CNTs are discharged (neutral) so that differences reflect just the confinement. The pores have a nominal diameter of 1nm.

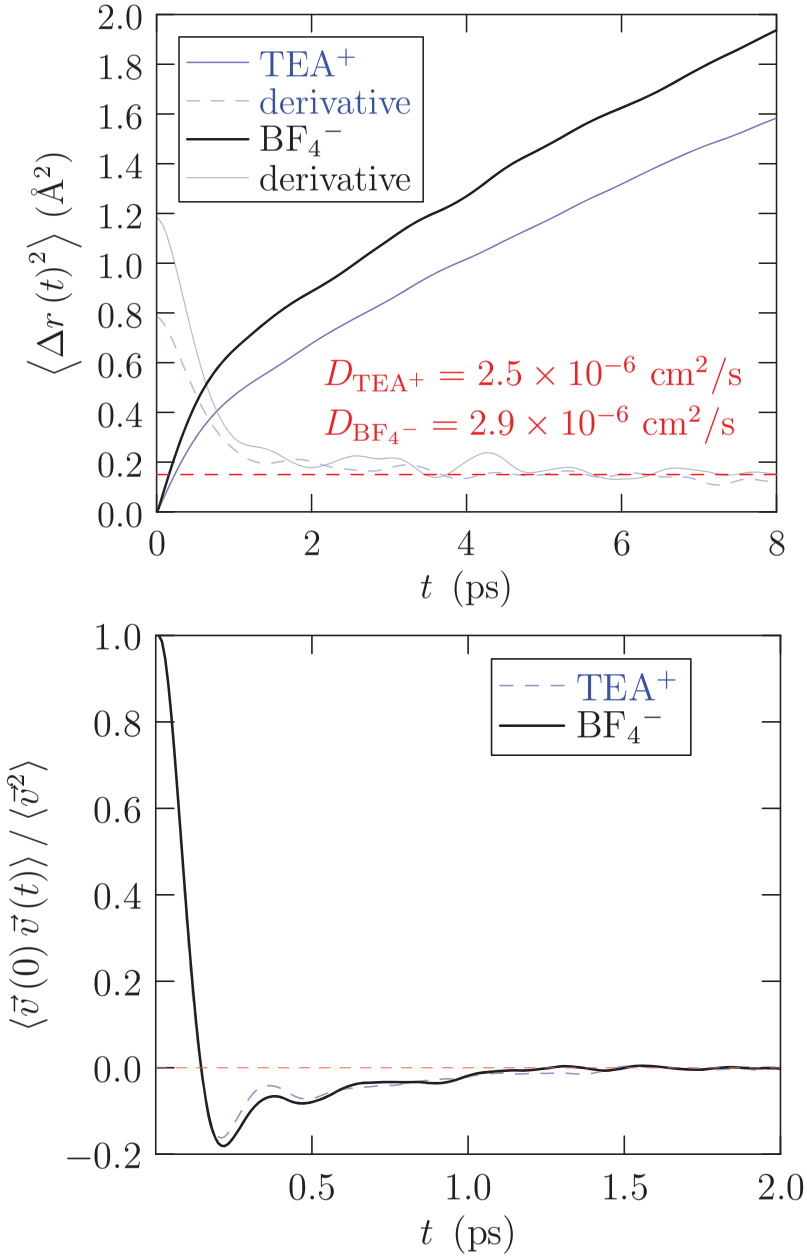

Figure 4.12: Upper panel: Mean-square-displacements of the center-of-mass of ions in PC. The thinner curves are the time-derivatives of the mean-square-displacements. Lower panel: Autocorrelation functions of the center-of-mass velocities of these ions. On this time interval these functions are qualitatively similar even though the molecular structures of these ions are qualitatively different.

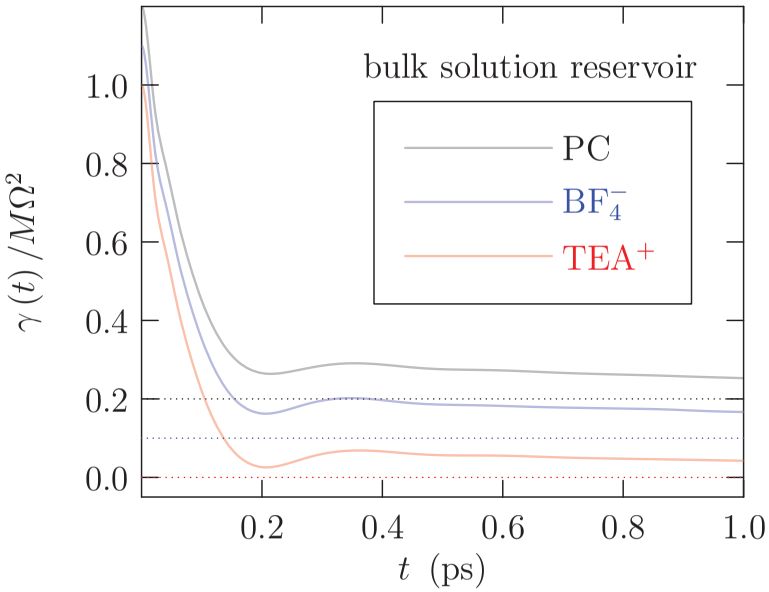

Figure 4.13: The autocorrelation function of the random forces on PC, BF_4^-, TEA^+ in the bulk solution reservoir. (Geometry defined as Fig. 4.4)

Kinetic properties for TEA^+ and BF_4^- ions (Fig. 4.12) in the bulk solution reservoir are investigated in the similar way.

Memory functions for BF_4^-, TEA^+ and PC in the bulk solution reservoir (Fig. 4.13) are achieved following Sec: 4.2.3. Ions behavior qualitatively similar to the solvent PC.

4.2.5 Dielectric relaxation

Dipole relaxation process in properties of propylene carbonate has been investigated in order to better understand its dynamical properties. Dielectric relaxation accesses the lag of the polarization of a material in responding to a change in an applied electric field. The molecular polarization in a dielectric medium does not respond to a changing electric field instantly. This delay is dependent on the frequency of a changing electric field. At low enough frequency, dielectric constant keep the same because the orientation of the dipoles can still keep up with the changing field. With the increase of frequency, the dipoles start to lag behind the field.[157]

The frequency dependent dielectric constant can be written as[157–159]

$$\epsilon(\omega) = \epsilon'(\omega) - i\epsilon''(\omega) \ . \tag{4.7}$$

The imaginary part $\epsilon''(\omega)$ is referred to dielectric loss, represents the loss of energy which is converted to heat. The relationship between $\epsilon(\omega)$ and the Fourier transform of the dipole moment autocorrelation function $P(t)$ is given by[159–161]

$$\frac{\epsilon'(\omega) - i\epsilon''(\omega)}{\epsilon_r - \epsilon_\infty} = 1 - i\omega \int_0^\infty P(t) \exp(-i\omega t) \mathrm{d}t \ , \tag{4.8}$$

with $\epsilon_r = \epsilon/\epsilon_0$ the static dielectric constant, $\epsilon_\infty = 1$ in the absence of electronic polarization in the system and

$$P(t) = \frac{\langle M(0)M(t)\rangle - \langle M(0)\rangle^2}{\langle M(0)^2\rangle - \langle M(0)\rangle^2} \ . \tag{4.9}$$

$M(t)$ is the dipole moment of the simulation system at time t.

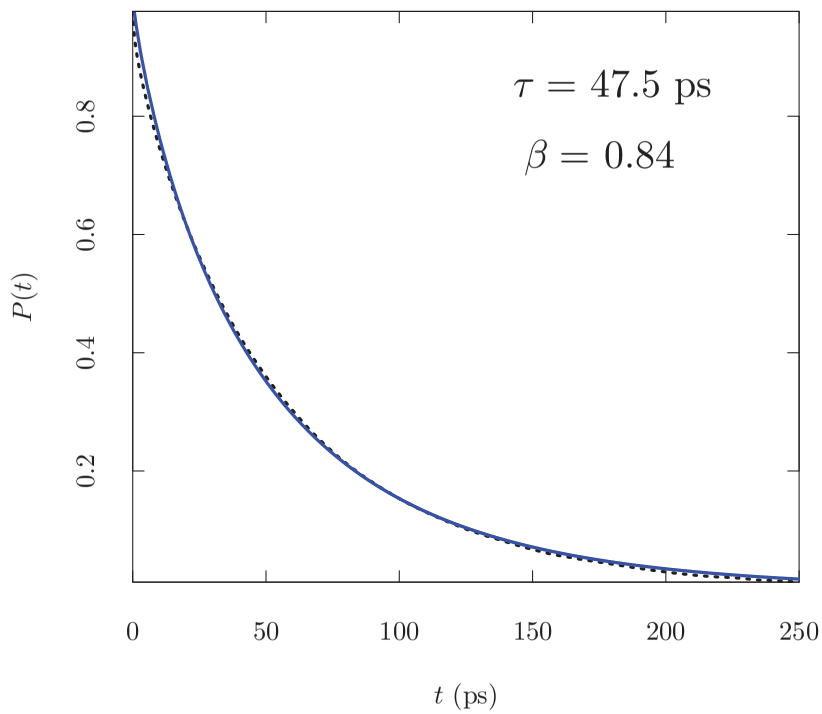

Figure 4.14: The dipole moment autocorrelation function $P(t)$ (dotted line) and fitted results to a Kohlrausch-Willliams-Watts model P_{KWW} (solid blue line) for liquid PC at $T = 300$ K and $p = 1$ atm. The relaxation time $\tau = 47.5$ ps, compared to the experimental result $\tau = 46$ ps [162].

The computed $P(t)$ was fitted to a Kohlrausch-Williams-Watts model

$$P_{\mathrm{KWW}}(t) = \exp[-(t/\tau)^{\beta}] \ . \tag{4.10}$$

The fitted results (Fig. 4.14) was used in Eq. 4.8 to obtain the real and imaginary part of frequency dependent dielectric constant (Fig. 4.15).[161]

Dielectric relaxation for liquid PC was also investigated at 280K, 320K, 250K, 400K and 600K (Table. 4.2). At elevated temperature, the molecular random thermo motion is greater, therefore, less perfect alignment with an applied field. This is

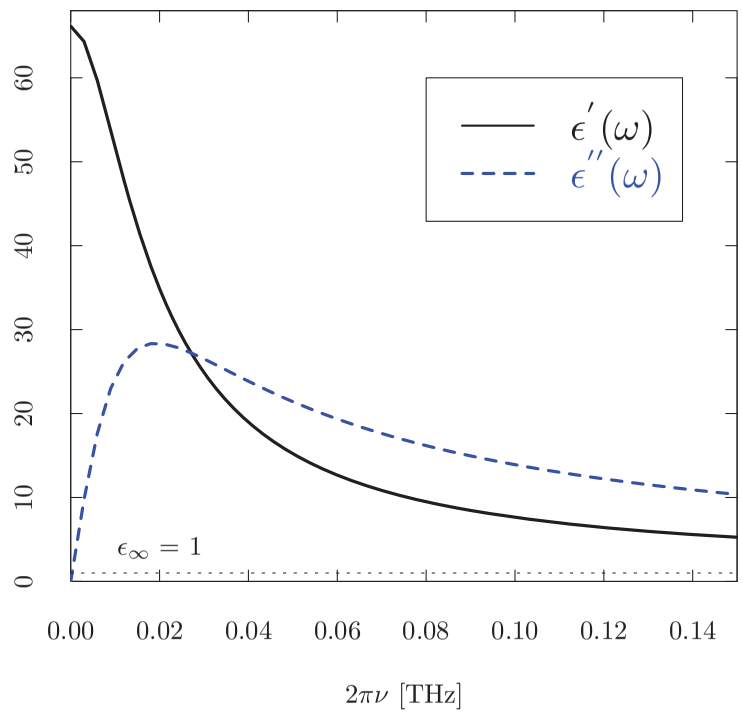

Figure 4.15: Dielectric constant and loss for liquid PC at $T = 300$ K and $p = 1$ atm. Static dielectric constant $\epsilon_0 = 63.4$ from bulk PC simulation.

Table 4.2: Dielectric properties of liquid PC in the temperature range of 280K to 600K.

T(K)	ϵ/ϵ_0	τ (ps)	β
280	78.4	78.9	0.84
300	66.1	47.5	0.84
320	63.2	30.1	0.89
350	55.8	19.2	0.86
400	42.2	10.7	0.88
600	19.2	2.7	0.92

reflected by a reduced static dielectric constant (Fig. 4.16).

The relaxation time is decreased as temperature increased, which implying the polarization relaxes faster towards a new equilibrium at higher temperature. As a result, the dielectric loss shows a lower and broader peak extending into the higher frequency range (Fig. 4.17).

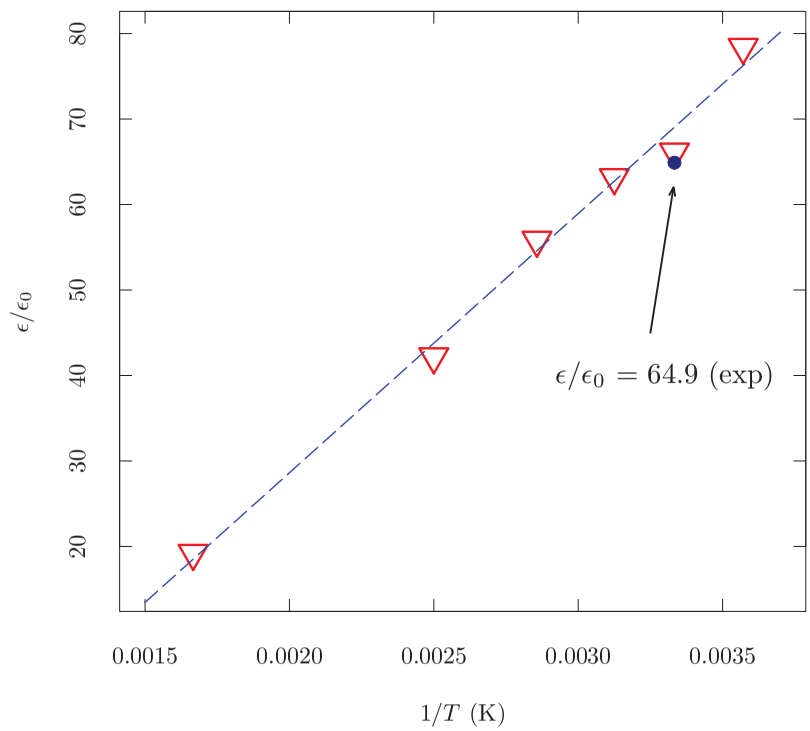

Figure 4.16: Dielectric constant of model propylene carbonate, evaluated following standard simulation methods.[75,115] The calculation treated 1000 PC molecules under periodic boundary conditions. Resulting values were averaged from the 40 ns production trajectories at constant pressure of 1 atm. Molecular parameters other than PC partial charges[75] are from Gromacs OPLS-aa force field. The solid dot is the experimental result at 25C.[116] Numerical values are given in Table 4.2.

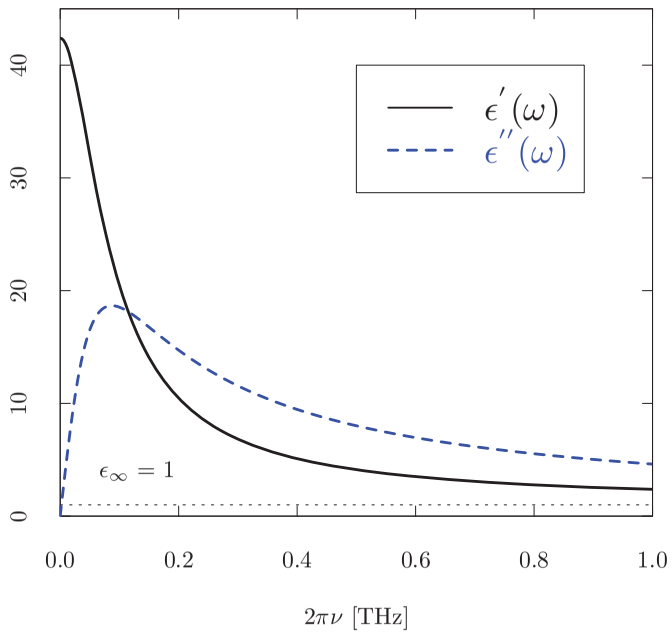

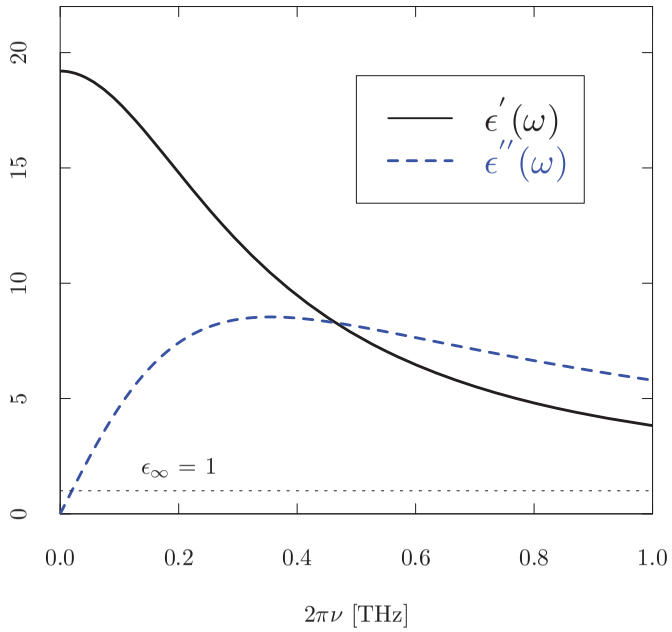

Figure 4.17: Dielectric constant and loss for liquid PC at $P = 1$ atm, $T = 400$K (upper) and $T = 600$K (lower).

The temperature dependence of relaxation time may be modeled as

$$\tau = A \exp(\Delta H^* / RT) \ , \tag{4.11}$$

where the ΔH^* is the molar activation enthalpy. A is the pre-exponential factor, which can be assumed to have a temperature dependence or treated as a constant. However, the exact form of this pre-factor haven't been reached an agreement in the historical studies.[162–164]

Excluding the pre-factor A, the relationship between relaxation time the activation enthalpy can be represented as

$$\ln(\tau) \propto \Delta H^* / RT \ . \tag{4.12}$$

Therefore, ΔH^* can be evaluated from the slope of linear plot $\ln(\tau) \sim 1/T$ (Fig. 4.18). In our temperature range of 280K to 600K, the calculated $\Delta H^* = 3.47$ kcal/mol.

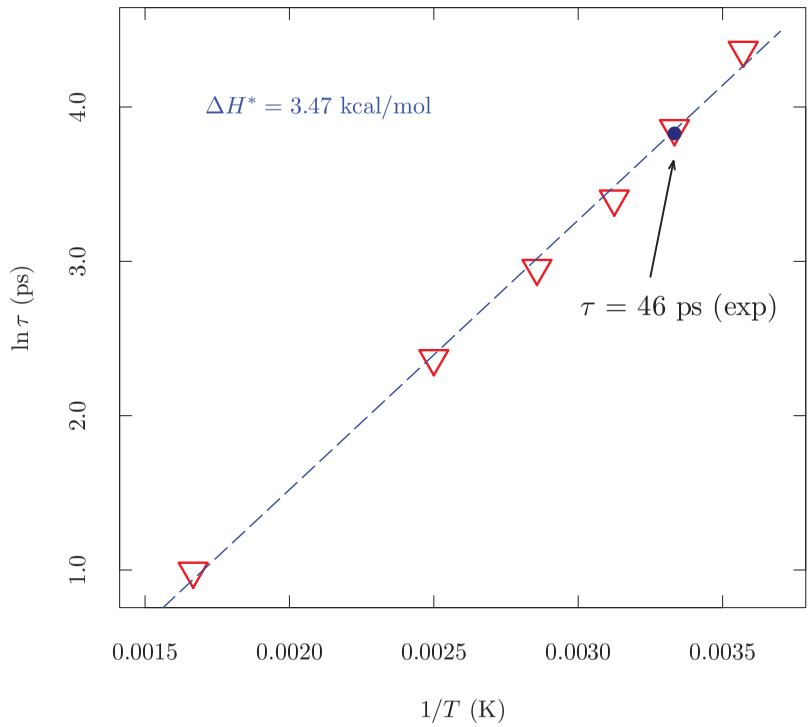

Figure 4.18: Dielectric relaxation time of liquid PC at $p = 1$ atm. The enthalpy of activation (ΔH^*) is 3.47 kcal/mol. Numerical values are given in Table 4.2.

4.3 Conclusions

Here we characterize the charging and discharging processes for EDLCs by direct simulating of $TEABF_4$/PC solution filling of CNT forests. Recent studies of interfacial properties of PC have laid the basis for this simulation model. Explicating the rates of charging responses and the kinetic characteristics associated with the confinement and the anisotropic environment. The friction kernel (memory function, or autocorrelation of random forces) $\gamma(t)$ (Eq. (4.2)) is obtained utilizing linear-equation solving after discretization, or specialized Fourier transform method. For strongly bound liquids, the memory function exhibits two distinct relaxations with the longer time-scale relaxation associated with attractive intermolecular forces. Dielectric relaxation time for PC is 47.5 ps which consistents to the experimental results 46 ps at $T = 300$K.

4.4 Methods

Direct simulations of filling CNT forest with $TEABF_4$/PC were carried out by GROMACS packages in an isothermal-isobaric ensemble (NPT) with periodical boundaries at $T = 300$K, $p = 1$ atm. Temperature was maintained by Nose-Hoover thermostat. System sizes ranged from 18,000 to 35,000 atoms, depending on the interstitial space of the CNT forest. The 300-atom carbon nanotubes are capped with half of a buckyball, C_{360} in total. Electronic structure calculations were performed by Gary Hoffman with Gaussian 03 using the PBE density functional and the 3-21G split-valence basis set.[165] All the other parameters are adopted from GROMACS OPLS all-atom force field. For each charge level, 50ns production equilibrium run was performed after a 50ns-aging period. All Trajectories were constructed with a time step of 1 fs. Configurations were saved every 5 ps for further analysis.

For the mean square displacement and velocity autocorrelation function cal-

culations, 1 ns simulations were performed with a time step 1 fs. Trajectories were saved at each 10 steps.

Bulk liquid simulation details for propylene carbonate, ethylene carbonate, acetonitrile, water (TIP4P-EW model) are provided in the captions of Fig: 4.5 and Fig: 4.7.

Dielectric relaxation properties were calculated from 1 ns bulk liquid simulations with configurations saved every 1 fs.

Chapter 5

Multi-scale Theory in the Molecular Simulation of Electrolyte Solutions

5.1 Introduction

This chapter develops statistical mechanical theory with the goal of treating electrolyte solutions at chemical resolution. Our context is current research on electrochemical double-layer capacitors (EDLCs) based on nanotube forests.[75] The requirement of chemical resolution means that electronic structure must be an integral part of the theory consistent with the natural interest in chemical features of EDLCs.

Ab initio molecular dynamics (AIMD), though not statistical mechanical theory, is available to simulate electrolyte solutions. Compared to classic molecular simulations with empirical model force-fields, AIMD calculations are severely limited in space and time scales, by more than an order-of-magnitude in each. Consequently, application of AIMD is not feasible for EDLCs at scales that are experimentally interesting. This calls for further theory to embed AIMD methods in studies of EDCLs.

Change-of-scale consequences are a primitive goal of fundamental statistical mechanical theory. That basic perspective is explicit in the classic phase transition literature,[166] and it has long been relevant to the theory of electrolyte solutions specifically.[167,168] This paper organizes several basic results of the statistical mechanics of solutions to treat electrolyte solutions where space and time scales will otherwise prohibit direct AIMD calculations. Our results here suggest a role for AIMD somewhat analogous to sub-grid modeling in computational fluid mechanics. Nevertheless, the goals of the statistical thermodynamics of complex solutions are distinct, and we do not propose transfer of results here between those fields.

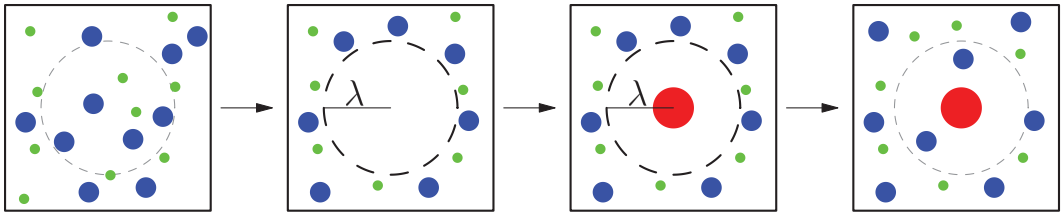

Figure 5.1: Evaluation of the excess chemical potential of a distinguished ion (red disk), patterned according to QCT. The blue and green disks are other ions in the system, and the solvent is in the background. The stepwise contributions are "packing," "outer shell," and "chemical" contributions, from left to right. See the text and Eq. 5.11 for further discussion.

Our development here utilizes several theoretical results that are "...both difficult and strongly established ..."[167] We put burdensome technical results in appendices, and in this introduction give a fuller discussion of the line of reasoning.

The initial step in our development is the McMillan-Mayer (MM) theory[167,169,170] *integrating out* of solvent degrees of freedom. MM theory is a pinnacle of coarse-graining for the statistical mechanics of solutions, it achieves a vast conceptual simplification the theory of electrolyte solutions. No sacrifice of molecular realism is implied by MM theory, and all primitive electrolyte solution models rest on it. But cataloging the multi-body potentials required for a literal MM application is pro-

hibitive.[171] Therefore, use of MM theory to construct a specific primitive model for a system of experimental interest has been limited.[172,173] Indeed, the MM theory is not generally suitable for specific molecular-scale implementation.

To address this we exploit *quasi-chemical theory* (QCT) which is formally complete in its modern expression.[117,174] QCT evaluates solvation free energies by breaking them into contributions with clear physical meanings. One contribution is a *packing* contribution. This can be simple in the anticipated applications because the solvent is not involved specifically, and the ion concentrations are not prohibitively high. A second contribution — the *outer shell* contribution — treats ion-ion interactions at long-range and it is expected on physical grounds that the necessary MM interactions should be simple then. That outer-shell contribution is studied below.

The final contribution — the *chemical* contribution — treats ion-ion inner-shell neighbors. Smaller spatial scales must be directly confronted and it is here that the sub-grid AIMD activity comes into play. Fig. 5.1 shows a now-standard picture of this organization of the statistical thermodynamical problem.

This discussion suggests that van der Waals theory is a subset of the present QCT approach. This is advantageous because van der Waals theory is the basis of the theory of liquids viewed broadly.[133,175] While paying an unavoidable price of significant computational effort, QCT goes beyond van der Waals theory in several ways. For example here, where ion-pairing is an essential part of the physical picture, associative phenomena are treated fully. Furthermore, our QCT implementation would routinely treat outer-shell interactions through gaussian order rather than the mean-field approach of classic van der Waals theories. This is essential in the present applications in order to capture the physical effect of Debye screening of ion correlations.

It is an interesting physical point that the identification of *packing* and *chemi-*

cal contributions here is a consequence of a choice of conditioning event, in the present development the emptiness of the inner-shell. This has the advantages that the theory is a close relative of van der Waals theory, and that the outer-shell contribution should be particularly simple to evaluate. But other choices of conditioning event are possible too.[120] For example, the conditioning event might be the event that the occupancy of the inner-shell is the value most probably observed. This has the intuitive attraction of being close to simple observations. But it presents the challenge that the evaluation of the partition function for that case might be more difficult. In what follows, our primary emphasis is to characterize the computational effort to evaluate the partition function associated with *outer-shell* contribution that arises with the original suggestion for the conditioning event.

5.2 Basic Theory Required

5.2.1 McMillan-Mayer theorem

The osmotic pressure, π, is evaluated as the partition function

$$\mathrm{e}^{\beta\pi V} = \sum_{\boldsymbol{n}_\mathrm{A}\geq 0} \mathcal{Z}\left(\boldsymbol{n}_\mathrm{A};\boldsymbol{z}_\mathrm{S}\right)\left(\frac{\boldsymbol{z}_\mathrm{A}{}^{\boldsymbol{n}_\mathrm{A}}}{\boldsymbol{n}_\mathrm{A}!}\right) , \tag{5.1}$$

involving only the solute species A. Here V is the volume, $k_\mathrm{B}T = \beta^{-1}$ the temperature, and the activity of the solvent (species S) is denoted by $z_\mathrm{S} = \mathrm{e}^{\beta\mu_\mathrm{S}}$. Eq. 5.1 involves

$$\mathcal{Z}\left(\boldsymbol{n}_\mathrm{A};\boldsymbol{z}_\mathrm{S}\right) = \left[\lim_{\boldsymbol{z}_\mathrm{A}\to 0}\left(\frac{\rho_\mathrm{A}}{z_\mathrm{A}}\right)^{\boldsymbol{n}_\mathrm{A}}\right]\int_V \mathrm{d}1_\mathrm{A}\ldots\int_V \mathrm{d}n_\mathrm{A}\mathrm{e}^{-\beta W(1_\mathrm{A}\ldots n_\mathrm{A})} , \tag{5.2}$$

with ρ_{A} being the density of solutes, and with the potentials-of-average-force given by

$$W\left(1_{\mathrm{A}}\ldots n_{\mathrm{A}}\right)=-\frac{1}{\beta}\ln g\left(1_{\mathrm{A}}\ldots n_{\mathrm{A}};\boldsymbol{z}_{\mathrm{S}},\boldsymbol{z}_{\mathrm{A}}=0\right)\ , \tag{5.3}$$

which depends on the the activity of the solvent. Eq. 5.2 is compact, thermodynamically explicit, and general; see the Appendix for an accessible derivation and fuller discussion.

5.2.2 Potential distribution theorem (PDT)

The solute chemical potential may be expressed as

$$\beta\mu_{\mathrm{A}}=\ln\rho_{\mathrm{A}}{\Lambda_{\mathrm{A}}}^{3}/q_{\mathrm{A}}^{(\mathrm{int})}+\beta\mu_{\mathrm{A}}^{(\mathrm{ex})}\left(z_{\mathrm{A}}=0\right)-\ln\left\langle\left\langle\mathrm{e}^{-\beta\Delta W_{\mathrm{A}}^{(1)}}\right\rangle\right\rangle_{0}\ . \tag{5.4}$$

The binding energy of a distinguished solute (A) molecule in the MM system is

$$\Delta W_{\mathrm{A}}^{(1)}=W\left(\boldsymbol{n}_{A}+1\right)-W\left(\boldsymbol{n}_{A}\right)-W\left(1\right)\ . \tag{5.5}$$

The middle term of Eq. 5.4,

$$\beta\mu_{\mathrm{A}}^{(\mathrm{ex})}\left(z_{\mathrm{A}}=0\right)=-\ln\left\langle\left\langle\mathrm{e}^{-\beta\Delta U_{\mathrm{A}}^{(1)}}\right\rangle\right\rangle_{0}\ , \tag{5.6}$$

is evaluated at infinite dilution of the solute. This evaluation is typically highly non-trivial, but much has been written about that[117,174] and we will proceed to analyze that right-most term of Eq. 5.4.

5.2.3 Quasi-chemical theory

Thus we study

$$\beta\Delta\mu_{\mathrm{A}}^{(\mathrm{ex})} = \beta\mu_{\mathrm{A}}^{(\mathrm{ex})} - \beta\mu_{\mathrm{A}}^{(\mathrm{ex})}\left(z_{\mathrm{A}}=0\right) = -\ln\left\langle\left\langle \mathrm{e}^{-\beta\Delta W_{\mathrm{A}}^{(1)}}\right\rangle\right\rangle_0 \ . \tag{5.7}$$

$\Delta\mu_{\mathrm{A}}^{(\mathrm{ex})}$ is the contribution to the chemical potential of species A in excess of the infinite dilution result, due to inter-ionic interactions with the influence of solvent fully considered.

A quasi-chemical development of Eq. 5.7 starts by characterizing neighborship. If the species considered are ions in solution, then we need to characterize ion neighbors of each ion in solution, distinguished in turn. Pairing of oppositely charged ions has been the subject of classic scientific history[113] that can inform the present discussion. Pairing of tetra-fluoroborate 1-hexyl-3-methylimidazolium in pentanol has recently been studied both experimentally and computationally.[176]

Pairing of tetra-ethylammonium tetra-fluoroborate in propylene carbonate is a helpful example.[113] In that case, pairing is simple to observe for saturated solution conditions and formation of chains and rings of ions is consistent with the molecular-scale observations. We might consider an indicator function χ_{AB} with the requirement that $\chi_{\mathrm{AB}} = 1$ indicates *no* B ions are within an inner-shell stencil of a distinguished A ion. The simplest possibility, natural for compact molecular ions, is to identify a central atom in A and in B ions, and to set $\chi_{\mathrm{AB}} = 1$ (but zero otherwise), when those atoms of further apart than a designated distance λ_{AB}.

Even simpler, and satisfactory for the primitive model that follows below, we might identify a central atom for ion A, then define a spherical inner-shell by the radius λ_{A} with the requirement that *no* other ions be closer than that. In fact, we choose the same radius for cations and anions in the primitive model studied below,

$\lambda_{\mathrm{A}} = \lambda_{\mathrm{A}} = \lambda$.

Eq. 5.7 was derived using the grand canonical ensemble. But implementation with simulations in the grand canonical ensemble would be painful. Calculations with *canonical* ensemble methods should be satisfactory. In what follows we will develop Eq. 5.7 from the perspective on the canonical ensemble. Appendix C discusses the relevant ensemble differences.

The canonical ensemble average of $\mathrm{e}^{\beta\Delta W_{\mathrm{A}}^{(1)}}\chi_{\mathrm{A}}$ gives

$$\left\langle \mathrm{e}^{\beta\Delta W_{\mathrm{A}}^{(1)}}\chi_{\mathrm{A}} \right\rangle = \frac{\left\langle\left\langle \mathrm{e}^{-\beta\Delta W_{\mathrm{A}}^{(1)}}\mathrm{e}^{\beta\Delta W_{\mathrm{A}}^{(1)}}\chi_{\mathrm{A}} \right\rangle\right\rangle_0}{\left\langle\left\langle \mathrm{e}^{-\beta\Delta W_{\mathrm{A}}^{(1)}} \right\rangle\right\rangle_0} = \mathrm{e}^{\beta\Delta\mu_{\mathrm{A}}^{(\mathrm{ex})}} \left\langle\left\langle\chi_{\mathrm{A}}\right\rangle\right\rangle_0 \ . \tag{5.8}$$

In addition, for indicator function χ_{A}, and some other quantity G we have

$$\langle G\chi_{\mathrm{A}}\rangle = \langle G|\chi_{\mathrm{A}} = 1\rangle \langle\chi_{\mathrm{A}}\rangle \ . \tag{5.9}$$

Collecting these relations yields

$$\mathrm{e}^{\beta\Delta\mu_{\mathrm{A}}^{(\mathrm{ex})}} = \left\langle \mathrm{e}^{\beta\Delta W_{\mathrm{A}}^{(1)}}|\chi_{\mathrm{A}} = 1\right\rangle \times \frac{\langle\chi_{\mathrm{A}}\rangle}{\left\langle\left\langle\chi_{\mathrm{A}}\right\rangle\right\rangle_0} \ . \tag{5.10}$$

After evaluating the logarithm and replacing the conditional ensemble average with an integral over a conditional probability distribution, we get

$$\beta\Delta\mu_{\mathrm{A}}^{(\mathrm{ex})} = -\ln\left\langle\left\langle\chi_{\mathrm{A}}\right\rangle\right\rangle_0 + \ln\int \mathrm{e}^{\beta\varepsilon} P_{\mathrm{A}}\left(\varepsilon|\chi_{\mathrm{A}} = 1\right) d\varepsilon + \ln\langle\chi_{\mathrm{A}}\rangle \tag{5.11}$$

where

$$P_{\mathrm{A}}\left(\varepsilon|\chi_{\mathrm{A}} = 1\right) = \left\langle \delta\left(\varepsilon - \Delta W_{\mathrm{A}}^{(1)}\right)|\chi_{\mathrm{A}} = 1\right\rangle \ . \tag{5.12}$$

These three terms correspond to the three processes in Fig. 5.1.

c (mol/dm^3)	L (nm)	$n_{\text{ion-pairs}}$	κ^{-1} (nm)	$\beta q^2\kappa/2\epsilon$
0.01	32.15	200	2.67	0.17
0.05	18.80	200	1.19	0.39
0.1	14.92	200	0.84	0.55
0.2	11.84	200	0.60	0.77
0.4	9.4	200	0.42	1.11
0.5	9.4	250	0.37	1.26
0.6	9.4	300	0.34	1.37
0.8	9.4	400	0.30	1.55
1.0	9.4	500	0.27	1.72
2.0	7.4	500	0.19	2.44

Table 5.1: Specifications for Monte Carlo simulation of a primitive model with dielectric constant, ion charges and sizes corresponding to the atomically detailed [TEA][BF_4]/PC case.[113] Specifically the model dielectric constant is $\epsilon = 60$, and $d_{++} = 0.6668$ nm, $d_{--} = 0.6543$ nm, $d_{-+} = 0.45$ nm are distances of closest approach for the hard spherical ions. These calculations utilized the Towhee[76] package adapted to the present system, conventional cubical periodic boundary conditions at $T = 300$K, and the indicated concentrations c. Each calculation was extended to 10^6 cycles after aging, each cycle comprising $2n_{\text{ion-pairs}}$ attempted moves. 10,000 configurations are saved and used for the following analyses.

5.3 Numerical demonstration

We have tested how Eq. 5.11 works numerically on the basis of a primitive electrolyte solution model that was designed to correspond to the TEABF_4/PC. Table. 5.1 describes the model further and indicates the thermodynamic states studied by Monte Carlo calculations. The radial distribution functions (Fig. 5.2) show why this primitive model, with non-additive hard-sphere interactions, was identified to study ion-pairing.

In this case, the packing and chemistry contributions can be directly calculated by trial insertions (for *packing* and $\langle\langle\chi_{\text{A}}\rangle\rangle_0$), and observation of the closest neighbor molecule distance distribution (for *chemistry* and $\langle\chi_{\text{A}}\rangle$). That leaves the *outer-shell* contribution which is our particular interest here.

For the general theory (Eq. 5.11 and Eq. 5.1), the distinguished ion will be

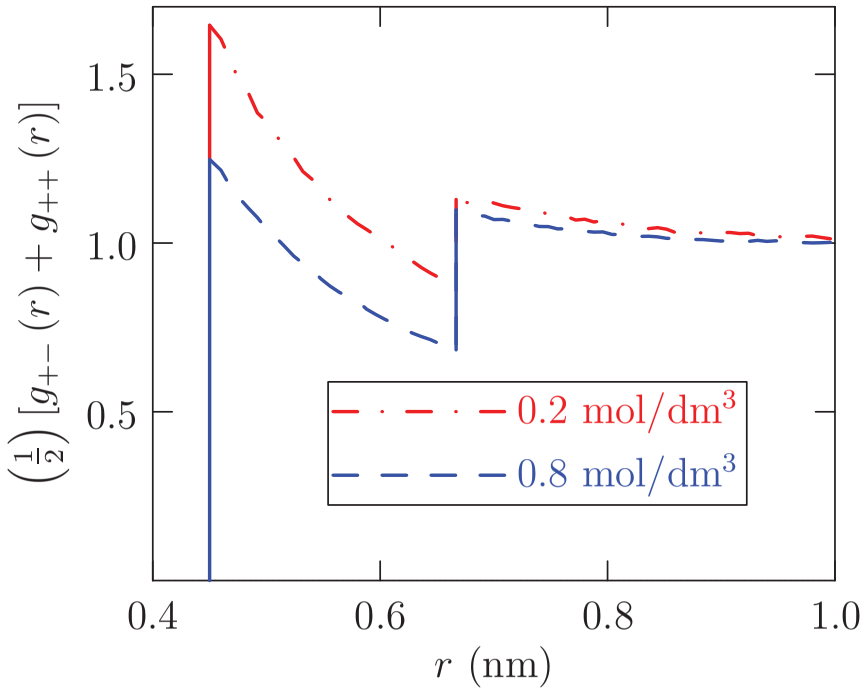

Figure 5.2: The radial distribution functions of $c = 0.2$ mol/dm^3 and $c = 0.8$ mol/dm^3 from cation to other ions. These two vertical lines identify the closest approach distances, which are 0.45 nm and 0.6668 nm in this case.

separated by a substantial distance from all other ions. We assume that the required binding energy can be approximated as a superposition of the pair potential-of-mean-force at long-range between the distinguished ion and all ion neighbors, which we take to be the classic macroscopic result $q_i q_j / 4\pi\epsilon r$ for a separation of r. That superposition is just the electrostatic inter-ionic potential energy of interaction for the primitive model considered here.

The system size correction of Hummer, *et al.*[177] was applied to all binding energies, and thus to the free energies evaluated here.[125]

5.3.1 Binding energy distributions

We evaluate binding energies for the primitive model by standard Ewald calculation for configurations extracted from the Monte Carlo simulations, $\varepsilon = \Delta W_{\mathrm{A}}^{(1)}$. We examine the distributions of binding energies for the ions present in the simulation,

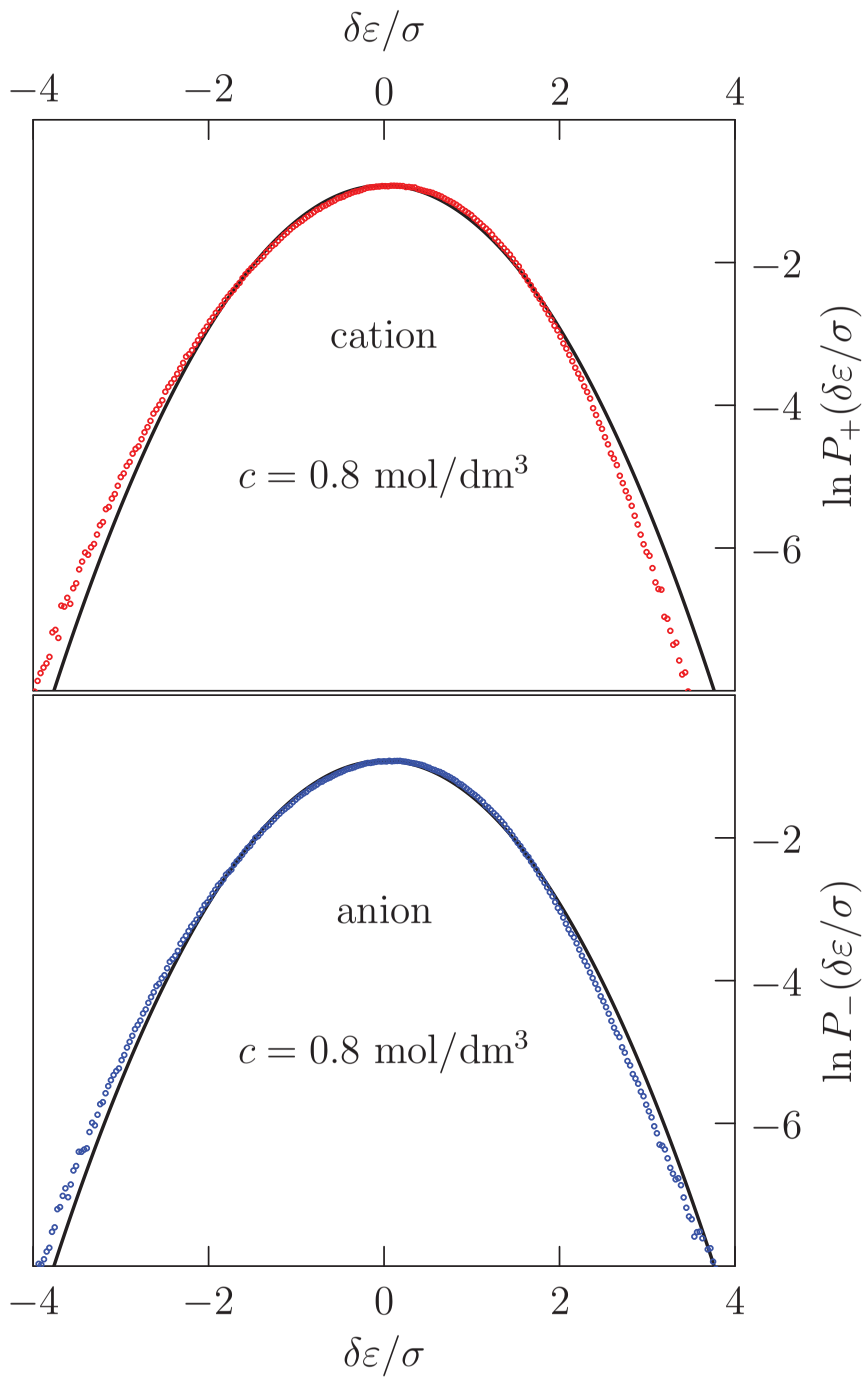

Figure 5.3: Observed distributions of ion binding energies, shifted and scaled into standard normal form, for $c = 0.8$ mol/dm^3. The parabolae (solid black lines) here are standard normal comparisons.

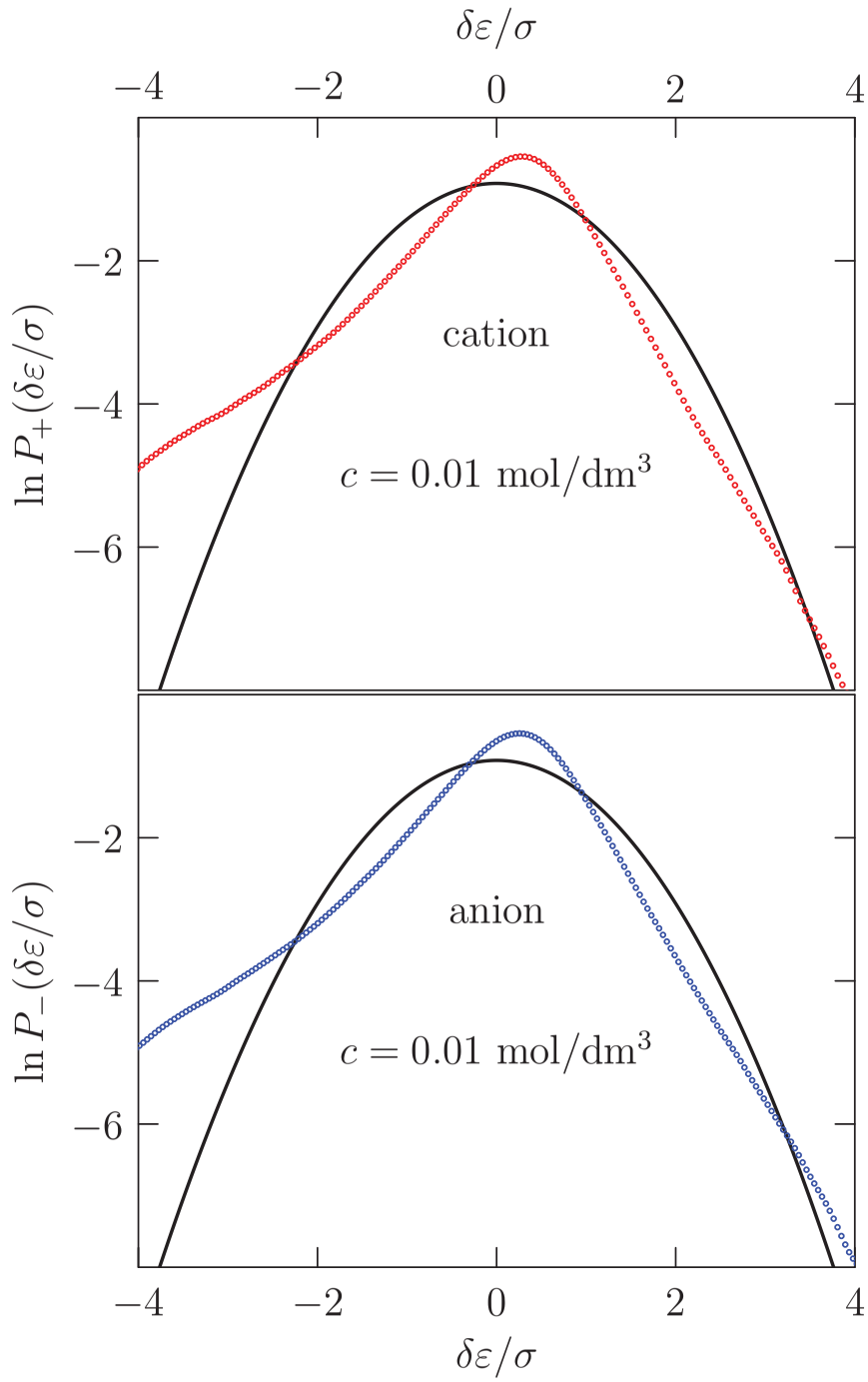

Figure 5.4: Observed distributions of ion binding energies, shifted and scaled into standard normal form, for $c = 0.01$ mol/dm^3. The parabolae (solid black lines) here are standard normal comparisons.

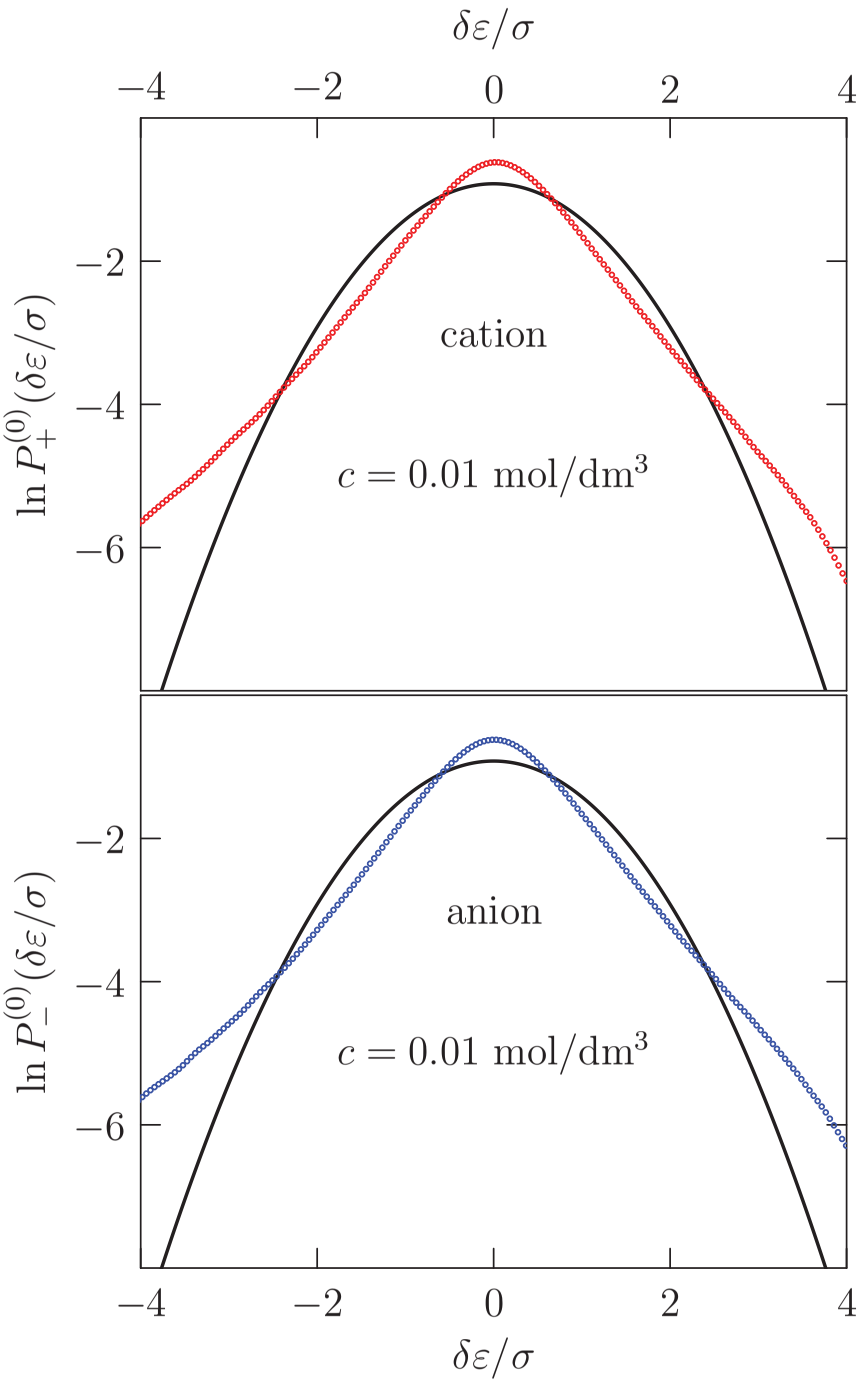

Figure 5.5: Observed distributions of uncoupled ion binding energies, shifted and scaled into standard normal form, for $c = 0.01$ mol/dm^3. The parabolae (solid black lines) here are standard normal comparisons.

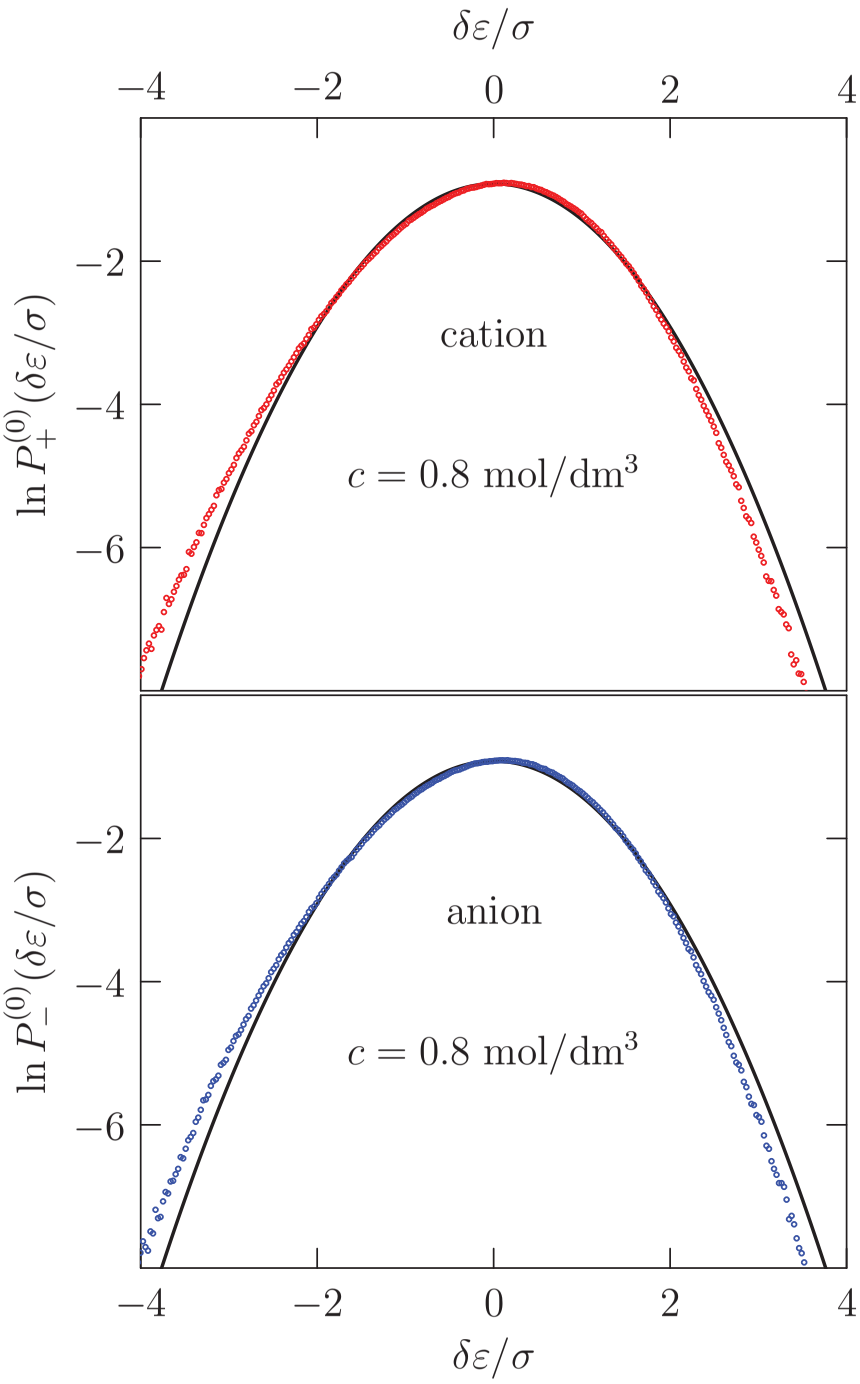

Figure 5.6: Observed distributions of uncoupled ion binding energies, shifted and scaled into standard normal form, for $c = 0.8$ mol/dm^3. The parabolae (solid black lines) here are standard normal comparisons.

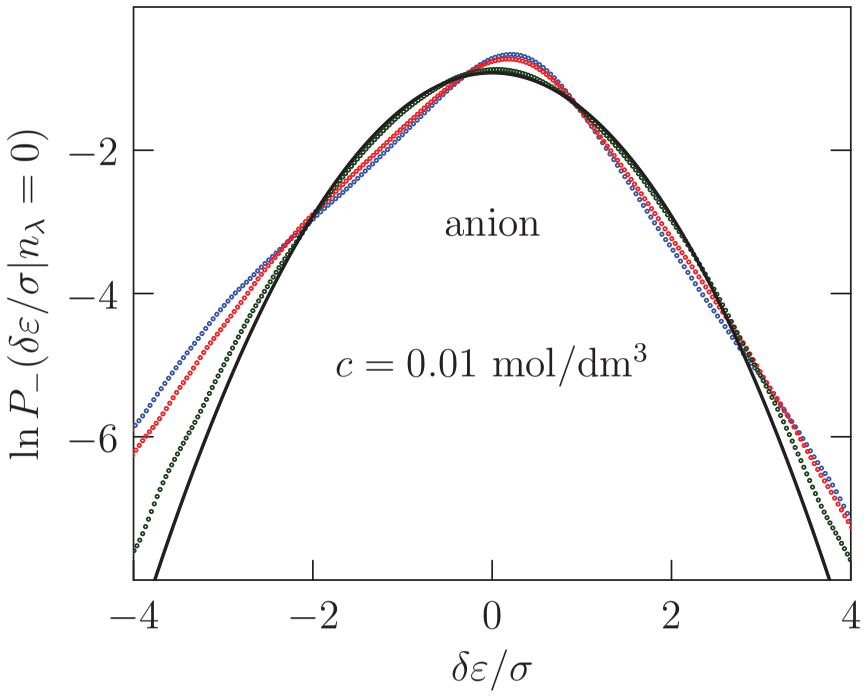

Figure 5.7: Probability density functions for the outer-shell binding energy for the anions in the simulation of Table. 5.1, for the lowest concentration there, with $\lambda =$ 0.7, 0.9, and 2.0 nm (blue, red, and darkgreen respectively), compared the standard normal (solid black curve). This demonstates how increasing λ enforces better Gaussian behavior for this distribution.

$P(\varepsilon)$, and also binding energies for permissible trial placements of additional anions or cations, $P^{(0)}(\varepsilon)$. In order to have a basis for comparison, we do these calculations first *without* the conditioning prescribed by QCT, *i.e.*, all anions or cations without regard to their neighborship status. Distributions of those binding energies (Fig. 5.3, 5.4, 5.5, and 5.6) are striking. At the higher concentration shown (Fig. 5.3), the distributions are reasonably normal as expected. At the lower concentration shown (Fig. 5.4), the distributions are non-gaussian. The design of the model to reflect ion-pairing is evident in the enhanced weight at substantially negative binding energies.

The normal presentation (as in Fig. 5.3, 5.4, and 5.5, shift-scaled and compared to standard normal) helps to judge the width of these distributions. An alternatively presentation (Fig. 5.8 and 5.9) compares these binding energy ranges to the thermal energy kT and gives additional insight. The free energy prediction from the coupled distributions (Fig. 5.3 and 5.4) depends sensitively on the high-ε (right) wing of these graphs and hardly at all on the low-ε (left) wing. Even though the low-concentration distribution (Fig. 5.4) is strikingly non-gaussian, the right-wing extends, very roughly, to the same width as the natural gaussian. In contrast the uncoupled $P^{(0)}(\varepsilon)$ (Fig. 5.5) is qualitatively non-gaussian in both high-ε and low-ε wings.

The uncoupled $P^{(0)}(\varepsilon)$ (Fig. 5.5) at low concentration also distinctly abnormal, in both wings; at high-concentration they (Fig. 5.6) more nearly gaussian.

5.3.2 QCT conditioned binding energy distributions

We next consider the conditioned distributions that arise with the QCT approach (Eq. 5.11 and Fig. 5.1). We take the inner-shell to be a sphere of radius λ centered on the ions. Typical results for $P_{-}(\delta\varepsilon/\sigma|n_\lambda = 0)$ for the interesting low concentration case (Fig. 5.7) shows how the conditioning affects this distribution, with increasing λ driving the distribution toward normal behavior.

5.3.3 Free energies and gaussian approximations

The goal of our QCT development is to break the free energy into parts associated first with simple observations, and finally with a partition function calculation (the *outer-shell* contribution) that can be well approximated by a gaussian model with simply observed parameters. In that case the *outer-shell* contribution of Eq. 5.11 would be

$$\ln \int \mathrm{e}^{\beta\varepsilon} P_{\mathrm{A}}\left(\varepsilon|\chi_{\mathrm{A}}=1\right) d\varepsilon \approx \beta\langle\varepsilon|\chi_{\mathrm{A}}=1\rangle + \beta^2\langle\delta\varepsilon^2|\chi_{\mathrm{A}}=1\rangle/2 \ . \tag{5.13}$$

To test these ideas, we evaluate the free energies directly, with and without the QCT conditioning, and also compare the results of the gaussian approximation Eq. 5.13.

The direct evaluation of the free energies follows Bennett's method,[178] and searches for the value $\Delta\mu^{(\mathrm{ex})}$ that solves

$$\left\langle \frac{1}{1+\mathrm{e}^{-\beta\left(\varepsilon-\Delta\mu_{\mathrm{A}}^{(\mathrm{ex})}\right)}} \right\rangle = \left\langle \frac{1}{1+\mathrm{e}^{\beta\left(\varepsilon-\Delta\mu_{\mathrm{A}}^{(\mathrm{ex})}\right)}} \right\rangle_0 \tag{5.14}$$

for each species considered. The average on the left is estimated with the sample associated with $P_{\mathrm{A}}(\varepsilon)$ whereas the average on the right of uses the binding energies leading to $P_{\mathrm{A}}^{(0)}(\varepsilon)$ associated with permissible trial placements.

5.3.3.1 No conditioning

In this case, we estimate a non-electrostatic contribution directly by trial insertions, then electrostatic contribution on the basis of distributions such as Fig. 5.4 and Fig. 5.5. The mean activity coefficients (Fig. 5.10) obtained with the gaussian approximation and the Bennett evaluation are qualitatively similar but quantitatively different from each other.

5.3.3.2 Pointwise Bennett comparison

A more specific statement of the Bennett approach is

$$\frac{P(\varepsilon)}{1+\mathrm{e}^{-\beta\left(\varepsilon-\Delta\mu^{(\mathrm{ex})}\right)}} = \frac{P^{(0)}(\varepsilon)}{1+\mathrm{e}^{\beta\left(\varepsilon-\Delta\mu^{(\mathrm{ex})}\right)}} \ . \tag{5.15}$$

This relies on the basic relation

$$P(\varepsilon) = \mathrm{e}^{-\beta\left(\varepsilon-\Delta\mu^{(\mathrm{ex})}\right)} P^{(0)}(\varepsilon) \ , \tag{5.16}$$

and the elementary identity

$$\mathrm{e}^{-\beta\left(\varepsilon-\Delta\mu^{(\mathrm{ex})}\right)} = \frac{1+\mathrm{e}^{-\beta\left(\varepsilon-\Delta\mu^{(\mathrm{ex})}\right)}}{1+\mathrm{e}^{\beta\left(\varepsilon-\Delta\mu^{(\mathrm{ex})}\right)}} \ . \tag{5.17}$$

Eq. 5.15 assembles information from $P(\varepsilon)$ and $P^{(0)}(\varepsilon)$, and thus illuminates the behavior of the important wings, high-ε for $P(\varepsilon)$ and low-ε for $P^{(0)}(\varepsilon)$. Typical results (Fig. 5.8 and 5.9) show reasonable match between the left and right side of Eq. 5.15. It is helpful to note that at the higher concentration shown (Fig. 5.9), the match in the low-probability wings is not perfect. A reasonable guess is that this is due to inaccuracy of $P^{(0)}(\varepsilon)$ at low-ε and that this is the reason behind the puzzling discrepancy between the Bennett result and the gaussian model seen in Fig. 5.10 and Fig. 5.13.

5.3.3.3 QCT conditioning

Though the various QCT contributions depend on the radius λ of the inner-shell (Fig. 5.11), the net free energy varies only slightly with increases of $\lambda > 0.7$ nm. The mean activity coefficients evaluated by the Bennett method and the gaussian approximation (Fig. 5.13) now accurately agree. This suggests that both approaches are physically reliable with this conditioning. In order that an MM pair-potential at

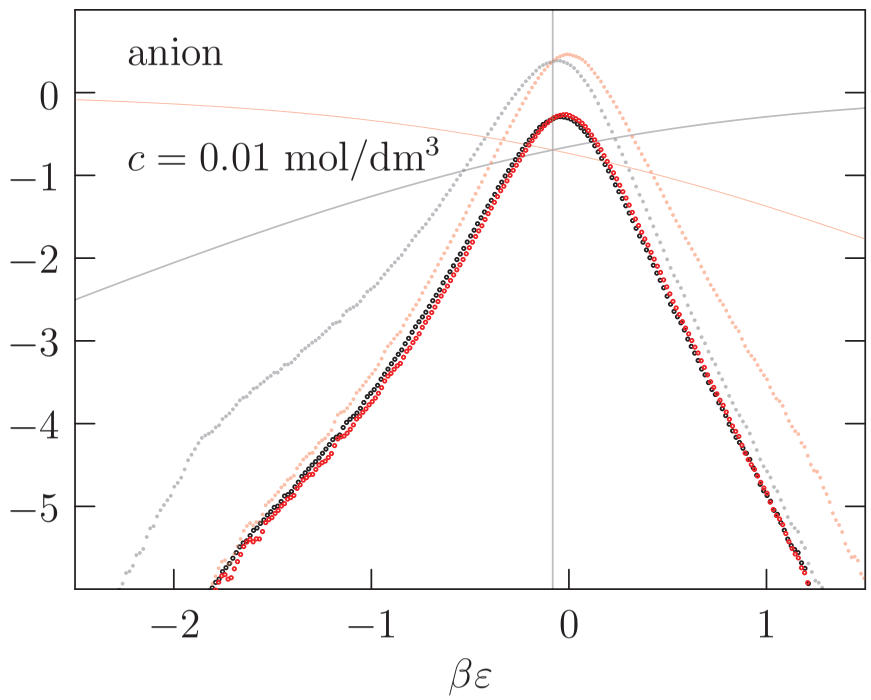

Figure 5.8: For the low concentration case of Table. 5.1. The bold circles are the logarithms of the functions left and right of Eq. 5.15, black and red, respectively. The pale solid curves are the corresponding weight factors, *e.g.* $-\ln\left[1+\mathrm{e}^{\beta\left(\varepsilon-\Delta\mu_\alpha^{(\mathrm{ex})}\right)}\right]$ for the red curve. The pale symbols are the plotted logarithms of the observed probability densities. The vertical line is the inferred value of the $\beta\Delta\mu_\alpha^{(\mathrm{ex})}$. Note the Eq. 5.15 is accurately satisfied.

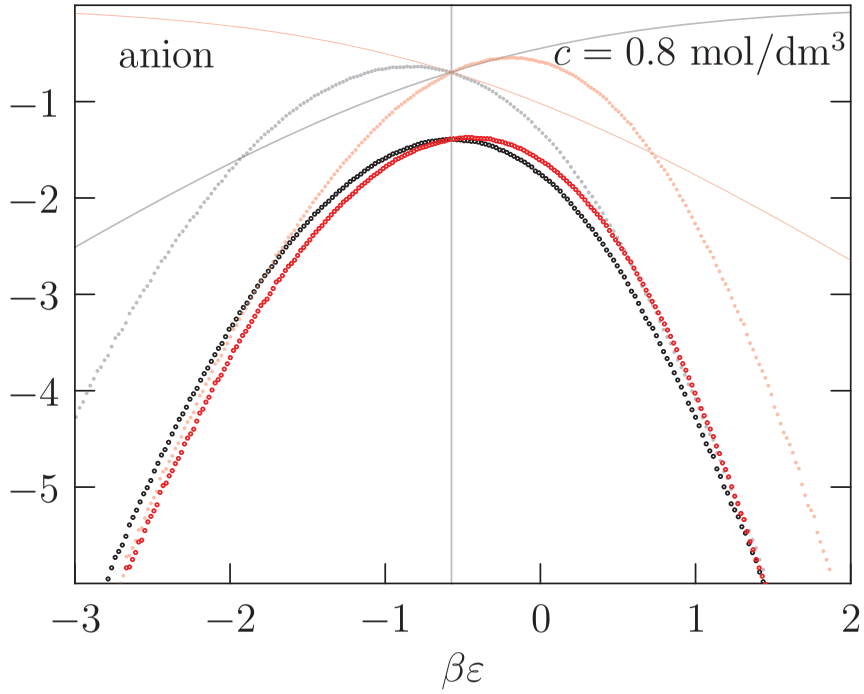

Figure 5.9: For the c=0.8 mol/dm^3 case of Table. 5.1. The bold circles are the logarithms of the functions left and right of Eq. 5.15, black and red, respectively. The pale solid curves are the corresponding weight factors, *e.g.* $-\ln\left[1+\mathrm{e}^{-\beta\left(\varepsilon-\Delta\mu_\alpha^{(\mathrm{ex})}\right)}\right]$ for the black curve. The pale symbols are the plotted logarithms of the observed probability densities. The vertical line is the inferred value of the $\beta\Delta\mu^{(\mathrm{ex})}$. Note the Eq. 5.15 is only roughly satisfied in the low-ε wing.

long-range may be plausibly exploited, the conditioning is essential to the broader idea here .

For the concentrations and λ values in Fig. 5.11, the Poisson estimates of the packing and chemical contributions[113]

$$-\ln \langle\langle\chi\rangle\rangle_0 \equiv -\sum_{\alpha} \ln \langle\langle\chi_\alpha\rangle\rangle_0 = \left(\frac{1}{2}\right) \sum_{\alpha,\gamma} \frac{4\pi}{3}\lambda^3 c \ , \tag{5.18}$$

$$-\ln \langle\chi\rangle \equiv -\sum_{\alpha} \ln \langle\chi_\alpha\rangle = \left(\frac{1}{2}\right) \sum_{\alpha,\gamma} 4\pi \int_0^\lambda c g_{\alpha\gamma}(r)\, r^2 \mathrm{d}r \ , \tag{5.19}$$

are useful. The combination

$$-\ln \left[\frac{\langle\langle\chi\rangle\rangle_0}{\langle\chi\rangle}\right] = -\left(\frac{1}{2}\right) \sum_{\alpha,\gamma} 4\pi \int_0^\lambda c\left[g_{\alpha\gamma}(r) - 1\right] r^2 \mathrm{d}r \ . \tag{5.20}$$

is then interesting. The utility of these results emphasizes again that the ion densities are not high, so simple results can be helpful.

5.4 Conclusions

This chapter organizes several basic theoretical results — McMillan-Mayer theory, the potential distribution approach, and quasi-chemical theory — to apply high-resolution AIMD to electrolyte solutions. The conceptual target for these considerations is that the last of the calculations depicted in Fig. 5.1 can be done by AIMD directly on the time and space scales typical of those demanding methods. This theory then develops a mechanism for addressing effects associated with longer spatial scales, involving also characteristically longer time scales. The theory treats composition fluctuations which would be accessed by larger-scale calculations, and also longer-ranged interactions and correlations that are of special interest for electrolyte solutions.

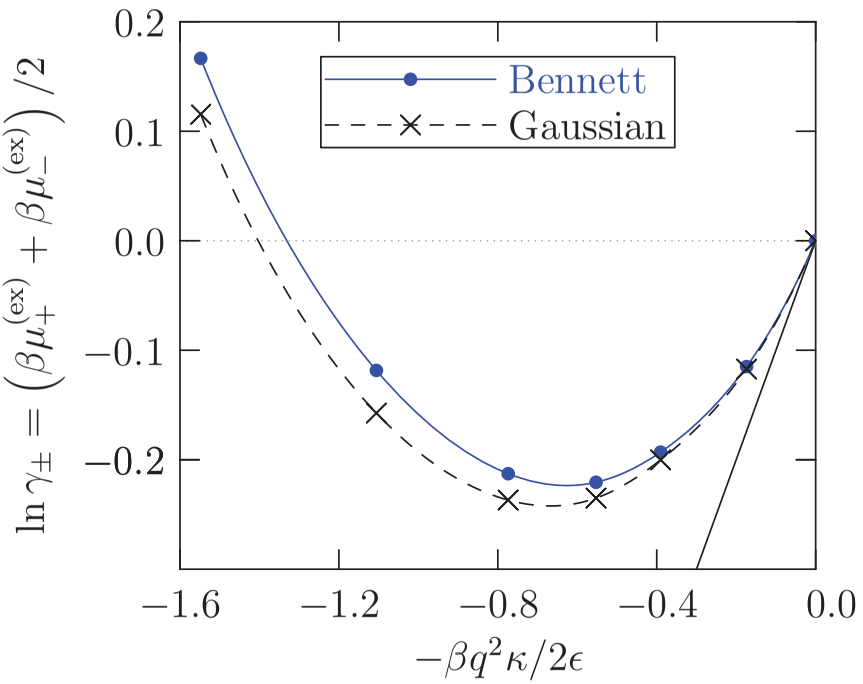

Figure 5.10: No conditioning, non-QCT, as discussed in Sec. 5.3.3.1. The solid black line is the Debye-Hückel limiting law. The points correspond to $c = \{0.01, 0.05, 0.1, 0.2, 0.4, 0.8\}$ mol/dm^3 cases of Table. 5.1

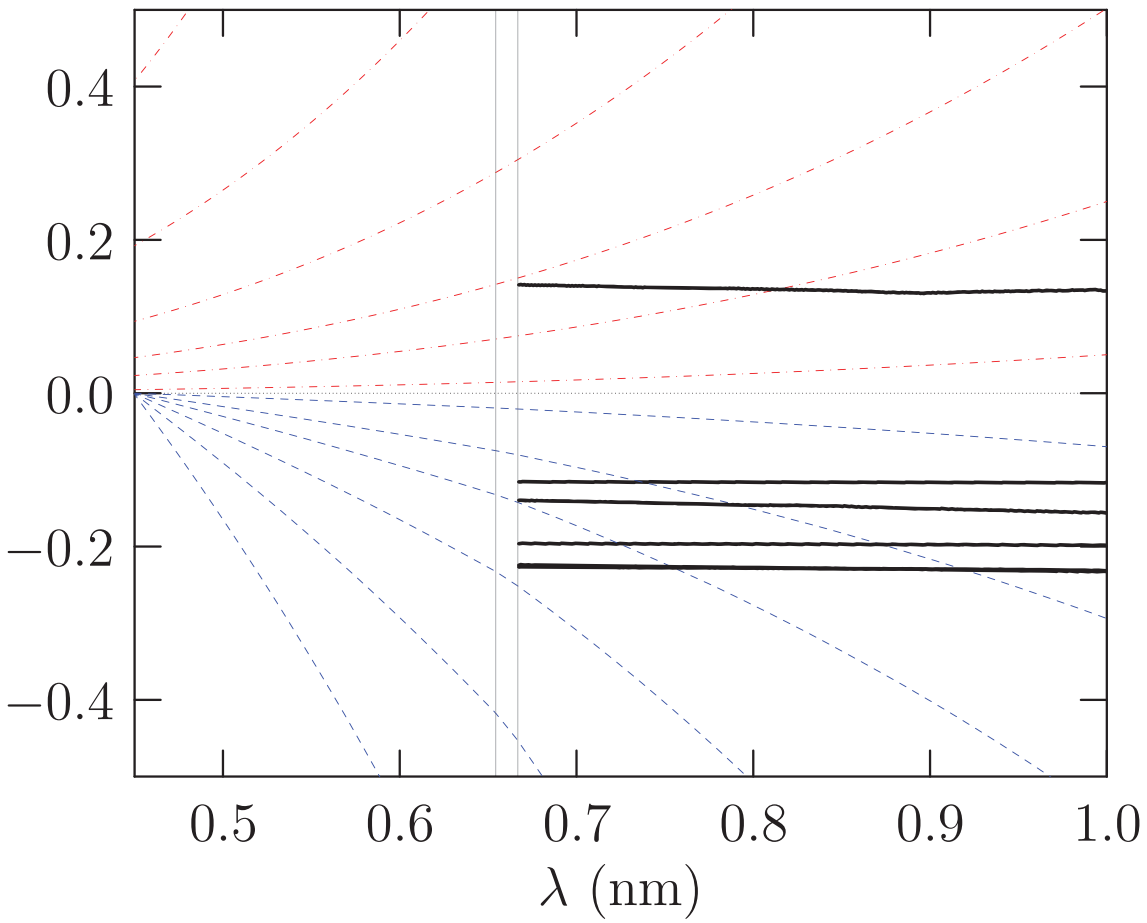

Figure 5.11: The red, blue, and black curves are the packing (arithmetic average of $-\ln\langle\langle\chi\rangle\rangle_0$ for the two ion types), chemical (arithmetic average of $\ln\langle\chi\rangle$ for the two ion types), and net contributions (following Eq. 5.11, including the outer-shell contribution, for $\ln\gamma_\pm$), respectively, for the primitive model results.[113] The various curves correspond to $c = \{0.01, 0.05, 0.1, 0.2, 0.4, 0.8\}$ mol/dm^3 cases of Table. 5.1.

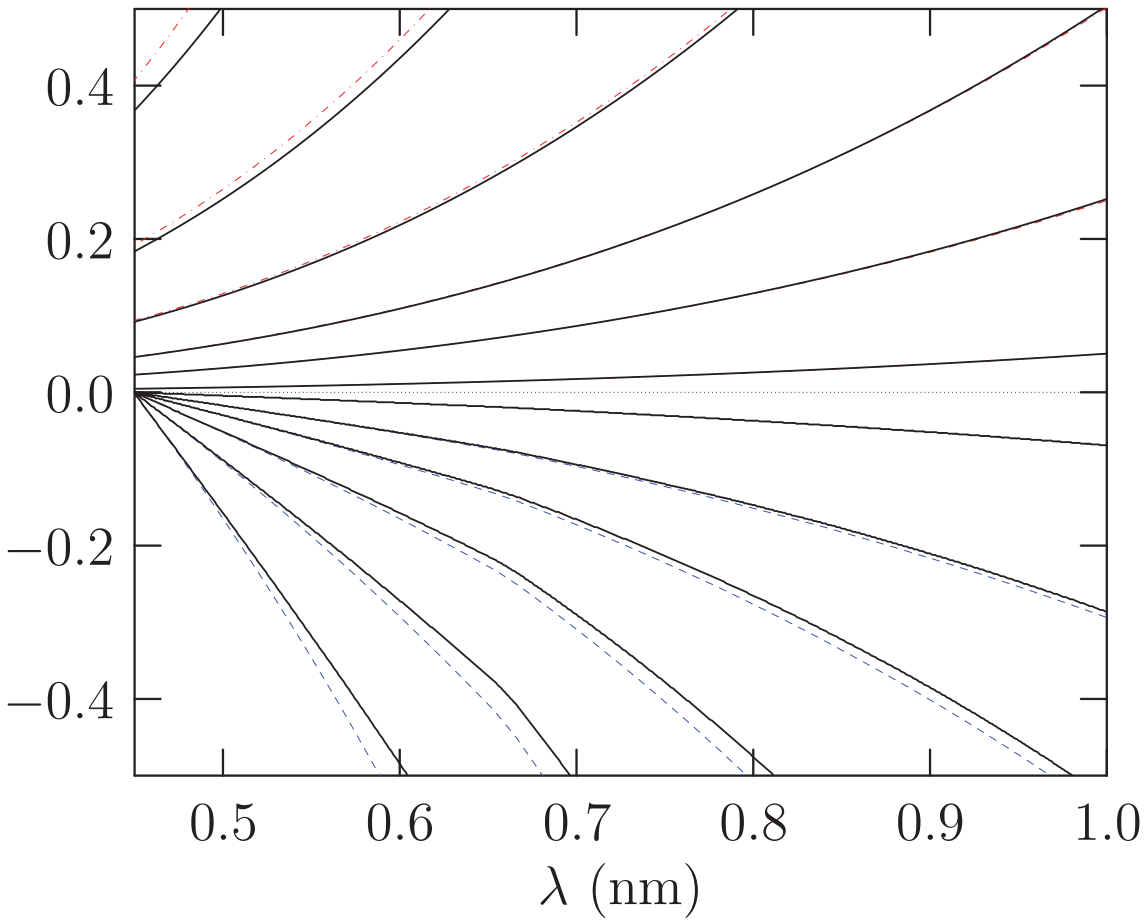

Figure 5.12: Upper black curves are the results from Eq. 5.18. Similarly, the red dot-dashed curves are the direct numerical results obtained by trail insertions. The lower black are the results from Eq. 5.19. Similarly, the blue dashed curves are the direct numerical results obtained by observations of the ions present in the simulations.

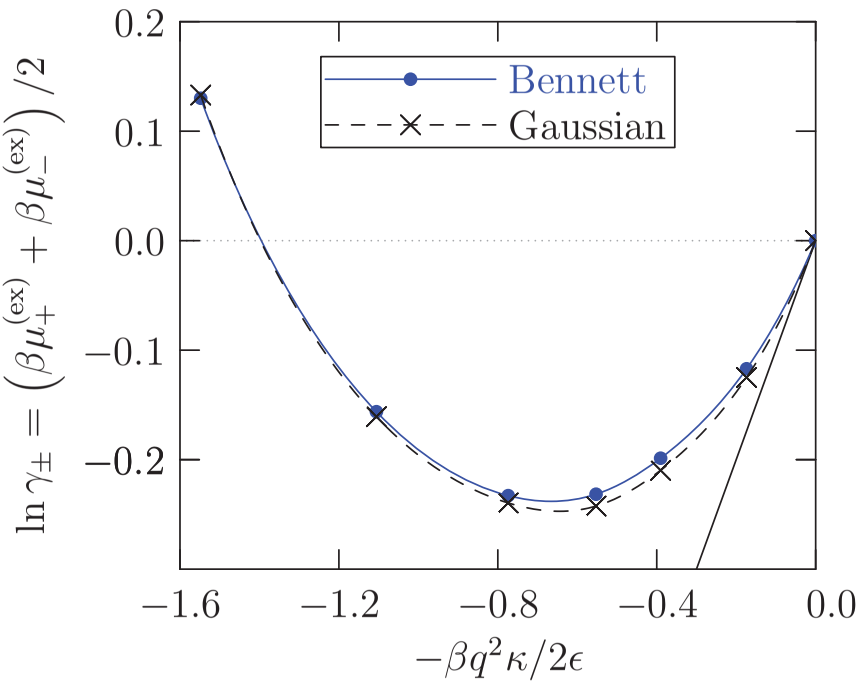

Figure 5.13: QCT, as discussed in Sec. 5.2.3. The solid black line is the Debye-Hückel limiting law.

The quasi-chemical organization, as an extension of van der Waals pictures, breaks-up governing free energies into physically distinct contributions: *packing*, *outer-shell*, and *chemical* contributions. This chapter adopted a primitive model suggested by observed ion-pairing in tetra-ethylammonium tetra-fluoroborate dissolved in propylene carbonate, then studied specifically the *outer-shell* contributions that expresses electrolyte screening. Gaussian statistical models are shown to be effective as physical models for these *outer-shell* contributions, and they are conclusive for the free energies within the quasi-chemical formulation (Fig. 5.11 and 5.13). In fact, with this data set the gaussian physical approximation is more efficient in providing an accurate mean activity coefficient than is the Bennett direct evaluation of that free energy (Fig. 5.10 and 5.13).

5.5 Methods

The primitive model simulation details are provided in Table. 5.1. The binding energy distribution and free energy calculations are done by Wei Zhang.

Chapter 6

Appendix

A: Accessible derivation of the McMillan-Mayer Theory

In the analysis of the MM theory, the formulae that are employed can be intimidating[179–181] at several stages so a physically clear notation helps. We consider a system composed of solvent (S) and solutes (A). The numbers of these species will be indicated by $\boldsymbol{n}_{\mathrm{S}}$ and $\boldsymbol{n}_{\mathrm{A}}$, the bold-face typography indicating that each of these quantities can be multi-component, *i.e.*, $\boldsymbol{n}_{\mathrm{A}} = \{n_{\mathrm{A}_1}, n_{\mathrm{A}_2}, \ldots\}$, and similarly for solvent species. The Helmholtz free energy $A(T, V, \boldsymbol{n}_{\mathrm{S}}, \boldsymbol{n}_{\mathrm{A}})$ then leads to the canonical partition function

$$\mathrm{e}^{-\beta A(T,V,\boldsymbol{n}_{\mathrm{S}},\boldsymbol{n}_{\mathrm{A}})} = \mathcal{Q}\left(\boldsymbol{n}_{\mathrm{S}}, \boldsymbol{n}_{\mathrm{A}}\right) / \left(\boldsymbol{n}_{\mathrm{S}}!\boldsymbol{n}_{\mathrm{A}}!\right) \ . \tag{6.1}$$

T (temperature) and V (volume) have their usual meanings, and we will suppress that notation on the right of 6.1. To further fix the notation we recall[125] $\mathcal{Q}(n_{\mathrm{A}} = 1) \equiv V q_{\mathrm{A}}^{(\mathrm{int})}/{\Lambda_{\mathrm{A}}}^3$ is the canonical ensemble partition function for a system comprising exactly one molecule of type A in a volume V with Λ_{A} is the thermal deBroglie

wavelength. The factorial notation

$$\boldsymbol{n}_{\mathrm{A}}! = n_{\mathrm{A}_1}! n_{\mathrm{A}_2}! \ldots \tag{6.2}$$

is common.[125,179] When convenient, we will denote $\boldsymbol{n} = \{\boldsymbol{n}_{\mathrm{S}}, \boldsymbol{n}_{\mathrm{A}}\}$ so that

$$\mathrm{e}^{-\beta A(T,V,\boldsymbol{n})} = \mathcal{Q}\left(\boldsymbol{n}\right)/\boldsymbol{n}! \ . \tag{6.3}$$

The grand canonical partition function will be central,

$$\mathrm{e}^{\beta p V} = \sum_{\boldsymbol{n} \geq 0} \mathcal{Q}\left(\boldsymbol{n}\right) \left(\frac{\boldsymbol{z}^{\boldsymbol{n}}}{\boldsymbol{n}!}\right) \ , \tag{6.4}$$

in these terms. Here we adopt a correspondingly simplified notation for the activities[125,179]

$$\boldsymbol{z}^{\boldsymbol{n}} = \exp\left\{\sum_{\mathrm{X}} \beta \mu_{\mathrm{X}} n_{\mathrm{X}}\right\} \tag{6.5}$$

with μ_{X} the chemical potential of species X. We will compare the pressure of the solution with the pressure of the solvent-only system at the same activity $z_{\mathrm{S}} = \mathrm{e}^{\beta \mu_{\mathrm{S}}}$:

$$\mathrm{e}^{\beta (p-\pi) V} = \sum_{\boldsymbol{n}_{\mathrm{S}} \geq 0} \mathcal{Q}\left(\boldsymbol{n}_{\mathrm{S}}, \boldsymbol{n}_{\mathrm{A}} = 0\right) \left(\frac{\boldsymbol{z}_{\mathrm{S}}{}^{\boldsymbol{n}_{\mathrm{S}}}}{\boldsymbol{n}_{\mathrm{S}}!}\right) \ . \tag{6.6}$$

The pressure difference π is the osmotic pressure. The probability for observing $\boldsymbol{n}_{\mathrm{S}}$ in the solvent-only system is

$$P\left(\boldsymbol{n}_{\mathrm{S}}; \boldsymbol{z}_{\mathrm{A}} = 0\right) = \mathcal{Q}\left(\boldsymbol{n}_{\mathrm{S}}, \boldsymbol{n}_{\mathrm{A}} = 0\right) \left(\frac{\boldsymbol{z}_{\mathrm{S}}{}^{\boldsymbol{n}_{\mathrm{S}}}}{\boldsymbol{n}_{\mathrm{S}}!}\right) \mathrm{e}^{-\beta (p-\pi) V} \ . \tag{6.7}$$

With these notations we write

$$\mathrm{e}^{\beta\pi V} = \sum_{\boldsymbol{n}_\mathrm{A}\geq 0}\left(\frac{\boldsymbol{z}_\mathrm{A}{}^{\boldsymbol{n}_\mathrm{A}}}{\boldsymbol{n}_\mathrm{A}!}\right)\sum_{\boldsymbol{n}_\mathrm{S}\geq 0}\left\{\frac{\mathcal{Q}\left(\boldsymbol{n}_\mathrm{S},\boldsymbol{n}_\mathrm{A}\right)}{\mathcal{Q}\left(\boldsymbol{n}_\mathrm{S},\boldsymbol{n}_\mathrm{A}=0\right)}\right\}P\left(\boldsymbol{n}_\mathrm{S};\boldsymbol{z}_\mathrm{A}=0\right) = \sum_{\boldsymbol{n}_\mathrm{A}\geq 0}\mathcal{Z}\left(\boldsymbol{n}_\mathrm{A};\boldsymbol{z}_\mathrm{S}\right)\left(\frac{\boldsymbol{z}_\mathrm{A}{}^{\boldsymbol{n}_\mathrm{A}}}{\boldsymbol{n}_\mathrm{A}!}\right) . \tag{6.8}$$

The important point is the structural similarity to 6.4.

Our task is to analyze the MM configurational integral

$$\mathcal{Z}\left(\boldsymbol{n}_\mathrm{A};\boldsymbol{z}_\mathrm{S}\right) = \sum_{\boldsymbol{n}_\mathrm{S}\geq 0}\left\{\frac{\mathcal{Q}\left(\boldsymbol{n}_\mathrm{S},\boldsymbol{n}_\mathrm{A}\right)}{\mathcal{Q}\left(\boldsymbol{n}_\mathrm{S},\boldsymbol{n}_\mathrm{A}=0\right)}\right\}P\left(\boldsymbol{n}_\mathrm{S};\boldsymbol{z}_\mathrm{A}=0\right) \tag{6.9}$$

The displayed ratio of partition functions is distinctive. For the case $\boldsymbol{n}_\mathrm{A} = 1$, for example, we write

$$\sum_{\boldsymbol{n}_\mathrm{S}\geq 0}\left\{\frac{\mathcal{Q}\left(\boldsymbol{n}_\mathrm{S},\boldsymbol{n}_\mathrm{A}=1\right)}{\mathcal{Q}\left(\boldsymbol{n}_\mathrm{S},\boldsymbol{n}_\mathrm{A}=0\right)}\right\}P\left(\boldsymbol{n}_\mathrm{S};\boldsymbol{z}_\mathrm{A}=0\right) = \mathcal{Q}\left(\boldsymbol{n}_\mathrm{S}=0,\boldsymbol{n}_\mathrm{A}=1\right)\left\langle\left\langle \mathrm{e}^{-\beta\Delta U_\mathrm{A}^{(1)}}\right\rangle\right\rangle_0 , \tag{6.10}$$

where the right-most factor is to be evaluated at infinite dilution of the solute, $\boldsymbol{z}_\mathrm{A} = 0$. The potential distribution development establishes that right-side to be[125]

$$\mathcal{Q}\left(\boldsymbol{n}_\mathrm{S}=0,\boldsymbol{n}_\mathrm{A}=1\right)\left\langle\left\langle \mathrm{e}^{-\beta\Delta U_\mathrm{A}^{(1)}}\right\rangle\right\rangle_0 = \lim_{z_A\to 0}\left(\frac{n_\mathrm{A}}{z_A}\right) = \lim_{z_A\to 0}\left(\frac{\rho_\mathrm{A}}{z_A}\right)V . \tag{6.11}$$

To write the general term for 6.9, we will use

$$\binom{\boldsymbol{n}_\mathrm{A}}{\boldsymbol{m}_\mathrm{A}}$$

to denote the number of ways of selecting the $\boldsymbol{m}_\mathrm{A}$ solute molecule set from the collection $\boldsymbol{n}_\mathrm{A}$. For example, if only one type of solute A is considered, then

$$\binom{\boldsymbol{n}_\mathrm{A}}{\boldsymbol{m}_\mathrm{A}} = \frac{n_\mathrm{A}!}{m_\mathrm{A}!\left(n_\mathrm{A}-m_\mathrm{A}\right)!} = \frac{n_\mathrm{A}^{\underline{m}_\mathrm{A}}}{m_\mathrm{A}!} , \tag{6.12}$$

as usual, with the last equality using the 'n_{A}-to-the-m_{A}-falling' notation.[125,182]

For more general but specified $\boldsymbol{m}_{\mathrm{A}}$, we rewrite 6.9

$$\sum_{\boldsymbol{n}_{\mathrm{S}}\geq 0}\left\{\frac{\mathcal{Q}\left(\boldsymbol{n}_{\mathrm{S}},\boldsymbol{m}_{\mathrm{A}}\right)}{\mathcal{Q}\left(\boldsymbol{n}_{\mathrm{S}},\boldsymbol{m}_{\mathrm{A}}=0\right)}\right\}P\left(\boldsymbol{n}_{\mathrm{S}};\boldsymbol{z}_{\mathrm{A}}=0\right)=\mathcal{Q}\left(\boldsymbol{n}_{\mathrm{S}}=0,\boldsymbol{m}_{\mathrm{A}}\right)\left\langle\left\langle \mathrm{e}^{-\beta\Delta U^{(\boldsymbol{m}_{\mathrm{A}})}}\right\rangle\right\rangle_{0} \tag{6.13}$$

and again, after having set $\boldsymbol{m}_{\mathrm{A}}$, this is to be evaluated at infinite dilution. Here the binding energy

$$\Delta U^{(\boldsymbol{m}_{\mathrm{A}})}=U\left(\boldsymbol{n}_{\mathrm{S}},\boldsymbol{m}_{\mathrm{A}}\right)-U\left(\boldsymbol{n}_{\mathrm{S}},\boldsymbol{m}_{\mathrm{A}}=0\right)-U\left(\boldsymbol{n}_{\mathrm{S}}=0,\boldsymbol{m}_{\mathrm{A}}\right)\ , \tag{6.14}$$

is associated with the collection of $\boldsymbol{m}_{\mathrm{A}}$ solute molecules. Following the potential distribution theory further[125]

$$\mathcal{Q}\left(\boldsymbol{n}_{\mathrm{S}}=0,\boldsymbol{m}_{\mathrm{A}}\right)\left\langle\left\langle \mathrm{e}^{-\beta\Delta U^{(\boldsymbol{m}_{\mathrm{A}})}}\right\rangle\right\rangle_{0}=\left\langle\binom{\boldsymbol{n}_{\mathrm{A}}}{\boldsymbol{m}_{\mathrm{A}}}\right\rangle\frac{\boldsymbol{m}_{\mathrm{A}}!}{\boldsymbol{z}_{\mathrm{A}}{}^{\boldsymbol{m}_{\mathrm{A}}}}\ , \tag{6.15}$$

Finally,

$$\left\langle\binom{\boldsymbol{n}_{\mathrm{A}}}{\boldsymbol{m}_{\mathrm{A}}}\right\rangle\boldsymbol{m}_{\mathrm{A}}!=\boldsymbol{\rho}_{\mathrm{A}}{}^{\boldsymbol{m}_{\mathrm{A}}}\int_{V}\mathrm{d}1_{\mathrm{A}}\ldots\int_{V}\mathrm{d}m_{\mathrm{A}}g^{(\boldsymbol{m}_{\mathrm{A}})}\left(1_{\mathrm{A}}\ldots m_{\mathrm{A}}\right)\ , \tag{6.16}$$

with $g^{(\boldsymbol{m}_{\mathrm{A}})}\left(1_{\mathrm{A}}\ldots m_{\mathrm{A}}\right)$ denoting the usual $\boldsymbol{m}_{\mathrm{A}}$ joint distribution function. Here we denote solute configurational coordinates as $(1_{\mathrm{A}},\ldots m_{\mathrm{A}})$, and the necessary integrations by $\int_{V}\mathrm{d}1_{\mathrm{A}}\ldots\int_{V}\mathrm{d}m_{\mathrm{A}}$. This produces the factor of V in 6.11. Since we wish to simplify 6.13, with $\boldsymbol{z}_{\mathrm{A}}=0$, we use 6.15 to write

$$\mathcal{Z}\left(\boldsymbol{n}_{\mathrm{A}};\boldsymbol{z}_{\mathrm{S}}\right)=\left[\lim_{\boldsymbol{z}_{\mathrm{A}}\to 0}\left(\frac{\boldsymbol{\rho}_{\mathrm{A}}}{\boldsymbol{z}_{\mathrm{A}}}\right)\right]^{\boldsymbol{n}_{\mathrm{A}}}\int_{V}\mathrm{d}1_{\mathrm{A}}\ldots\int_{V}\mathrm{d}n_{\mathrm{A}}g^{(\boldsymbol{n}_{\mathrm{A}})}\left(1_{\mathrm{A}}\ldots n_{\mathrm{A}};\boldsymbol{z}_{\mathrm{A}}=0\right) \tag{6.17}$$

The prefactor, to be evaluated at infinite dilution, is given by

$$\frac{\rho_{\mathrm{A}}}{z_{\mathrm{A}}} = \frac{q_{\mathrm{A}}^{\mathrm{int}}}{\Lambda_{\mathrm{A}}^{3}} \left\langle \left\langle \mathrm{e}^{-\beta \Delta U_{\mathrm{A}}^{(1)}} \right\rangle \right\rangle_{0} \tag{6.18}$$

in the potential distribution theorem formulation.[125]

With this suggestive form we can be more specific about the canonical configurational integrals that started our discussion, specifically

$$\mathcal{Q}\left(\boldsymbol{n}_{\mathrm{A}}\right) = \lim_{\boldsymbol{z}_{\mathrm{S}} \to 0} \mathcal{Z}\left(\boldsymbol{n}_{\mathrm{A}}; \boldsymbol{z}_{\mathrm{S}}\right) = \lim_{\boldsymbol{z}_{\mathrm{S}} \to 0} \left[\lim_{\boldsymbol{z}_{\mathrm{A}} \to 0} \left(\frac{\rho_{\mathrm{A}}}{z_{\mathrm{A}}} \right) \right]^{\boldsymbol{n}_{\mathrm{A}}} \int_{V} \mathrm{d}1_{\mathrm{A}} \ldots \int_{V} \mathrm{d}n_{\mathrm{A}} \mathrm{e}^{-\beta W(1_{\mathrm{A}} \ldots n_{\mathrm{A}})} \ . \tag{6.19}$$

The multipliers appearing on the middle line supply features of the kinetic energy portion of the partition function, specific to the implementation for the particular case. For notational simplicity we will drop the specific identification of the solvent activity in the formulae elsewhere.

These formulae, particularly 6.19, are collected in the summary statement of MM theory in 5.2.1, and particularly with 5.2.

B: Potential Distribution Theory

With the MM background, we evaluate the average number of solute A molecules as

$$\langle n_{\mathrm{A}} \rangle = \mathrm{e}^{-\beta \pi V} \sum_{\boldsymbol{n}_{\mathrm{A}} \geq 0} n_{\mathrm{A}} \mathcal{Z}\left(\boldsymbol{n}_{\mathrm{A}}; \boldsymbol{z}_{\mathrm{S}}\right) \left(\frac{\boldsymbol{z}_{\mathrm{A}}{}^{\boldsymbol{n}_{\mathrm{A}}}}{\boldsymbol{n}_{\mathrm{A}}!} \right) \ . \tag{B-1}$$

Since the summand factor n_{A} annuls the $n_{\mathrm{A}} = 0$ term, this result presents an explicit leading factor of z_{A}. Determination of z_{A} establishes the thermodynamic property μ_{A}. Therefore, we rewrite this equation by bringing forward the explicit extra factor of z_{A} as

$$\langle n_{\mathrm{A}} \rangle = e^{-\beta\pi V} \mathcal{Z}\left(\boldsymbol{n}_{\mathrm{A}} = 1; \boldsymbol{z}_{\mathrm{S}}\right) z_{\mathrm{A}} \sum_{\boldsymbol{n}_{\mathrm{A}} \geq 0} \left(\frac{\mathcal{Z}\left(\boldsymbol{n}_{\mathrm{A}} + 1; \boldsymbol{z}_{\mathrm{S}}\right)}{\mathcal{Z}\left(\boldsymbol{n}_{\mathrm{A}} = 1; \boldsymbol{z}_{\mathrm{S}}\right) \mathcal{Z}\left(\boldsymbol{n}_{\mathrm{A}}; \boldsymbol{z}_{\mathrm{S}}\right)} \right) \mathcal{Z}\left(\boldsymbol{n}_{\mathrm{A}}; \boldsymbol{z}_{\mathrm{S}}\right) \left(\frac{{\boldsymbol{z}_{\mathrm{A}}}^{\boldsymbol{n}_{\mathrm{A}}}}{\boldsymbol{n}_{\mathrm{A}}!} \right) \quad \text{(B-2)}$$

or

$$\langle n_{\mathrm{A}} \rangle = \mathcal{Z}\left(\boldsymbol{n}_{\mathrm{A}} = 1; \boldsymbol{z}_{\mathrm{S}}\right) z_{\mathrm{A}} \left\langle \left\langle \mathrm{e}^{-\beta \Delta W_{\mathrm{A}}^{(1)}} \right\rangle \right\rangle_0 \ . \quad \text{(B-3)}$$

Here

$$\Delta W_{\mathrm{A}}^{(1)} = W\left(\boldsymbol{n}_A + 1\right) - W\left(\boldsymbol{n}_A\right) - W\left(1\right) \ , \quad \text{(B-4)}$$

is the binding energy of a distinguished solute (A) molecule in the MM system, and the quantity

$$\mathcal{Z}\left(\boldsymbol{n}_{\mathrm{A}} = 1; \boldsymbol{z}_{\mathrm{S}}\right) = \frac{V q_{\mathrm{A}}^{(\mathrm{int})}}{{\Lambda_{\mathrm{A}}}^3} \left\langle \left\langle \mathrm{e}^{-\beta \Delta U_{\mathrm{A}}^{(1)}} \right\rangle \right\rangle_0 \quad \text{(B-5)}$$

involves interactions of one A molecule and the solvent; it is proportional to the system volume.

C: QCT breakup in the grand canonical ensemble

Here we discuss twists associated with the consideration of PDT developments when n_{A} fluctuates. We begin with the observation from B-3 that

$$\left\langle \left\langle \mathrm{e}^{-\beta \Delta W_{\mathrm{A}}^{(1)}} \right\rangle \right\rangle_0 \propto \langle n_{\mathrm{A}} \rangle \ . \quad \text{(C-1)}$$

Then considering the ratio

$$\frac{\left\langle\left\langle \mathrm{e}^{-\beta\Delta W_{\mathrm{A}}^{(1)}} F \right\rangle\right\rangle_0}{\left\langle\left\langle \mathrm{e}^{-\beta\Delta W_{\mathrm{A}}^{(1)}} \right\rangle\right\rangle_0} = \frac{\langle F n_{\mathrm{A}} \rangle}{\langle n_{\mathrm{A}} \rangle} \ , \tag{C-2}$$

yields a particularly transparent result. Choosing $F = \mathrm{e}^{\beta\Delta W_{\mathrm{A}}^{(1)}} \chi_{\mathrm{A}}$, we obtain an analogue of Eq 5.8:

$$\frac{\left\langle \mathrm{e}^{\beta\Delta W_{\mathrm{A}}^{(1)}} \chi_{\mathrm{A}} n_{\mathrm{A}} \right\rangle}{\langle n_{\mathrm{A}} \rangle} = \frac{\langle\langle \chi_{\mathrm{A}} \rangle\rangle_0}{\left\langle\left\langle \mathrm{e}^{-\beta\Delta W_{\mathrm{A}}^{(1)}} \right\rangle\right\rangle_0} \ . \tag{C-3}$$

If the averages are canonical then this is just Eq 5.8 again, but C-3 remains true if n_{A} fluctuates.

We expect that

$$\frac{\left\langle \mathrm{e}^{\beta\Delta W_{\mathrm{A}}^{(1)}} \chi_{\mathrm{A}} n_{\mathrm{A}} \right\rangle}{\langle n_{\mathrm{A}} \rangle} \sim \left\langle \mathrm{e}^{\beta\Delta W_{\mathrm{A}}^{(1)}} \chi_{\mathrm{A}} \right\rangle + O(\langle n_{\mathrm{A}} \rangle^{-1}) \ , \tag{C-4}$$

so in the thermodynamic limit that average matches the simpler canonical expression. The physical reason for this expectation is that we can write $n_{\mathrm{A}} = \langle n_{\mathrm{A}} \rangle + \delta n_{\mathrm{A}}$ in the numerator. Then the correlation of δn_{A} with the intensive characteristic of that numerator average should yield an intensive result.

Accepting this argument for the moment and retaining only the dominant contribution in C-4, we recover the results of 5.2.3 — and specifically the important result 5.11 — but consistently with the grand canonical ensemble derivation of the earlier sections.

To make that physical view specific, we introduce the additional notation

$$\left\langle \mathrm{e}^{\beta\Delta W_{\mathrm{A}}^{(1)}} | n_{\mathrm{A}} \right\rangle$$

for the canonical ensemble average that specifies n_{A}. For anticipated δn_{A}, we use

$$\left\langle \mathrm{e}^{\beta\Delta W^{(1)}}\chi_{\mathrm{A}}|n_{\mathrm{A}}\right\rangle \approx \left\langle \mathrm{e}^{\beta\Delta W_{\mathrm{A}}^{(1)}}\chi_{\mathrm{A}}|\left\langle n_{\mathrm{A}}\right\rangle\right\rangle + \delta n_{\mathrm{A}}\left(\frac{\partial\left\langle \mathrm{e}^{\beta\Delta W_{\mathrm{A}}^{(1)}}\chi_{\mathrm{A}}|\left\langle n_{\mathrm{A}}\right\rangle\right\rangle}{\partial\left\langle n_{\mathrm{A}}\right\rangle}\right) . \quad \text{(C-5)}$$

Used in the left-side of C-4, and then averaging with respect to n_{A} occupancies, this yields

$$\frac{\left\langle \mathrm{e}^{\beta\Delta W_{\mathrm{A}}^{(1)}}\chi_{\mathrm{A}}n_{\mathrm{A}}\right\rangle}{\left\langle n_{\mathrm{A}}\right\rangle} \approx \left\langle \mathrm{e}^{\beta\Delta W_{\mathrm{A}}^{(1)}}\chi_{\mathrm{A}}|\left\langle n_{\mathrm{A}}\right\rangle\right\rangle + \frac{\left\langle \delta n_{\mathrm{A}}{}^{2}\right\rangle}{\left\langle n_{\mathrm{A}}\right\rangle}\left(\frac{\partial\left\langle \mathrm{e}^{\beta\Delta W_{\mathrm{A}}^{(1)}}\chi_{\mathrm{A}}|\left\langle n_{\mathrm{A}}\right\rangle\right\rangle}{\partial\left\langle n_{\mathrm{A}}\right\rangle}\right) , \quad \text{(C-6)}$$

the expected result. Since

$$\left\langle \delta n_{\mathrm{A}}{}^{2}\right\rangle = \left(\frac{\partial\left\langle n_{\mathrm{A}}\right\rangle}{\partial\beta\mu_{\mathrm{A}}}\right)_{T,V,\mu_{\mathrm{S}}} ,$$

the correction indeed vanishes in the thermodynamic limit.

D: Intermolecular radial distribution functions between heavy atoms in PC

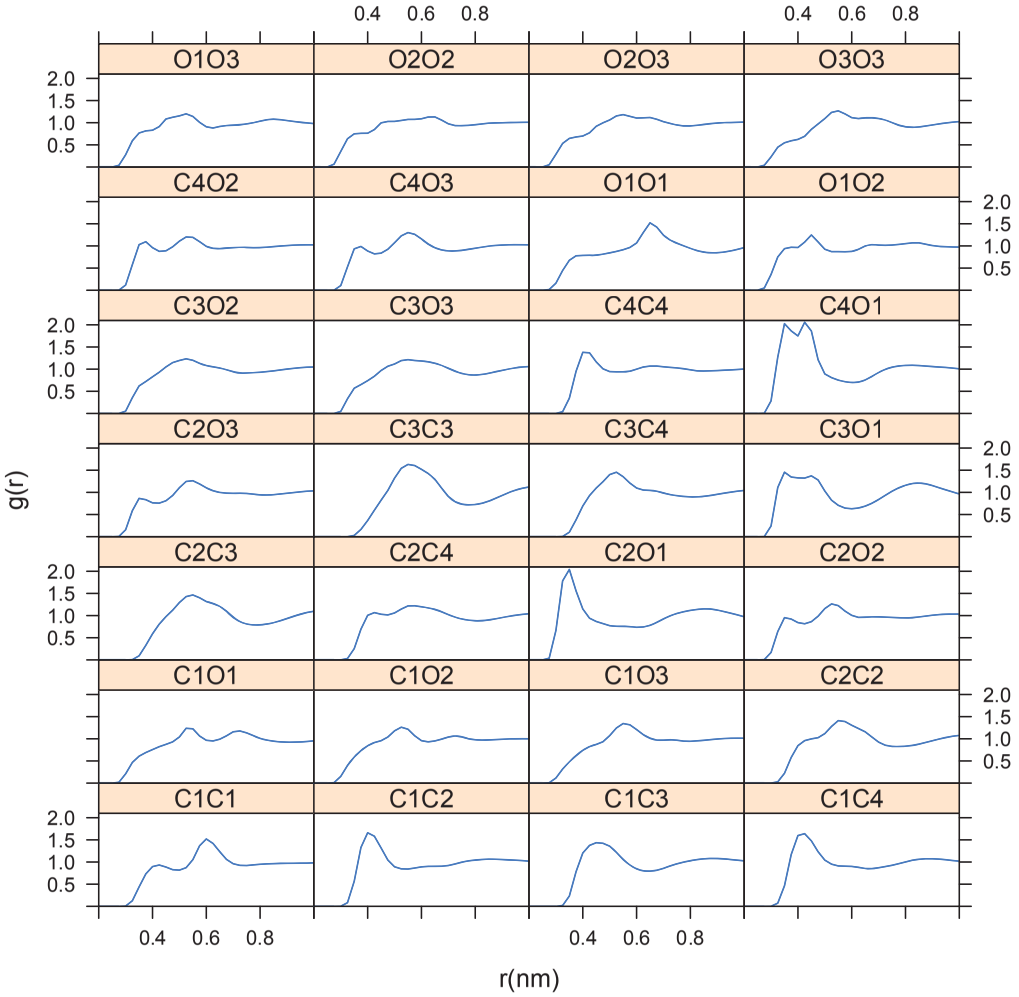

Figure 6.1: Radial distribution function between heavy atoms in PC at 300K.

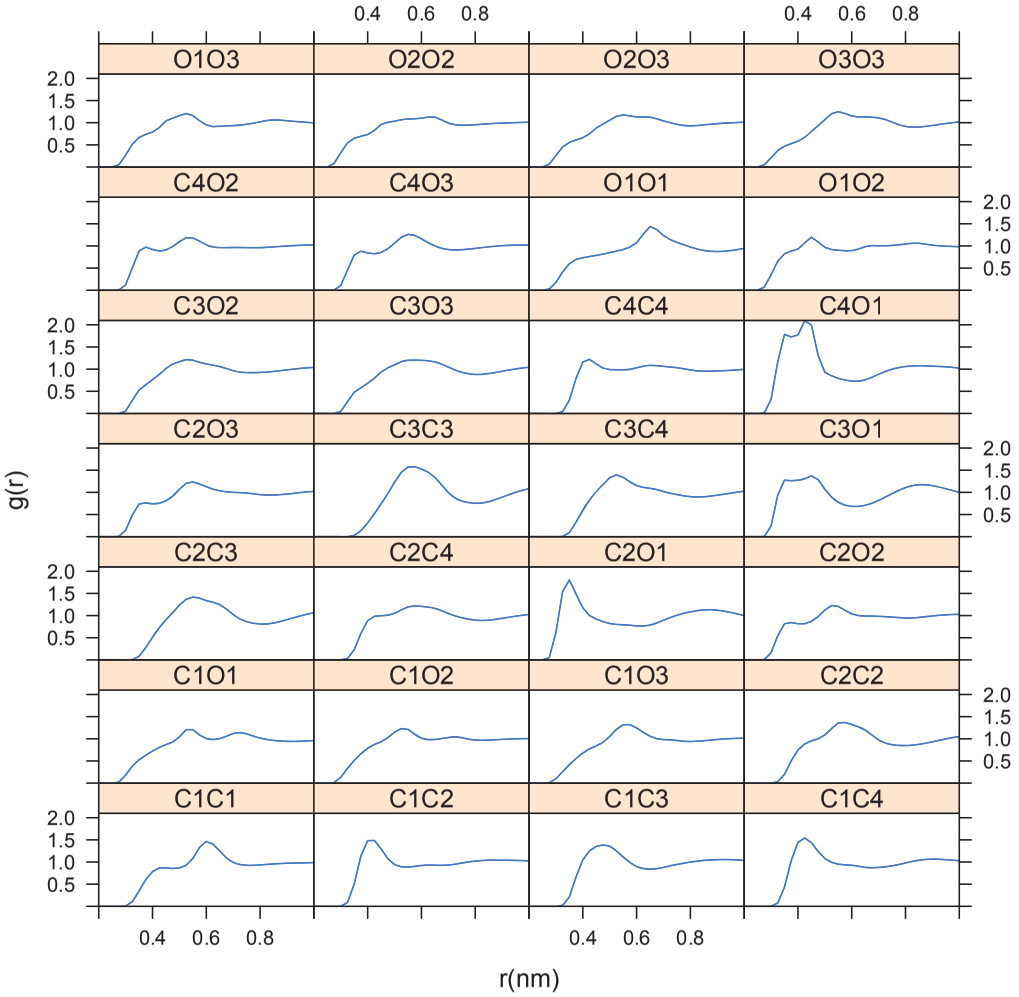

Figure 6.2: Radial distribution function between heavy atoms in PC at 400K.

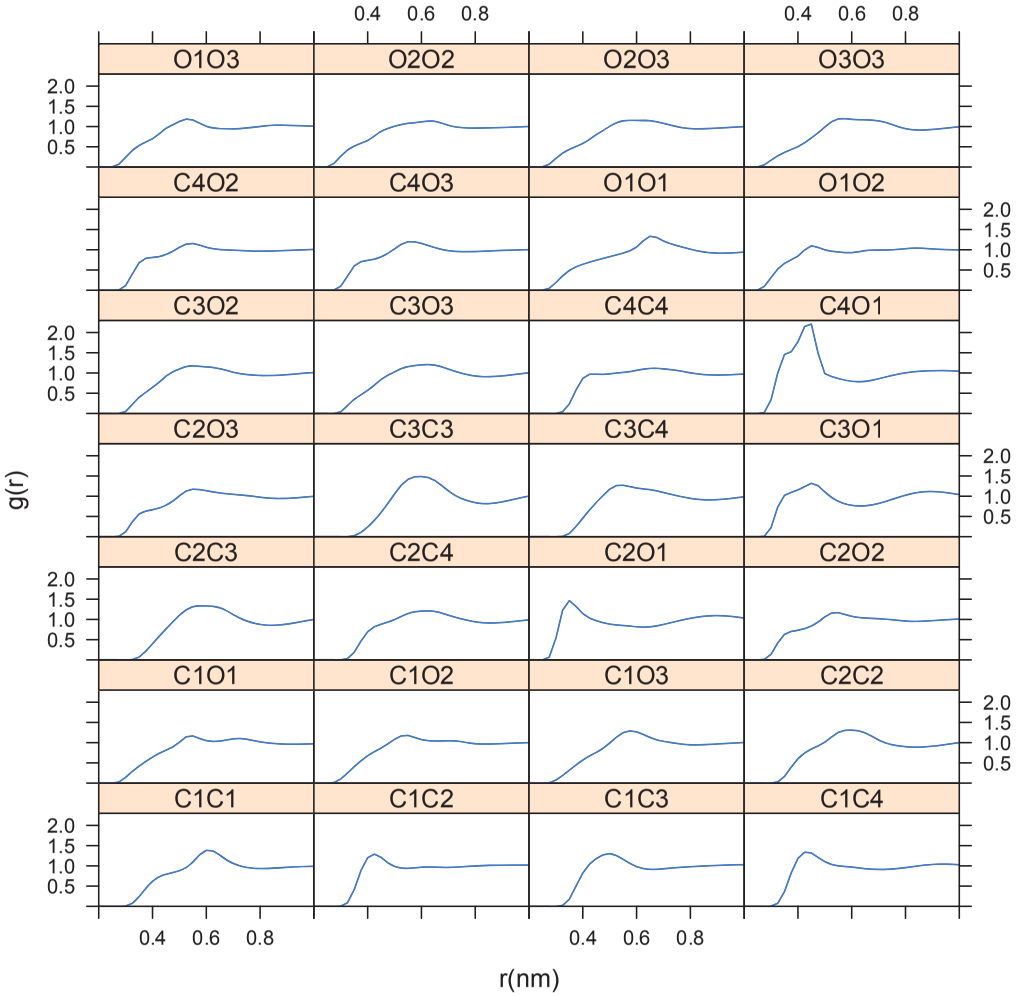

Figure 6.3: Radial distribution function between heavy atoms in PC at 600K.

E: Memory kernel from generalized Langevin equation

The generalized Langevin equation described the motion of a fluid particle itself rather than a Brownian particle dissolved in the fluid.[183] Compared to the simple Langevin equation,

$$m\frac{\mathrm{d}v(t)}{\mathrm{d}t} = -\xi m v(t) + R(t) \ , \tag{C-7}$$

the generalized form introduced a memory function, $\gamma(t)$, which implies that the frictional force acting at a given time reflects the pervious history of the system.[184]

$$m\frac{\mathrm{d}v(t)}{\mathrm{d}t} = -m\int_0^t \gamma(t-\tau)v(\tau)\mathrm{d}\tau + R(t) \ , \tag{C-8}$$

where m is the mass of the particle, $R(t)$ is the random fluctuating force, arises from collisions with the surrounding molecules. The random force is assumed to

- vanish in the mean, $\langle R(t)\rangle = 0$
- be uncorrelated with the velocity, $\langle R(t)\cdot v(0)\rangle = 0$
- have a infinitely short correlation time, $\langle R(t+s)\cdot R(s)\rangle = 2\pi R_0\delta(t)$, where R_0, the power spectrum of the random force is a constant.

And the relationship between memory function and velocity autocorrelation function is arrived[183–185] as

$$m\frac{\mathrm{d}C(t)}{\mathrm{d}t} = -\int_0^t \gamma(t-\tau)C(\tau)\mathrm{d}\tau \ , \tag{C-9}$$

Based on Eq. C-9, we have

$$\left(\frac{\mathrm{d}C(t)}{\mathrm{d}t} - \frac{1}{m}\int_0^t \gamma(t-\tau)C(\tau)\mathrm{d}\tau\right)^2 = 0 \ . \tag{C-10}$$

We obtain $\gamma(t)$ by minimizing the left side of Eq. C-10, after discretization. Let $\gamma_{\mathrm{m}}(t) = \gamma(t)/m$,

$$\gamma_{\mathrm{m}}(\Delta t) = -\frac{\mathrm{d}^2C(\Delta t)}{\mathrm{d}t^2} - \frac{\Delta t}{2}\left\{\gamma_{\mathrm{m}}(\Delta t)\frac{\mathrm{d}C(0)}{\mathrm{d}t} + \gamma_{\mathrm{m}}(0)\frac{\mathrm{d}C(\Delta t)}{\mathrm{d}t}\right\} \ , \tag{C-11a}$$

$$\begin{aligned}\gamma_{\mathrm{m}}(n\Delta t) = &-\frac{\mathrm{d}^2C(\Delta t)}{\mathrm{d}t^2} \\ &- \Delta t\sum_{k=0}^{n-1}\gamma_{\mathrm{m}}(k\Delta t)\frac{\mathrm{d}C((n-k)\Delta t)}{\mathrm{d}t} \\ &+ \frac{\Delta t}{2}\left\{\gamma_{\mathrm{m}}(n\Delta t)\frac{\mathrm{d}C(0)}{\mathrm{d}t} + \gamma_{\mathrm{m}}(0)\frac{\mathrm{d}C(n\Delta t)}{\mathrm{d}t}\right\} \ .\end{aligned} \tag{C-11b}$$

With $C(0) = 1$ and $\frac{\mathrm{d}C(0)}{\mathrm{d}t} = 0$, Eq. C-11 can be simplified to

$$\gamma_{\mathrm{m}}(\Delta t) = -\frac{\mathrm{d}^2C(\Delta t)}{\mathrm{d}t^2} - \frac{\gamma_{\mathrm{m}}(0)\Delta t}{2}\frac{\mathrm{d}C(\Delta t)}{\mathrm{d}t} \ , \tag{C-12a}$$

$$\gamma_{\mathrm{m}}(n\Delta t) = -\frac{\mathrm{d}^2C(\Delta t)}{\mathrm{d}t^2} - \Delta t\sum_{k=0}^{n-1}\gamma_{\mathrm{m}}(k\Delta t)\frac{\mathrm{d}C((n-k)\Delta t)}{\mathrm{d}t} + \frac{\gamma_{\mathrm{m}}(0)\Delta t}{2}\frac{\mathrm{d}C(n\Delta t)}{\mathrm{d}t} \ . \tag{C-12b}$$

We also utilized a specialized Fourier transform method to extract $\gamma(t)$ from $C(t)$ on the basis of the one-sided Fourier (Laplace) transform:

$$\tilde{C}(z) = \int_0^\infty e^{izt}C(t)\mathrm{d}t \ , \tag{C-13}$$

where $z = \omega + i\epsilon$, assuming z is a real number and in the upper half plane, $z = \omega > 0$, which followed by

$$\tilde{C}(\omega) = \int_0^\infty \cos\omega t C(t)\mathrm{d}t + i\int_0^\infty \sin\omega t C(t)\mathrm{d}t \tag{C-14a}$$

$$= C'(\omega) + iC''(\omega) \tag{C-14b}$$

Similarly,

$$\tilde{\gamma}_\mathrm{m}(\omega) = \tilde{\gamma}'_\mathrm{m}(\omega) + i\tilde{\gamma}''_\mathrm{m}(\omega)\ . \tag{C-15}$$

Recall from Eq. C-9,

$$\frac{\mathrm{d}C(t)}{\mathrm{d}t} = -\int_0^t \gamma_\mathrm{m}(t-\tau)C(\tau)\mathrm{d}\tau\ . \tag{C-16}$$

The one-sided Fourier transform of both sides of Eq. C-16 results in

$$\int_0^\infty e^{i\omega t}\frac{\mathrm{d}C(t)}{\mathrm{d}t}\mathrm{d}t = -C(0) - it\int_0^\infty e^{i\omega t}C(t)\mathrm{d}t \tag{C-17a}$$

$$= -C(0) - it\tilde{C}(\omega)\ , \tag{C-17b}$$

and

$$\int_0^\infty e^{i\omega t}\left(\int_0^t \gamma_\mathrm{m}(t-\tau)C(\tau)\mathrm{d}\tau\right)\mathrm{d}t = \int_0^\infty e^{i\omega\tau}C(\tau)\mathrm{d}\tau\int_\tau^\infty e^{i\omega(t-\tau)}\gamma_\mathrm{m}(t-\tau)\mathrm{d}\tau \tag{C-18a}$$

$$= \tilde{C}(\omega)\tilde{\gamma}_\mathrm{m}(\omega)\ . \tag{C-18b}$$

We combined Eq. C-17 and Eq. C-18, then substituted $\tilde{C}(\omega)$ and $\tilde{\gamma}_{\mathrm{m}}(\omega)$ with $(C'(\omega)+iC''(\omega))$ and $(\tilde{\gamma}'_{\mathrm{m}}(\omega)+i\tilde{\gamma}''_{\mathrm{m}}(\omega))$, respectively (Eq.C-14, C-15):

$$\tilde{C}(\omega)=\frac{-iC(0)}{\omega-i\tilde{\gamma}_{\mathrm{m}}(\omega)}=C'(\omega)+iC''(\omega)=\frac{C(0)}{\gamma'_{\mathrm{m}}(\omega)+i(\omega+\gamma''_{\mathrm{m}}(\omega))}\ , \tag{C-19}$$

given $C(0)=1$ and solved for $C'(\omega)$ and $C''(\omega)$, we reached

$$C'(\omega)=\frac{\gamma'_{\mathrm{m}}(\omega)}{\gamma'_{\mathrm{m}}(\omega)^2+(\omega+\gamma''_{\mathrm{m}}(\omega))^2} \tag{C-20a}$$

$$C''(\omega)=\frac{-(\omega+\gamma''_{\mathrm{m}}(\omega))}{\gamma'_{\mathrm{m}}(\omega)^2+(\omega+\gamma''_{\mathrm{m}}(\omega))^2}\ , \tag{C-20b}$$

$$\frac{C''(\omega)}{C'(\omega)}=\frac{-(\omega+\gamma''_{\mathrm{m}}(\omega))}{\gamma'_{\mathrm{m}}(\omega)}\ . \tag{C-21}$$

$C'(\omega)$ can be expressed as

$$C'(\omega)=\frac{\gamma'_{\mathrm{m}}(\omega)}{\gamma'_{\mathrm{m}}(\omega)^2\left(1+(C''(\omega)/C'(\omega))^2\right)}\ , \tag{C-22}$$

that produced

$$\gamma'_{\mathrm{m}}(\omega)=\frac{C'(\omega)}{C'(\omega)^2+C''(\omega)^2}\ . \tag{C-23}$$

List of References

[1] A. C. Dillon, Chem. Rev., vol. 110, pp. 6856–6872, 2010.

[2] P. Simon and Y. Gogotsi, Nature Mater., vol. 7, p. 845, 2008.

[3] P. Sharma and T. S. Bhatti, Energy. Convers. Manage., vol. 51, p. 2901, 2010.

[4] M. Carlen and R. Ktz, Electrochim. Acta, vol. 45, p. 2483, 2000.

[5] C. Niu, E. K. Sichel, R. Hoch, D. Moy, and H. Tennent, Appl. Phys. Lett., vol. 70, p. 1480, 1997.

[6] K. H. An, W. S. Kim, J. M. Moon, D. J. Bae, S. C. Lim, Y. S. Lee, and Y. H. Lee, Adv. Funct. Mater., vol. 11, p. 387, 2001.

[7] B. J. Yoon, S. H. Jeong, K. H. Lee, H. S. Kim, C. G. Park, and J. H. Han, Chem. Phys. Lett., vol. 388, p. 170, 2004.

[8] D. Chunsheng, Y. Jeff, and P. Ning, Nanotechnology, vol. 16, p. 350, 2005.

[9] A. Kumar, V. L. Pushparaj, S. Kar, O. Nalamasu, P. M. Ajayan, and R. Baskaran, Appl. Phys. Lett., vol. 89, p. 163120, 2006.

[10] D. N. Futaba, Nature Mater., vol. 5, p. 987, 2006.

[11] C. Largeot, C. Portet, J. Chmiola, Y. Taberna, P Land Gogotsi, and P. Simon, J. Am. Chem. Soc., vol. 130, p. 2730, 2008.

[12] J. Huang, B. G. Sumpter, and V. Meunier, Angew. Chem. Int. Ed., vol. 47, p. 520, 2008.

[13] L. Yang, B. H. Fishbine, A. Migliori, and L. R. Pratt, J. Am. Chem. Soc., vol. 131, p. 12373, 2009.

[14] Y. Shim and H. J. Kim, ACS Nano, vol. 4, p. 2345, 2010.

[15] G. Feng, R. Qiao, J. Huang, S. Dai, B. G. Sumpter, and V. Meunier, Phys. Chem. Chem. Phys., vol. 13, pp. 1152–1161, 2010.

[16] M. S. Ding and T. R. Jow, Electroche. Soc., vol. 151, p. A2007, 2004.

[17] Z. B. Zhou, H. Matsumoto, and K. Tatsumi, Chemistry - A European Journal, vol. 11, p. 752, 2005.

[18] R. Kötz and M. Carlen, Electrochimica Acta, vol. 45, pp. 2483–2498, 2000.

[19] B. E. Conway, *Electrochemical Supercapacitors : Scientific Fundamentals and Technological Applications.* Kluwer-Plenum, 1999.

[20] A. Burke, J. Power Sources, vol. 91, pp. 37–50, 2000.

[21] G. Wang, L. Zhang, and J. Zhang, Chem. Soc. Rev., vol. 41, pp. 797–828, 2012.

[22] M. Armand, F. Endres, D. R. MacFarlane, H. Ohno, and B. Scrosati, Nature Mater., vol. 8, p. 621, 2009.

[23] P. Simon and Y. Gogotsi, Nat. Mater., vol. 7, pp. 845–854, 2008.

[24] E. Frackowiak and F. Béguin, Carbon, vol. 39, p. 937, 2001.

[25] P. W. Ruch, D. Cericola, A. Foelske, R. Tötz, and A. Wokaun, Electrochimica Acta, vol. 55, pp. 2352–2357, 2010.

[26] J. Chmiola, G. Yushin, Y. Gogotsi, C. Portet, P. Simon, , and P. L. Taberna, Science, vol. 313, pp. 1760–1763, 2006.

[27] P. W. Ruch, L. J. Hardwick, M. Hahn, A. Foelske, R. Kötz, and A. Wokaun, Carbon, vol. 47, pp. 38–52, 2009.

[28] T. A. Centeno and F. Stoeckli, Electrochem. Comm., vol. 16, pp. 34–36, 2012.

[29] P. Simon and Y. Gogotsi, Accts. Chem. Res., vol. 46, pp. 1094–1103, 2013.

[30] F. Stoeckli and T. A. Centeno, J. Mat. Chem. A, vol. 1, pp. 6865–6873, 2013.

[31] C. Merlet, M. Salanne, B. Rotenberg, and P. A. Madden, J. Phys. Chem. C, vol. 115, pp. 16 613–16 618, 2011.

[32] C. Merlet, B. Rotenberg, P. A. Madden, P.-L. Taberna, P. Simon, Y. Gogotsi, and M. Salanne, Nature Materials, vol. 11, pp. 306–310, 2012.

[33] C. Merlet, M. Salanne, B. Rotenberg, and P. A. Madden, Electrochim. Acta, vol. 101, pp. 262–271, 2013.

[34] G. Feng and P. T. Cummings, J. Phys. Chem. Letts., vol. 2, pp. 2859–2864, 2011.

[35] G. Feng, S. Li, V. Presser, and P. T. Cummings, J. Phys. Chem. Letts., vol. 4, pp. 3367–3376, 2013.

[36] D. Jiang, Z. Jin, and J. Wu, Nano Letts., vol. 11, pp. 5373–5377, 2011.

[37] D. Jiang and J. Wu, J. Phys. Chem. Letts., vol. 4, pp. 1260–1267, 2013.

[38] D. Jiang, Z. Jin, D. Henderson, and J. Wu, J. Phys. Chem. Letts., vol. 3, pp. 1727–1731, 2012.

[39] P. Wu, J. Huang, V. Meunier, B. G. Sumpter, and R. Qiao, ACS Nano, vol. 5, pp. 9044–9051, 2011.

[40] N. N. Rajput, J. Monk, R. Singh, and F. R. Hung, J. Phys. Chem. C, vol. 116, pp. 5170–5182, 2012.

[41] K. K. Mandadapu, J. A. Templeton, and J. W. Lee, J. Chem. Phys., vol. 139, 2013.

[42] J. W. Lee, J. A. Templeton, K. K. Mandadapu, and J. A. Zimmerman, J. Chem. Theory Comp., vol. 9, pp. 3051–3061, 2013.

[43] J. W. Lee, R. H. Nilson, J. A. Templeton, S. K. Griffiths, A. Kung, and B. M. Wong, J. Chem. Theory Comp., vol. 8, pp. 2012–2022, 2012.

[44] J. A. Templeton, R. E. Jones, J. W. Lee, J. A. Zimmerman, and B. M. Wong, J. Chem. Theory Comp., vol. 7, pp. 1736–1749, 2011.

[45] Z. Wang, Y. Yang, D. L. Olmsted, M. Asta, and B. B. Laird, J. Chem. Phys., vol. 141, p. 184102, 2014.

[46] H. Wang, J. Fang, and L. Pilon, Electrochimica Acta, vol. 109, pp. 316–321, 2013.

[47] H. Wang, A. Thiele, and L. Pilon, J. Phys. Chem. C, vol. 117, pp. 18 286–18 297, 2013.

[48] H. Wang and L. Pilon, J. Power Sources, vol. 221, pp. 252–260, 2013.

[49] H. Wang and L. Pilon, Electrochimica Acta, vol. 76, pp. 529–531, 2012.

[50] H. Wang and L. Pilon, Electrochimica Acta, vol. 64, pp. 130–139, 2012.

[51] H. Wang and L. Pilon, Electrochimica Acta, vol. 63, pp. 55–63, 2012.

[52] H. Wang and L. Pilon, J. Phys. Chem. C, vol. 115, pp. 16 711–16 719, 2011.

[53] H. Wang, J. Varghese, and L. Pilon, Electrochimica Acta, vol. 56, pp. 6189–6197, 2011.

[54] J. Varghese, H. Wang, and L. Pilon, J. Electrochem. Soc., vol. 158, pp. A1106–A1114, 2011.

[55] W. G. McMillan and J. E. Mayer, J. Chem. Phys., vol. 13, p. 276, 1945.

[56] H. L. Friedman and W. D. T. Dale, Modern Theoretical Chemistry, vol. 5, pp. 85–136, 1977.

[57] J. P. Simonin, J. Chem. Soc, Faraday Trans., vol. 92, pp. 3519–3523, 1996.

[58] H. L. Friedman, Ann. Rev. Phys. Chem., vol. 32, pp. 1798–204, 1981.

[59] G. Stell, Modern Theoretical Chemistry, vol. 5, pp. 47 – 84, 1977.

[60] D. Henderson, M. Holovko, and Trokhymchuk, Eds., *Ionic soft matter: modern trends in theory and applications*, 2005.

[61] P. Debye and E. Hückel, Physik. Zeits., vol. 24, pp. 179–207, 1923.

[62] S. A. Adelman, Chem. Phys. Letts., vol. 38, pp. 567–570, 1976.

[63] C. P. Ursenbach, W. D., and G. N. Patey, J. Chem. Phys., vol. 94, pp. 6782–6784, 1991.

[64] F. Hirata, *Molecular Theory of Solvation.* Dordrecht: Kluwer, 2003.

[65] D. Bowron, J. Finney, and A. Soper, J. Am. Chem. Soc, vol. 128, pp. 5119–5126, 2006.

[66] A. K. Soper, J. Phys.: Condens. Matter, vol. 19, p. 415108, 2007.

[67] L. R. Pratt, R. A. LaViolette, M. A. Gomez, and M. E. Gentile, J. Phys. Chem. B, vol. 105, pp. 11 662–11 668, 2001.

[68] M. E. Paulaitis and L. R. Pratt, Adv. Prot. Chem., vol. 62, pp. 283–310, 2002.

[69] T. L. Beck, M. E. Paulaitis, and L. R. Pratt, *The potential distribution theorem and models of molecular solutions.* Cambridge University Press, 2006.

[70] D. Asthagiri, L. R. Pratt, and M. E. Paulaitis, J. Chem. Phys., vol. 125, p. 024701, 2006.

[71] S. Chempath, L. R. Pratt, and M. E. Paulaitis, J. Chem. Phys., vol. 130, p. 054113, 2009.

[72] R. A. Robinson and R. H. Stokes, *Electrolyte Solutions*. Mineola, NY: Dover Publications Inc., 2002.

[73] T. R. Jow, K. Xu, and S. P. Ding, "Nonaqueous electrolyte development for electrochemical capacitors," U.S. Army Research Laboratory Adelphi, MD, Tech. Rep. DOE/ID/13451, 1999.

[74] L. Yang, B. H. Fishbine, A. Migliori, and L. R. Pratt, J. Am. Chem. Soc., vol. 131, pp. 12 373–12 376, 2009.

[75] L. Yang, B. H. Fishbine, A. Migliori, and L. R. Pratt, J. Chem. Phys., vol. 132, pp. 044 701(1–4), 2010.

[76] M. G. Martin. (2012) Mcccs towhee. http://towhee.sourceforge.net

[77] N. Bjerrum, Kgl. Dan. Vidensk. Selsk. Mat-fys. Medd., vol. 7, p. 1, 1926.

[78] R. M. Fuoss, Trans. Faraday Soc., vol. 30, pp. 967–980, 1934.

[79] R. Fowler and E. A. Guggenheim, *Statistical Thermodynamics*. Cambridge University Press, 1949, chapter IX.

[80] H. Reiss, J. Chem. Phys., vol. 25, pp. 400–407, 1956.

[81] H. L. Friedman, Ann. Rev. Phys. Chem., vol. 12, pp. 171–194, 1961.

[82] F. H. Stillinger Jr and R. Lovett, J. Chem. Phys., vol. 48, pp. 1–11, 1968.

[83] J. Given and G. Stell, J. Chem. Phys., vol. 106, pp. 1195–1209, 1997.

[84] P. Camp and G. N. Patey, J. Chem. Phys., vol. 111, pp. 9000–9008, 1999.

[85] P. J. Camp and G. N. Patey, Phys. Rev. E, vol. 60, pp. 1063–1066, 1999.

[86] T. Kaneko, J. Chem. Phys., vol. 123, p. 134509, 2005.

[87] R. M. Fuoss, PHYS CHEM CHEM PHYS, vol. 30, pp. 967–980, 1934.

[88] S. Chandrasekhar, REV MOD PHYS, vol. 15, pp. 1–89, 1943.

[89] S. Mazur, J CHEM PHYS, vol. 97, pp. 9276–9282, 1992.

[90] G. Hummer, S. Garde, A. E. García, A. Pohorille, and L. R. Pratt, P NATL ACAD SCI USA, vol. 93, pp. 8951–8955, 1996.

[91] L. R. Pratt, S. Garde, and G. Hummer, NATO Adv. Study Inst. Ser., Ser. C, vol. 529, p. 407, 1999.

[92] L. R. Pratt, ANNU REV PHYS CHEM, vol. 53, pp. 409–436, 2002.

[93] S. Chempath, B. R. Einsla, L. R. Pratt, C. S. Macomber, J. M. Boncella, J. A. Rau, and B. S. Pivovar, J PHYS CHEM C, vol. 112, pp. 3179–3182, 2008.

[94] S. Chempath, J. M. Boncella, L. R. Pratt, N. Henson, and B. S. Pivovar, J PHYS CHEM C, vol. 114, pp. 11 977–11 983, 2010.

[95] D. A. Case, T. A. Darden, I. T. E. Cheatham, C. L. Simmerling, J. Wang, R. E. Duke, R. Luo, K. M. Merz, D. A. Pearlman, M. Crowley, R. C. Walker, W. Zhang, B. Wang, S. Hayik, A. Roitberg, G. Seabra, K. F. Wong, F. Paesani, X. Wu, S. Brozell, V. Tsui, H. Gohlke, L. Yang, C. Tan, J. Mongan, V. Hornak, G. Cui, P. Beroza, D. H. Mathews, C. Schafmeister, W. S. Ross, , and P. A. Kollman, 2006.

[96] V. B. Luzhkov, F. Osterberg, P. Acharya, J. Chattopadhyaya, and J. Aqvist, PCCP, vol. 4, pp. 4640 – 4647, 2002.

[97] J. de Andrade, E. S. Boes, and H. Stassen, J. Phys. Chem. B, vol. 106, pp. 13 344 – 13 351, Dec 2002.

[98] J. M. Wang, R. M. Wolf, J. W. Caldwell, P. A. Kollman, and D. A. Case, J. Comp. Chem., vol. 25, pp. 1157 – 74, Jul 2004.

[99] L. Yang, B. H. Fishbine, A. Migliori, and L. R. Pratt, J. Chem. Phys., vol. 132, p. 044701, 2010.

[100] L. Yang, B. H. Fishbine, A. Migliori, and L. R. Pratt, J. Am. Chem. Soc, vol. 131, p. 12373, 2009.

[101] G. G. Hoffman, R. Mariano, N. Pesika, L. R. Pratt, S. W. Rick, and X. You, "Simulation of Propylene Carbonate as a Solvent for Electrochemical Double-layer Capacitors," Proceedings of Louisiana EPSCoR RII LA-SiGMA 2011 Symposium, Tech. Rep., 2011, proceedings of Louisiana EPSCoR RII LA-SiGMA 2011 Symposium.

[102] X. You, K. M. Aritakula, N. Pesika, L. R. Pratt, and S. W. Rick, "Simulation of Propylene Carbonate Solutions for Electrochemical Double-layer Capacitors," Proceedings of Louisiana EPSCoR RII LA-SiGMA 2012 Symposium, Tech. Rep., 2012, proceedings of Louisiana EPSCoR RII LA-SiGMA 2012 Symposium.

[103] S. Paul and A. Chandra, J. Phys. Chem. B, vol. 109, p. 20558, 2005.

[104] Z. Hu and J. D. Weeks, J. Phys. Chem. C, vol. 114, p. 10202, 2010.

[105] S. Liu, Z. Hu, J. D. Weeks, and J. T. Fourkas, J. Phys. Chem., vol. 116, p. 4012, 2012.

[106] J. C. Soetens, C. Millot, B. Maigret, and I. Bako, J. Mol. Liq., vol. 92, pp. 201–216, 2001.

[107] L. B. Silva and L. C. G. Freitas, J. Mol. Struct.-Theochem, vol. 806, Mar. 2007.

[108] F. Heslot, N. Fraysee, and A. M. Cazabat, Nature, vol. 338, pp. 640–642, 1989.

[109] P.-G. deGennes, F. Borchard-Wyart, and D. Quéré, *Capillarity and Wetting Phenomena*. Springer, 2004.

[110] R. Werder, J. H. Walther, R. L. Jaffe, T. Halicioglu, and P. Koumoutsakos, J. Phys. Chem. B, vol. 107, pp. 1345–1352, 2003.

[111] A. W. Adamson and A. P. Gast. Wiley, 1997, http://en.wikipedia.org/wiki/Surface-tension$_v aluescite_n ote - Phys_C hem_S urf - 1$.

[112] G. M. Wilson, D. M. Von Niederhausern, and N. F. Giles, J. Chem. & Eng. Data, vol. 47, pp. 761–764, 2002.

[113] P. Zhu, Y. You, L. R. Pratt, and K. D. Papadopoulos, J. Chem. Phys., vol. 134, p. 054502, Jan. 2011.

[114] C. J. Brown, Acta Cryst.], pp. 1–5, 1954.

[115] Y. Wu, H. L. Tepper, and G. A. Voth, J. Chem. Phys., vol. 124, p. 024503, Jan. 2006.

[116] J.-P. Côte, D. Brouillette, J. E. Desnoyers, J.-F. Rouleau, J.-M. St-Arnaud, and G. Perron, J. Soln. Chem., vol. 25, pp. 1163–1173, 1996.

[117] D. Asthagiri, P. D. Dixit, S. Merchant, M. E. Paulaitis, L. R. Pratt, S. B. Rempe, and S. Varma, Chem. Phys. Letts., vol. 485, pp. 1–7, 2010.

[118] S. Chempath, L. R. Pratt, and M. E. Paulaitis, J. Chem. Phys., vol. 130, pp. 054 113(1–5), 2009.

[119] S. Chempath and L. R. Pratt, J. Phys. Chem. B, vol. 113, pp. 4147–4151, 2009.

[120] D. M. Rogers, D. Jiao, L. R. Pratt, and S. B. Rempe, Ann. Rep. Comp. Chem., vol. 8, pp. 71–127, 2012.

[121] J. Shah, D. Asthagiri, L. Pratt, and M. Paulaitis, J. Chem. Phys., vol. 127, pp. 144 508 (1–7), 2007.

[122] V. Weber, S. Merchant, and D. Asthagiri, J. Chem. Phys., vol. 135, p. 181101, 2011.

[123] V. Weber and D. Asthagiri, J. Chem. Phys., vol. 133, p. 141101, 2010.

[124] V. Weber, S. Merchant, P. D. Dixit, and D. Asthagiri, J. Chem. Phys., vol. 132, p. 204509, 2010.

[125] T. L. Beck, M. E. Paulaitis, and L. R. Pratt, *THE POTENTIAL DISTRIBUTION THEOREM AND MODELS OF MOLECULAR SOLUTIONS*. Cambridge University Press, 2006.

[126] G. A. Bottomley and M. T. Bremers, Aust. J. Chem., vol. 39, pp. 1959–1981, 1986.

[127] Y. Marcus and G. T. Hefter, J. Mol. Liq., vol. 73, pp. 61–74, 1997.

[128] H. Piekarski, K. Kubalczyk, and M. Wasiak, J. Chem. Eng., vol. 55, p. 5435, 2010.

[129] B. Hess, C. Kutzner, D. van der Spoel, and E. Lindahl, J. Chem. Theory Comp., 2008.

[130] L. Martínez, R. Andrade, E. G. Birgin, and J. M. Martínez, J. Comp. Chem., vol. 30, pp. 2157–2164, Oct. 2009.

[131] S. Kumar, D. Bouzida, R. H. Swendsen, P. A. Kollman, and J. M. Rosenberg, J. Comp. Chem., vol. 13, pp. 1011–1021, 1992.

[132] A. Grossfield, "WHAM," University of Rochester Medical Center, Tech. Rep., 2010, http://membrane.urmc.rochester.edu/Software/WHAM/WHAM.html.

[133] B. Widom, Science, vol. 157, pp. 375–382, 1967.

[134] H. C. Andersen, D. Chandler, and J. D. Weeks, Adv. Chem. Phys., vol. 34, pp. 105–156, 1976.

[135] J. A. Barker and D. Henderson, Rev. Mod. Phys., vol. 48, p. 587, 1976.

[136] D. Chandler, J. D. Weeks, and H. C. Andersen, Science, vol. 220, pp. 787–794, 1983.

[137] J. L. Lebowitz and E. M. Waisman, Phys. Today, pp. 24–30, 1980.

[138] R. Zwanzig, Ann. Rev. Phys. Chem., vol. 16, pp. 67–102, 1965.

[139] P. Resibois, J. Piasecki, and Y. Pomeau, Phys. Rev. Letts., vol. 28, pp. 882–885, 1972.

[140] M. Seghers, P. Resibois, and Y. Pomeau, Phys. Letts., vol. 53A, pp. 353–354, 1975.

[141] L. Verlet, Phys. Rev., vol. 159, pp. 98–103, Jul. 1967.

[142] J. Kushick and B. J. Berne, J. Chem. Phys., vol. 59, p. 3732, 1973.

[143] B. J. Alder, D. M. Gass, and T. E. Wainwright, J. Chem. Phys., vol. 53, p. 3813, 1970.

[144] D. M. Heyes and J. G. Powles, Mol. Phys., vol. 95, pp. 259–267, Oct. 1998.

[145] D. M. Heyes, J. G. Powles, and G. Rickayzen, Mol. Phys., vol. 100, pp. 595–610, Mar. 2002.

[146] D. Forster, *Hydrodynamic fluctuations, broken symmetry, and correlation functions*, ser. Frontiers in Physics. Reading, Mass.: WA Benjamin, Inc., 1975, vol. 47.

[147] H. Stehfest, Comm. ACM, vol. 13, pp. 47–49, 1970.

[148] B. J. Berne and G. Harp, Adv. Chem. Phys, vol. 17, p. 63, 1970.

[149] A. M. Nikitin and A. P. Lyubartsev, J. Comp. Chem., vol. 28, pp. 2020–2026, 2007.

[150] H. W. Horn, W. C. Swope, J. W. Pitera, J. D. Madura, T. J. Dick, G. L. Hura, and T. Head-Gordon, J. Chem. Phys., vol. 120, p. 9665, 2004.

[151] P. G. Wolynes, J. Chem. Phys., vol. 68, p. 473, 1978.

[152] P. Zhu, L. Pratt, and K. Papadopoulos, J. Chem. Phys., vol. 137, p. 174501, 2012.

[153] L. X. Dang and H. V. R. Annapureddy, J. Chem. Phys., vol. 139, p. 084506, 2013.

[154] H. V. R. Annapureddy and L. X. Dang, J. Phys. Chem. B, vol. 118, pp. 8917–8927, Jul. 2014.

[155] L. X. Dang and T.-M. Chang, J. Chem. Phys., vol. 106, p. 8149, 1997.

[156] B. Smit, J. Chem. Phys., vol. 96, p. 8639, 1992.

[157] D. McQuarrie, *Statistical Mechanics*. University Science Books, 2000.

[158] C. P. Smyth, *Dielectric behavior and structure; dielectric constant and loss, dipole moment and molecular structure.* McGraw-Hill, 1955.

[159] G. Williams, *Advances in Polymer Science*. Springer, 1979.

[160] G. Williams and D. C. Watts, Trans. Faraday Soc., vol. 66, pp. 80–85, 1970.

[161] O. Borodin, D. Bedrov, and G. Smith, Macromolecules, vol. 35, pp. 2410–2412, 2002.

[162] R. Payne and I. E. Theodorou, J. Phys. Chem., vol. 76, p. 2892, 1972.

[163] M. T. Hosamani, N. H. Ayachit, and D. K. Deshpande, J. Mol. Liq., vol. 145, pp. 55–57, 2009.

[164] L. Zhang and M. L. Greenfield, J. Chem. Phys., vol. 127, p. 194502, 2007.

[165] G. G. Hoffman and L. R. Pratt, Proceedings of Louisiana EPSCoR RII LA-SiGMA Symposium, 2011.

[166] S. K. Ma, *Modern Theory of Critical Phenomena*. Reading, MA: W. A. Benjamin, Inc, 1976.

[167] H. L. Friedman and W. D. T. Dale, "Electrolyte solutions at equilibrium," in *STATISTICAL MECHANICS PART A: EQUILIBRIUM TECHNIQUES*, B. J. Berne, Ed. New York: Plenum, 1977, pp. 85–136.

[168] H. L. Friedman, Ann. Rev. Phys. Chem., vol. 32, pp. 1798–204, 1981.

[169] W. G. McMillan Jr and J. E. Mayer, J. Chem. Phys., vol. 13, pp. 276–305, 1945.

[170] T. L. Hill, *STATISTICAL THERMODYNAMICS*. Reading, MA USA: Addison-Wesley, 1960.

[171] S. A. Adelman, Chem. Phys. Letts., vol. 38, pp. 567–570, 1976.

[172] P. G. Kusalik and G. N. Patey, J. Chem. Phys., vol. 89, pp. 7478–7484, 1988.

[173] C. P. Ursenbach, D. Wei, and G. N. Patey, J. Chem. Phys., vol. 94, pp. 6782–6784, 1991.

[174] D. Sabo, D. Jiao, S. Varma, L. R. Pratt, and S. B. Rempe, Annu. Rep. Prog. Chem. Soc. C, vol. 109, pp. 266–278, 2013.

[175] D. Chandler, J. D. Weeks, and H. C. Andersen, Science, vol. 220, pp. 787–794, 1983.

[176] P. Zhu, L. R. Pratt, and K. D. Papadopoulos, J. Chem. Phys., vol. 137, p. 174501, 2012.

[177] G. Hummer, L. R. Pratt, and A. E. García, J. Phys. Chem, vol. 100, pp. 1206–1215, 1996.

[178] C. H. Bennett, J. Comp. Phys., vol. 22, pp. 245–268, 1976.

[179] J. E. Mayer and M. G. Mayer, *Statistical Mechanics*, 2nd ed. Wiley-Interscience, 1977.

[180] A. Münster, *Statistical Thermodynamics.* Academic Press, New York, 1974, vol. 2.

[181] H. L. Friedman, *Ionic Solution Theory.* Interscience, 1962.

[182] R. L. Graham, D. E. Knuth, and O. Patashnik. Addison-Wesley, 1989.

[183] R. Vogelsang and C. Hoheisel, J. Stat. Phys., vol. 54, p. 315, 1987.

[184] J. Hansen and I. McDonald, *Theory of Simple Liquids.* Academic Press, 1976.

[185] R. Zwanzig, *Nonequilibrium Statistical Mechanics.* Oxford, 2001.

Biography

Xinli You was born on July 30, 1986 in Hangzhou city of Zhejiang province in China. Xinli attended Zhejiang University from September 2004 till June 2008, where she completed her bachelor degree in bio-engineering.

In August 2008, Xinli went to United States to pursue her advanced degree in Chemical Engineering at Tulane University. As a doctoral student, she worked with Prof. Lawrence R. Pratt. Her research focus was on interfacial characteristics of propylene carbonate and validation of simulation models for electrochemical double-layer capacitors. She has published 3 peer reviewed journal articles and one book chapter, and has presented her research several times in international conferences. She received Distinguished Graduate Student Award of 2013 from Chemical and Biomolecular Engineering department at Tulane University, and Tulane IBM Cooperation Fellowship in Computational Science in 2009.